



universität
wien

DISSERTATION

Titel der Dissertation

„Investigations of the static and dynamic mechanical properties of nanostructured Cu and Cu-Al alloys processed by High-Pressure Torsion“

Verfasserin

Mag. Jelena Horky

angestrebter akademischer Grad

Doktorin der Naturwissenschaften (Dr. rer. nat)

Wien, 2015

Studienkennzahl lt. Studienblatt:

A 091 411

Dissertationsgebiet lt. Studienblatt:

Physik

Betreuerin / Betreuer:

ao. Univ.-Prof. Dr. Michael Zehetbauer

Abstract

This thesis deals with different aspects concerning the mechanical behaviour of nanostructured materials processed by High-Pressure Torsion (HPT). Furthermore, different experimental set-ups which have been developed to measure mechanical properties of small-scaled samples are presented.

Tensile tests of HPT Cu and Cu-Al alloys and their analysis using the Taylor equation reveal that the strength of these materials is to be ascribed mainly to the high dislocation density, and not only to the limited grain size. Moreover, the dislocations are in a low-stress arrangement. It is shown that such an arrangement is beneficial for the ductility. A comparison with literature data reveals that the dislocation arrangement, which is mainly determined by the processing parameters, has more influence on the ductility than the stacking fault energy or the twin density of the material.

Further experiments investigate cyclic deformation behaviour in the high cycle fatigue regime as well as crack growth in HPT Cu of different purity and thermal stability. These dynamic mechanical properties are also studied in a high purity HPT Cu with bimodal grain size distribution. Nanostructured HPT Cu generally shows an enhanced fatigue strength compared to its coarse grained counterpart. However, in case of high purity HPT processed material, grain coarsening at high number of loading cycles occurs which markedly deteriorates the fatigue strength. As concerns the fatigue crack growth rate, that of HPT Cu is increased compared to the coarse grained material. Also the threshold stress intensity factor range is lower. At low crack propagation rates, grain coarsening also occurs during crack growth near the crack tip. This phenomenon leads to a retardation of fatigue crack growth and takes place irrespective of the purity of the HPT material. However, a certain level of stored energy being connected to a certain density of deformation-induced defects seems to be a condition for this behaviour.

Kurzfassung

Die vorliegende Dissertation behandelt verschiedene Aspekte des mechanischen Verhaltens nanostrukturierter Materialien, die mittels Hochdruck-Torsion (HPT) hergestellt wurden. Außerdem werden unterschiedliche experimentelle Aufbauten vorgestellt, die zur Messung mechanischer Eigenschaften von Proben mit kleinen Dimensionen entwickelt wurden.

Zugversuche an HPT Cu und Cu-Al-Legierungen und deren Analyse mithilfe der Taylor-Gleichung zeigen, dass die Festigkeit dieser Materialien in erster Linie der hohen Versetzungsdichte zuzuschreiben ist und nicht allein der limitierten Korngröße. Die Versetzungen befinden sich außerdem in einer spannungsarmen Anordnung, welche sich ihrerseits positiv auf die Duktilität auswirkt. Durch Vergleich mit Literaturdaten wird gezeigt, dass die Versetzungsanordnung, die hauptsächlich durch die Prozessparameter bestimmt wird, einen größeren Einfluss auf die Duktilität hat als andere Materialparameter wie die Stapelfehlerenergie oder die Dichte der Zwillingskorngrenzen.

Weitere Experimente untersuchen das Wechselverformungsverhalten sowie das Ermüdungsrisswachstum in HPT Cu unterschiedlicher Reinheit bzw. thermischer Stabilität. Diese dynamischen mechanischen Eigenschaften werden außerdem an hochreinem HPT Cu mit einer bimodalen Korngrößenverteilung studiert. Die nanostrukturierten HPT Materialien zeigen durchwegs eine gegenüber dem unprozessierten grobkörnigen Zustand verbesserte zyklische Dauerfestigkeit. Allerdings wird diese in hochreinem HPT Cu durch eine bei hoher Lastwechselzahl auftretende Kornvergrößerung stark beeinträchtigt. Andererseits ist das Ermüdungsrisswachstum in nanostrukturiertem HPT Cu erhöht, auch der Schwellwert des Spannungsintensitätsfaktors ist kleiner im Vergleich zu grobkörnigem Cu. Im Bereich sehr niedriger Risswachstumsraten kommt es auch hier zu einer Kornvergrößerung im Bereich um die Rissspitze. Diese führt zu einer Verlangsamung des Risswachstums und tritt unabhängig von der Reinheit auf. Allerdings scheint ein bestimmtes Ausmaß an gespeicherter Energie, die mit einer bestimmten Dichte an Verformungsdefekten verbunden ist, Voraussetzung für dieses Verhalten zu sein.

Contents

Introduction	1
1 Theoretical background and literature overview	5
1 Defects in crystalline metallic materials	5
1.1 Vacancies	5
1.2 Dislocations	6
1.3 Stacking faults	7
1.4 Grain boundaries	7
1.4.1 Twin boundaries	8
2 Mechanical properties of metallic materials	11
2.1 Static properties: Tensile tests	11
2.1.1 Elastic and plastic deformation	12
2.1.2 Strength	13
2.1.3 Ductility	14
2.2 Dynamic properties: High cycle fatigue	15
2.2.1 Fatigue strength	16
2.2.2 Stages of fatigue damage	17
2.2.3 Effect of notches	17
2.3 Dynamic properties: Fatigue crack growth	18
2.3.1 Influence of load ratio	19
2.3.2 Retardation of crack growth & crack closure effects	20
3 Nanostructured materials by Severe Plastic Deformation	23
3.1 Production techniques	23
3.1.1 Severe Plastic Deformation	23
3.2 Structure	26
3.2.1 Stages of deformation and grain refinement	26
3.2.2 Defects in SPD materials	28
3.3 Mechanical properties of SPD materials	28
3.3.1 Tensile strength & ductility	28
3.3.2 Cyclic deformation behaviour	31
3.3.3 Fatigue crack growth	34

II	Experimental techniques for small-sized specimens	39
4	Tensile tests	41
4.1	Sample geometry	41
4.2	Experimental set-up and strain measurement	41
4.3	Data evaluation and measurement accuracy	46
5	High cycle fatigue	51
5.1	Ultrasonic resonance fatigue testing	51
5.2	Sample geometry	52
5.3	Calibration and determination of stress amplitude	54
6	Fatigue crack growth	57
6.1	Sample geometry	57
6.2	Experimental set-up	58
6.2.1	Calibration and determination of stress amplitude	58
III	Results & discussions	61
7	Strength and ductility of HPT processed nanostructured Cu and Cu-Al alloys	63
7.1	Introduction and motivation	63
7.2	Investigated materials and measurement methods	68
7.3	Results	69
7.3.1	Microstructure of HPT processed Cu & Cu-Al alloys	69
7.3.2	Strength and ductility	71
7.4	Discussion	74
7.4.1	Strength	74
7.4.2	Ductility	77
7.5	Conclusions	81
8	Fatigue strength and fatigue crack growth rates in HPT processed nanostructured Cu	83
8.1	Introduction	83
8.2	Experimental	83
8.2.1	Materials	83
8.2.2	Tensile Tests	84
8.2.3	Ultrasonic resonance fatigue testing system	85
8.3	Results and discussion	86
8.3.1	Fatigue life time curves	86
8.3.2	Fatigue crack growth threshold	86
8.3.3	Microstructural evolution in high purity HPT Cu	88
8.4	Conclusions	90

9	Effect of microstructural stability on fatigue crack growth behaviour of HPT processed nanostructured Cu	91
9.1	Introduction	91
9.2	Material and methods	92
9.3	Experimental results	92
9.3.1	Microstructural stability	93
9.3.2	Fatigue crack growth at constant stress amplitude	93
9.3.3	Relation of crack growth and strength in HPT Cu	97
9.3.4	Change of stress amplitude	98
9.4	Discussion	99
9.4.1	Influence of grain coarsening on crack propagation	99
9.4.2	Comparison of crack growth with cyclic deformation in the HCF regime	100
9.5	Summary and conclusions	102
10	Summary and conclusions	105
11	Outlook	110
IV	Appendix	111
A	HPT processed Cu after heat treatment	111
B	Microstructure and strength of quenched Cu and Cu-Al alloys	113
C	Short-range order in Cu-Al	115
C.1	Introduction	115
C.2	Short-range order in quenched Cu-Al alloys	115
C.3	Short-range order after HPT processing and order hardening	116
D	Comparison of literature on SPD Cu-Al alloys	119
E	Tensile properties & DSC of Cu-Al-Zn processed by HPT	121
E.1	Short-range order in the Cu-Al-Zn alloy	122
	Bibliography	125
	Curriculum Vitae	137
	Acknowledgements	141

INTRODUCTION

This thesis deals with the mechanical behaviour of nanostructured materials. The investigated properties range from tensile strength and ductility to the mechanical behaviour under cyclic loading with a focus on fatigue crack growth. The investigated materials are copper and copper alloys prepared by High-Pressure Torsion (HPT), a technique which deforms disc shaped specimens by shear under high hydrostatic pressure [1, 2]. The materials processed by this SPD (Severe Plastic Deformation) technique have grain sizes in the sub-micron and nanometer range and a high dislocation density and vacancy concentration [3–5].

The effect of SPD processing on mechanical properties has been quite widely investigated by different research groups studying different metals and alloys (see for example [1, 6–10]). However, while the drastic increase of strength is obvious, the influence of SPD processing on ductility, fatigue strength and resistance against fatigue crack growth is not that well investigated.

It is the aim of this work to shed more light on the relation between the microstructure obtained by SPD and the mechanical properties of these materials. Copper has been chosen because it is a rather simple single phase material which has been the subject of many previous studies.

The precise research questions are derived from the literature overview (chapter 3) and cover ductility and strength of HPT processed Cu-Al alloys as well as crack propagation in HPT Cu of different purity and different microstructural stability as shortly summarised here:

A lower stacking fault energy as well as a lower processing temperature both lead to a higher twin density of SPD processed metals [11–15]. Literature reports that such materials exhibit a better ductility [16–21]. It is the aim of this work to critically inspect this statement and to investigate the influence of grain size, dislocation density and arrangement as well as twin density on strength and ductility of SPD Cu-Al alloys. Own experiments on HPT processed materials will be discussed in comparison with results from literature using different SPD techniques.

Concerning the fatigue strength, it was observed by several authors that the stability of the microstructure of SPD materials is a big topic in case of cyclic loading [22–26]. Strain-induced grain coarsening was found to have a detrimental effect on the fatigue life time

in high purity SPD Cu. It is the aim of this thesis to investigate not only fatigue strength but also fatigue crack growth behaviour of HPT Cu of different purity and to examine the influence of microstructural stability on fatigue crack propagation. Furthermore, a bimodally structured high purity HPT Cu obtained by a proper heat treatment is investigated. This material exhibits higher microstructural stability and higher ductility but lower strength compared to the HPT processed one.

One general issue when investigating and comparing the mechanical properties of SPD processed materials is the usually limited sample size. Especially in case of HPT which produces rather small disc shaped specimens, non-standard sample geometries have to be used. The development of reliable experimental set-ups is therefore an important part of this thesis.

A laser-speckle based sensor for contactless strain measurement was successfully adopted to obtain tensile stress-strain curves of miniaturised dog-bone shaped specimens. A set-up and sample geometry to investigate the fatigue properties in the high cycle fatigue regime was developed within my Diploma thesis and is also used in this work. Fatigue crack growth properties of miniaturised HPT specimens were measured using a newly developed and carefully calibrated specimen holder and geometry.

Outline of the thesis

The thesis consists of three parts. The first part gives a general introduction to defects in crystalline materials as well as to the mechanical properties investigated within this work and the different ways to determine them. Furthermore, there is a chapter giving a detailed literature review on nanostructured materials, their production, structure and especially their mechanical properties. The precise research questions are obtained from this literature overview.

The second part describes in detail the experiments done within this work. As all the mechanical tests were conducted using small-sized specimens and specially adapted test set-ups, particular emphasis is given on this chapter. Details on the sample geometry, the sample preparation, the set-up, as well as on calibration measurements are given separately for tensile tests, fatigue life time tests in the high cycle fatigue regime and crack propagation tests in chapters 4, 5 and 6, respectively. The section on the laser-speckle sensor for direct strain measurement during tensile straining has already been published in the *Proceedings of the 20th IMEKO TC2 Symposium on Photonics in Measurement* in 2011.

The third part is a presentation and discussion of the obtained results. The first chapter therein covers the tensile strength and ductility of HPT processed Cu and Cu-Al alloys. The influence of the microstructure obtained by SPD processing (grain size, dislocation density and arrangement, twin density) on strength and ductility will be discussed.

The next two chapters within this part deal with the fatigue and crack propagation behaviour of nanostructured Cu processed by HPT. These two chapters have already been published in peer-reviewed international journals. The first paper “Role of structural parameters of ultra-fine grained Cu for its fatigue and crack growth behaviour” (p. 83) was published in *Journal of Alloys and Compounds* in 2011 and covers mainly the fatigue strength and the threshold stress intensity factor range of HPT Cu of different purity and grain size. The second paper entitled “Effect of microstructural stability on fatigue crack growth behaviour of nanostructured Cu” (p. 91) was published in *Mechanics of Materials* in 2013. It is a continuation of the research published in the first paper with focus on the influence of strain-induced grain coarsening on crack propagation rates.

This part is completed by a detailed summary of all the results and an outlook containing some remarks for possible future investigations.

Some further results which are mainly connected to the work on Cu-Al alloys (namely details on short-range order in the alloys and a short study of an HPT processed Cu-Al-Zn alloy) can be found in the appendix.

PART I

THEORETICAL BACKGROUND AND LITERATURE OVERVIEW

1 Defects in crystalline metallic materials

This section gives an introduction to the different types of defects existing in a crystalline metallic material. To keep this section short, it will only deal with defects in single phase materials. For further information on the various effects of different solute atoms, phase boundaries and precipitates, the reader is referred to standard textbooks (e.g. [27–32]).

1.1 Vacancies

A vacancy is simply a point defect where a lattice site is vacant. A certain vacancy concentration exists even in thermodynamic equilibrium at finite temperatures, so it is not possible to get a vacancy-free crystal. For example, the equilibrium vacancy concentration (vacant lattice sites per overall lattice sites) at the melting point is 2×10^{-4} for copper [27, p. 61]. At room temperature this equilibrium value is much lower (in the range of 10^{-21}) but one has to take into account that the mobility of the vacancies is also markedly decreased at low temperatures. Hence, a high vacancy concentration at room temperature can be produced by rapidly quenching a material from a temperature close to the melting point.

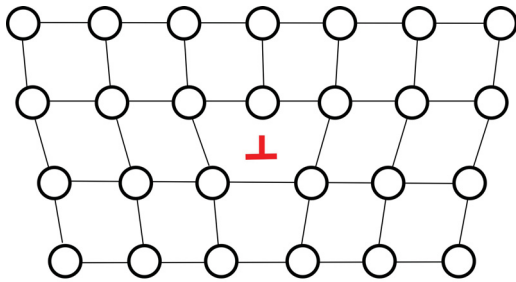
During plastic deformation of a metal, vacancies can be absorbed or emitted by the climb of edge dislocations or they can be created by other mechanisms involving the movement and interaction of dislocations [33]. Typical vacancy concentrations after conventional deformation are in the order of $10^{-5} - 10^{-6}$ [33].

Moreover, vacancies are mainly responsible for diffusion processes [29, p. 155f].

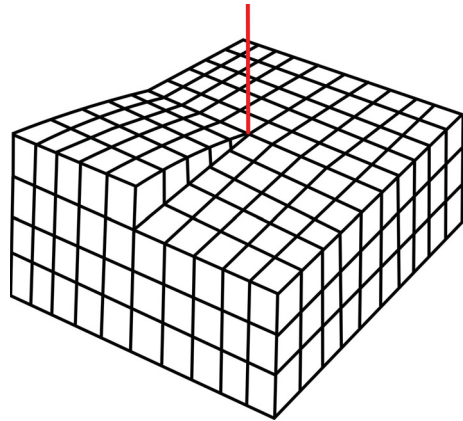
1.2 Dislocations

Dislocations are line defects within the crystalline lattice. In case of an *edge dislocation*, one lattice plane ends within the crystal as depicted in fig. 1.1a. The second possibility of a dislocation can be seen in fig. 1.1b and is called *screw dislocation*.

Almost every “real” dislocation is a mixture between those two principle types but a mixed dislocation line can always be separated within a screw and an edge part.



(a) Two-dimensional sketch of an edge dislocation. The dislocation line is perpendicular to the image plane at the position of the red mark.



(b) Crystalline lattice around a screw dislocation. The dislocation line is marked in red.

Figure 1.1: Dislocations (after [27, p. 65f]).

Dislocations are characterised by their dislocation line vector and their Burgers vector, the second being the length and direction the two parts of the crystal are shifted against each other when the dislocation is moving [27, p. 66].

When a stress is applied to a crystalline material, the glide of dislocations causes plastic deformation. The glide plane is the cross product of the dislocation line vector and the Burgers vector [27, p. 69]. In case of a screw dislocation these two vectors are parallel, so a screw dislocation has no well-defined glide plane and can therefore change its glide plane easily. This is called *cross slip*. Edge dislocations and mixed dislocations on the other hand can only change their glide plane through *climb*. This requires vacancies. Edge dislocations can therefore annihilate and also create vacancies.

A typical value for the dislocation density of an annealed metal is 10^{12} m^{-2} [34, p. 235]. This means that within one cubic millimeter there are dislocations that have a total length of one kilometer. Dislocations can be created and multiplied during plastic deformation, for example by the Frank-Read-mechanism [29, p. 241]. When two antiparallel dislocations meet, they can also annihilate.

If the movement of a dislocation is hindered by some obstacle (this can be other dislocations, boundaries or particles), a higher stress is required to overcome this obstacle. Introducing barriers for dislocation glide therefore increases the strength of a material.

1.3 Stacking faults

A stacking fault is a defect in the stacking sequence of the close-packed lattice planes. It can either be grown in during solidification or created during plastic deformation by the movement of a partial dislocation [29, p. 40].

The specific energy of a stacking fault – the *stacking fault energy* (SFE) – is an important material parameter determining the dissociation length of partial dislocations and thereby also the slip and twinning behaviour of a material, see p. 8.

1.4 Grain boundaries

A grain boundary is the interface between two areas (= grains or crystallites) exhibiting the same lattice structure but different orientations [27, p. 73]. The lattices of the two grains can thereby be twisted or tilted against each other – leading to the differentiation between twist and tilt boundaries. However, most grain boundaries have both features.

A common classification distinguishes between *low-angle grain boundaries* (LAGBs) and *high-angle grain boundaries* (HAGBs). The first ones have misorientation angles below $10\text{--}15^\circ$ and can be built up by parallel edge dislocations in case of a tilt boundary or by an array of screw dislocations in case of a twist boundary [29, p. 41]. HAGBs exhibit a larger misorientation angle and have a highly distorted structure which can in general not be described easily.

Grain boundaries are usually rather straight, as can be seen in fig. 1.2. The point where the boundaries of three neighbouring grains meet each other is called triple junction.

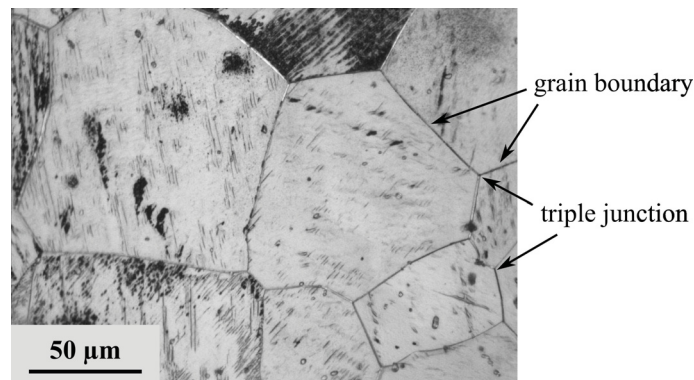


Figure 1.2: Light microscopy image of the grain structure in a magnesium alloy revealed by etching.

Grain boundaries block the movement of dislocations, thereby increasing the strength of the material. This is described in detail in section 2.1.1.

1.4.1 Twin boundaries

Mechanical twinning is a deformation mechanism where a part of the crystal (or the grain) is transformed by shear into an orientation with mirror symmetry relative to the matrix [27, p. 207]. The boundary in between is called twin boundary and is highly coherent, see fig. 1.3. There are different twinning systems (i.e. twinning planes and shear directions) for different lattice types; in cubic lattices there are 12 twinning systems. Furthermore, the specific energy of a twin boundary depends on the material.

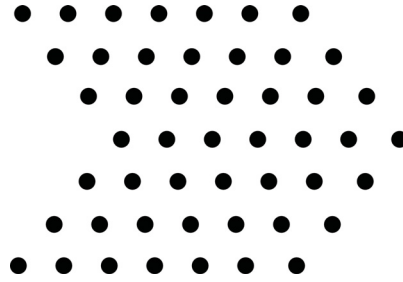


Figure 1.3: 2D-sketch of a twin boundary.

The critical stress for twinning is generally larger than for dislocation glide. Mechanical twinning therefore mainly occurs at high degrees of deformation or at deformation at low temperatures – in both cases the critical stress for (further) dislocation movement is enhanced.

Other possibilities for twins are annealing twins which can form during recrystallisation or grain growth and twin boundaries grown in during solidification [27, p. 212]. They are not associated with shear of the crystal.

Stacking fault energy and twinning

A lower stacking fault energy (SFE) is known to promote twinning. The reason for this relation is the following: A full dislocation can decrease its energy through a dissociation into two partial dislocations. Each of these partials has half of the Burgers vector (b) of the full dislocation and due to the fact that the energy of a dislocation is $\frac{1}{2}Gb^2$ per unit length (with G being the shear modulus) [27, p. 221], the two partials have a lower total energy than the full dislocation. A stacking fault forms between the two partial dislocations which has a certain energy and prevents a complete separation of the partials as depicted in fig. 1.4.

Due to the fact that the partials of a full screw dislocation are no screw dislocations any more, cross slip of a dissociated screw dislocation is only possible if the two partials recombine. In a material with lower SFE and therefore a larger distance between the partials, larger stresses are necessary to recombine the partials and allow cross slip [27, p. 240ff]. This has a high hardening effect and can lead to deformation by mechanical twinning instead of dislocation glide [27, p. 297].

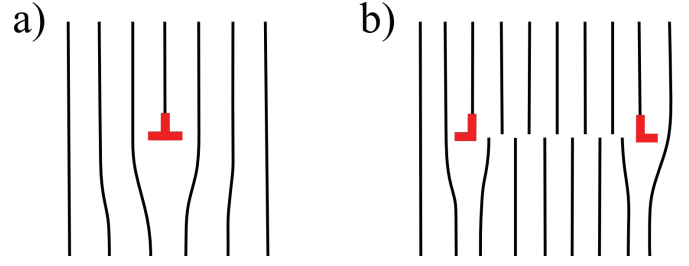


Figure 1.4: Dissociation of a full dislocation (a) into two partials (b) generating a stacking fault in between (after [27, p. 241]).

Another way to promote deformation by mechanical twinning is lowering the deformation temperature or increasing the strain rate. With both, the dislocation motion will be restricted and the critical resolved shear stress (CRSS) for dislocation slip will be increased by a larger amount than the CRSS for twinning [17, 35]. The difference between the CRSS values for the two deformation modes will therefore get smaller with decreasing deformation temperature and twinning will occur more frequently. The influences of strain rate and deformation temperature can be described by a single parameter, the Zener-Hollomon parameter Z [36]:

$$\ln Z = \ln \dot{\epsilon} + \frac{Q}{RT} \quad (1.1)$$

where $\dot{\epsilon}$ is the strain rate, Q the activation energy for diffusion, R the gas constant and T the temperature.

2 Mechanical properties of metallic materials

2.1 Static properties: Tensile tests

The most common experiment to determine mechanical properties of materials is a quasi-static (which means low strain rate) tensile test. Other static mechanical tests would be compression tests, bending tests or torsion tests – but as they are not part of this work they will not be described further.

In a tensile test, a specimen with the shape of a bar or rod is continuously strained until failure. The typical result of such a test can be seen in fig. 2.1.

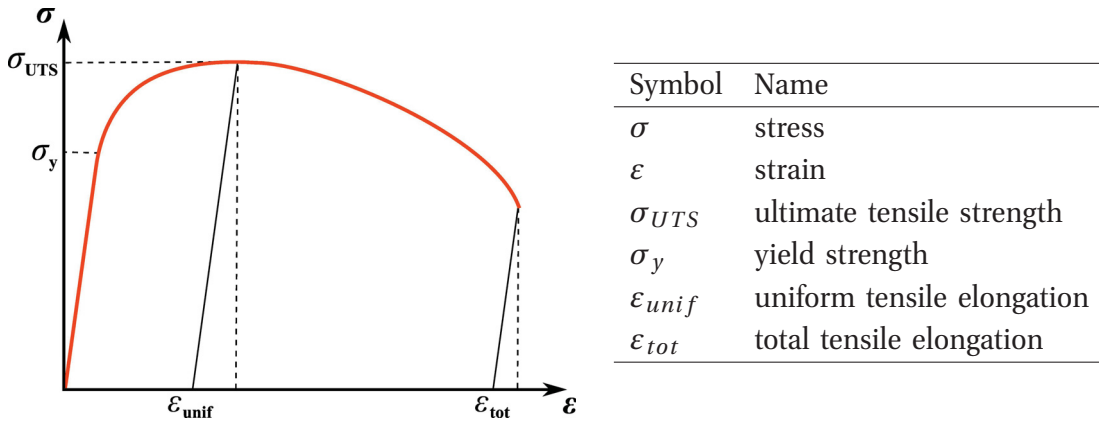


Figure 2.1: Sketch of a typical engineering stress-strain curve of a ductile metallic material.

Definition of stress and strain – “Engineering vs. True”

During a tensile test a certain force (F) is applied leading to an engineering stress $\sigma_{eng} = \frac{F}{A_0}$, where A_0 is the initial cross-section area of the sample. As the cross-section changes during testing – the sample gets longer and thinner – the true stress can be defined as $\sigma_{true} = \frac{F}{A}$, where in this case A is the actual cross-section area of the sample.

As long as the deformation is uniform and no localised deformation (= necking) occurs, the actual cross-section can be calculated using the conservation of volume: $A_0 \times l_0 = A \times l = const.$, where l_0 is the initial length and l the actual length of the specimen. This leads to a correlation between the engineering and the true stress:

$$\sigma_{true} = \sigma_{eng}(1 + \varepsilon_{eng}) \quad (2.1)$$

Similar definitions can be made in case of the strain. The engineering strain refers to the initial length of the specimen (eq. 2.2) while the true strain is the derivative of the

length related to the actual length (eq. 2.3).

$$\varepsilon_{eng} = \frac{l - l_0}{l_0} = \frac{\Delta l}{l_0} \quad (2.2)$$

$$d\varepsilon_{true} = \frac{dl}{l} \quad (2.3)$$

An integration of the latter formula leads to the following:

$$\varepsilon_{true} = \int_{l_0}^l \frac{dl}{l} = \ln \frac{l}{l_0} = \ln \frac{l_0 + \Delta l}{l_0} \quad (2.4)$$

$$\varepsilon_{true} = \ln(1 + \varepsilon_{eng}) \quad (2.5)$$

The equations 2.1 & 2.5 are often used to calculate the more physical true stress-strain curve from the engineering one. But while eq. 2.5 is always valid, eq. 2.1 implies a uniform deformation and is therefore only valid until the ultimate tensile strength. To determine the true stress when necking occurs, the smallest cross-section area must be measured *in-situ* during the experiment.

2.1.1 Elastic and plastic deformation

If an external force is applied to a material, it will deform. If the applied stress stays below the yield strength of the investigated material, the deformation will be elastic, which means that the original shape of the specimen will be regained immediately when the stress is released. In case of a tensile or compressive force the relation between the applied stress σ and the resulting strain ε is given by Hook's law, where E is the *Young's modulus* or elastic modulus:

$$\sigma = E\varepsilon \quad (2.6)$$

The value of the Young's modulus is determined by the material or alloy composition and in case of single crystals or heavily textured material also by the angle between the applied force and the crystal orientation.

Strictly speaking, elastic deformation only takes place at strain values below 10^{-4} [27, p. 190] but the first non-linear behaviour is only microscopically and technically insignificant. However, if the applied stress exceeds the yield strength of the material, the sample starts to flow and deforms plastically.

In contrast to elastic deformation, plastic deformation of a solid leads to an irreversible change of the specimen's shape. The main mechanism thereby is the movement of dislocations, see section 1.2. During plastic deformation the dislocations accumulate and the material hardens. In a tensile test this strain or work hardening compensates the decrease in cross-sectional area and the stress continues to rise [37, p. 3]. When the ultimate tensile strength is reached, the hardening capability of the material is no more able to prevent any localisation of deformation. Necking occurs and the applied load for further deformation decreases. But taking into account the actual (local) cross-section, the true stress-strain curve will not fall off but continue to rise after necking.

2.1.2 Strength

To characterise the tensile strength of a material two specific values are used: the *yield strength* (σ_y) and the *ultimate tensile strength* (σ_{UTS} or just UTS). The first one characterises the end of the elastic regime while the second tells the maximum stress a material can bear before the deformation localises, i.e. necking starts.

Using the engineering stress-strain curve, the ultimate tensile strength is just the maximum of the curve. The yield strength is not so easily to determine and for practical reasons the so-called *offset yield strength* $\sigma_{0.2}$ is used. Therefore a straight line parallel to the elastic one starting from a strain value of 0.2% is drawn. The intercept of this line with the stress-strain curve is the technical definition of the yield strength.

Generally, the strength of a crystalline material is increased by introducing obstacles to dislocation motion [38, p. 163]. These obstacles can be other dislocations (= work or strain hardening), boundaries (grain, cell or phase boundaries), solid-solution atoms or particles. The hardening effect is in general higher if the distance between the obstacles is smaller.

The yield strength as a function of the dislocation density was first theoretically described by Taylor [39]. The obtained equation is named after him:

$$\sigma_y = \sigma_0 + \alpha M G b \sqrt{\rho} \quad (2.7)$$

where σ_0 is the friction stress, α a parameter representing the arrangement of dislocations, M the Taylor factor ($M = 3.06$ for non-textured polycrystalline fcc materials [27, p. 250]), G the shear modulus, b the Burgers vector and ρ the dislocation density.

Grain boundary strengthening is expressed by the *Hall-Petch* relation [40, 41]:

$$\sigma_y = \sigma_0 + k_0 d^{-1/2} \quad (2.8)$$

where d is the grain diameter and σ_0 and k_0 are constants depending on the specific material. This equation can be explained by the pile-up model (see for example [38, p. 170]): when a polycrystalline material is loaded, yielding will first occur in grains with slip systems favourably oriented with respect to the tensile axis. Within these grains dislocations will move but their movement will be hindered by a grain boundary leading to a dislocation pile-up in front of the boundary. The resulting pile-up stress can cause dislocation emission and movement within the neighbouring grain (which has a less favourable orientation). The magnitude of the stress concentration arising from the pile-up depends on the number of dislocations therein and is therefore larger in larger grains where bigger pile-ups can evolve. Thus, the *external* stress which has to be applied to cause yielding in the second grain is lower if the grain size is larger due to the larger additional stress arising from the dislocation pile-up in the first grain.

Thinking of all the possible strengthening mechanisms (and the even much larger number of metallurgical ways to make use of them) gives rise to the conclusion that the strength of a material is a complex issue. Additionally, the results achieved through tensile tests depend on testing parameters like strain rate, temperature and environment [38, p. 16].

2.1.3 Ductility

According to [37, p. 1], “ductility” is a slippery term: it “implies the opposite of brittleness, the inverse of strength and conjures images of extensibility and ease of fabrication”. It is basically the ability of a material to deform plastically without fracturing.

In case of a tensile test, two parameters are used to characterise the ductility: the *uniform elongation / uniform strain* (ϵ_{unif}) and the *total elongation / total strain* (ϵ_{tot}). These values can be derived from the engineering stress-strain curve by going back along a straight line according to the Young’s modulus from the UTS and the fracture point, respectively, see fig. 2.1. Sometimes also the elastic part is included in the uniform as well as in the total elongation (e.g. in [37, p. 3]), these are then the values corresponding to the vertical dashed lines in fig. 2.1. The difference can be quite significant if the material has a low Young’s modulus, a high yield stress or a small work hardening capability.

A different measure of ductility would be the cross-section reduction at fracture. It describes the damage resistance of a material better than the total elongation – but anyhow, its quantitative use is difficult because of the triaxial stress state in the necking region [37, p. 9].

It is difficult to generalise the effects of different microstructural variables on ductility. Although the ductility usually decreases when the strength increases, there are many exceptions to this rule [37, p. 20]. But in general, a large uniform elongation is promoted by a high rate of strain hardening [37, p. 6]. Or in other words, initially soft materials, which have a high ability to accumulate dislocations, generally show larger elongation in tensile tests.

For the total elongation of a specimen also the fracture behaviour is important. A good ductility can be achieved in materials which are able to distribute strain and have structures that prevent the nucleation of localised slip surfaces [37, p. 57]. This is also connected to the sensitivity of a material to surface defects or notches. The tendency to concentrate or distribute strain, furthermore, is related to dislocation behaviour, shear band formation, stacking fault energy and strain hardening behaviour [37, p. 50].

Just as the strength, also the ductility of a material is not a unique property but varies with the mode of testing (or the stress state), the strain rate, the temperature and the environment. For example, metals generally become more ductile if the temperature is increased above room temperature. In the so-called static strain rate range, an increase in

strain rate causes an increase of the uniform tensile elongation for fcc and hcp materials. For bcc materials the effect is contrary [37, p. 27].

A special case of highly ductile behaviour is superplastic deformation. Thereby, up to 8000% elongation in tension can be achieved [42]. This is possible during high temperature and low strain rate deformation of fine grained alloys and involves mechanisms like grain boundary sliding and grain rotation [38, p. 295ff].

Influence of specimen geometry

To get valid results from tensile tests, the sample has to be strained without any bending stresses but also the shape of the specimen has an influence. Precisely, the post-necking elongation – i.e. the difference between total elongation and uniform elongation – and the shape of the engineering stress-strain curve in this range directly depend on the ratio between sample diameter and length [43, p. 325][37, p. 7]. The reason is that in a ductile metallic material the size of the part of the gauge length where necking occurs depends on the cross-section area. As in this stage of the tensile test the deformation is limited to the necking area, also Δl depends on this area and is independent of the overall gauge length (l_0). If now the initial sample length l_0 is different, the strain is also different. Testing short and thick samples leads to larger values of the total elongation than testing long and thin samples.

For miniaturised dog-bone shaped specimens of nanostructured copper this has been shown by Zhao et al. [44] and by Kulyasova et al. [45]. They showed systematically that larger thickness at constant length as well as shorter gauge length at constant thickness cause higher values of the total elongation. In [44] the values of the total elongation varied strongly between 10% and 70%, depending on the sample dimensions.

To overcome the problem of different specimen geometries, the DIN EN 10002-1 standard gives the following correlation between gauge length l_0 and cross-section area A_0 to get comparable tensile test results [46, p. 100]:

$$l_0 = 5.65\sqrt{A_0} \quad (2.9)$$

2.2 Dynamic properties: High cycle fatigue

The term *fatigue* means that cyclic loading of a material leads to the initiation of cracks and finally to the fracture of a test specimen or an engineering structure. The number of cycles causing fracture can thereby vary from some few to several millions and billions. Tests in the regime below 10^4 cycles are usually conducted under constant plastic strain amplitudes and are called *low cycle fatigue* (LCF) tests. Tests beyond this number of cycles are called *high cycle fatigue* (HCF) tests and are usually stress-controlled [47, p. 138ff]. Moreover, the regime beyond 10^8 cycles is often called ultra-high or very high cycle fatigue regime.

There are different ways to represent fatigue life time data. One is the Coffin-Manson plot which shows the applied plastic strain amplitude against the number of loading cycles to failure. In the HCF regime usually a Wöhler or S-N plot is used. It shows the applied stress amplitude against the number of loading cycles to failure. A sketch of a typical S-N curve of a metallic material can be seen in fig. 2.2. The stress varies periodically between the lower value σ_{min} and the upper value σ_{max} as shown in the inset in fig. 2.2. The load range is $\Delta\sigma = \sigma_{max} - \sigma_{min}$ and the stress amplitude is half of this value.

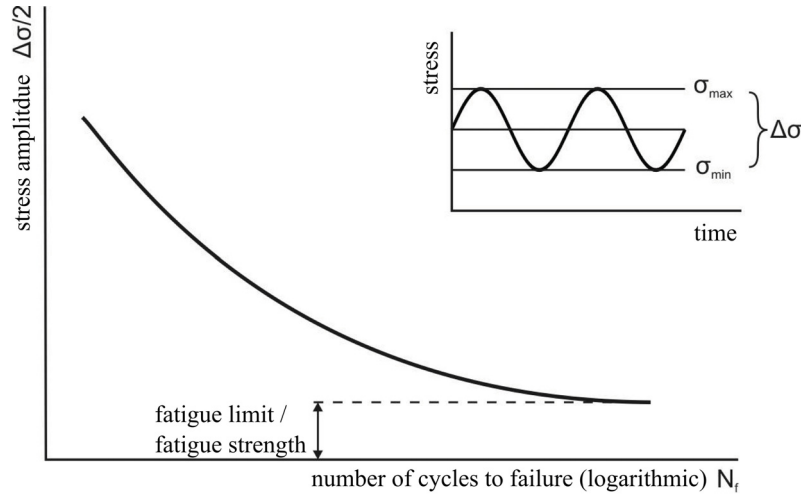


Figure 2.2: Sketch of a typical fatigue life time curve (after [47, p. 10]).

However, not only the cyclic stress amplitude, but also the mean stress is important. The mean stress is characterised by the load ratio R :

$$R = \frac{\sigma_{min}}{\sigma_{max}} \quad (2.10)$$

High cycle fatigue tests are often conducted under zero mean stress, implying that half of the loading cycle is compressive. The load ratio is then $R = -1$. A larger value of the load ratio typically shifts the S-N curve down to lower stress amplitude values [38, p. 573].

External parameters like testing temperature or environment of course also influence the fatigue behaviour of a material [48, p. 362ff]. Furthermore, fatigue testing can also be done under variable amplitude loading or under multiaxial loading [48, p. 314ff].

2.2.1 Fatigue strength

It is also indicated in fig. 2.2 that below a certain stress amplitude the material does not break at all (or at least not at a number of cycles which is experimentally accessible). This stress amplitude is called fatigue limit, endurance limit or *fatigue strength*. It is between

35% to 50% of the ultimate tensile strength for most steels and copper alloys [48, p. 128]. This also implies that materials exhibiting a high tensile strength usually show a high fatigue strength.

There are also materials which do not show a clear fatigue limit, e.g. many high strength steels and aluminium alloys [48, p. 128]. Interior fracture at non-metallic inclusions can play an important role in the ultra-high cycle fatigue regime [49].

2.2.2 Stages of fatigue damage

Fatigue loading of a specimen leads in the first stage to microstructural changes of the material. They can sum up and initiate a crack which grows during further cycling and leads to the fracture of the specimen. When testing in the high cycle fatigue regime, the first stage – i.e. the number of cycles before any microcracks can be detected – usually requires most of the overall life time of the specimen.

The mentioned microstructural changes are associated with the to and fro movement of dislocations and can lead to cyclic hardening or softening of the material. The former is typical for initially annealed and soft materials exhibiting an initially low dislocation density while the latter is typical for materials which previously have been mechanically processed and hardened [47, p. 17]. Cyclic hardening and softening can be measured by monitoring the hysteresis loop during cycling at constant stress or strain amplitude [47, p. 14].

The dislocation movement during fatigue loading creates typical structures. This can be planar arrays of dislocations in case of materials exhibiting a low stacking fault energy and cell structures or persistent slip bands in case of high stacking fault energy materials [47, p. 62].

Traces of the dislocation movement can be observed on the sample surface in form of extrusions and intrusions [48, p. 62]. This evolving surface roughness can be seen as the origin of microcracks. It is therefore – and also due to the fact that fatigue cracks mainly originate from the surface – obvious that the fatigue life time can depend on the surface state of the investigated samples [50, p. 25].

2.2.3 Effect of notches

At a notch or any general geometric discontinuity the stress is generally higher than the nominal value [50, p. 381]. The ratio of the stress at a notch (σ_{max}) to the nominal stress (σ_{nom}) can be calculated from elasticity theory. This *theoretical stress concentration factor* is defined as [47, p. 184]:

$$K_t = \frac{\sigma_{max}}{\sigma_{nom}} \quad (2.11)$$

It depends on the geometry of the notch and the mode of testing (tension, bending, torsion). A variety of calculated stress concentration factors can be found for example in the handbook of Peterson [51].

The effect of a notch on the fatigue strength, however, can be different and can also depend on the material [52, p. 92]. The experimentally determined stress concentration factor is usually smaller than the theoretical one but approaches the latter in case of large notch radii and high strength materials [48, p. 272]. The ratio between experimentally obtained and theoretically calculated effect of a notch is called *notch sensitivity*.

2.3 Dynamic properties: Fatigue crack growth

If a metallic material – a test specimen or a structural part in an application – contains a crack, this crack will grow with (further) cyclic deformation if the length of the crack and the applied load amplitude are large enough. Crack propagation rates are usually described in terms of the *stress intensity factor range* ΔK , which is a concept of linear elastic fracture mechanics. The definition of ΔK is the following [48, p. 192]:

$$\Delta K = K_{max} - K_{min} \quad (2.12)$$

$$\Delta K = f(a) \Delta \sigma \sqrt{\pi a} \quad (2.13)$$

where $\Delta \sigma$ is the applied stress range ($\sigma_{max} - \sigma_{min}$), a the crack length and $f(a)$ is a geometrical factor which depends on the ratio of the crack length to the width of the specimen. If σ_{min} is negative, ΔK is considered to be equal to K_{max} [53], assuming that the crack is closed and does not grow when the stress is compressive.

A typical curve, which is obtained when analysing the fatigue crack growth behaviour, shows the crack propagation rate (crack advance per number of loading cycles, da/dN) as a function of ΔK in a double logarithmic way and can be seen in fig. 2.3.

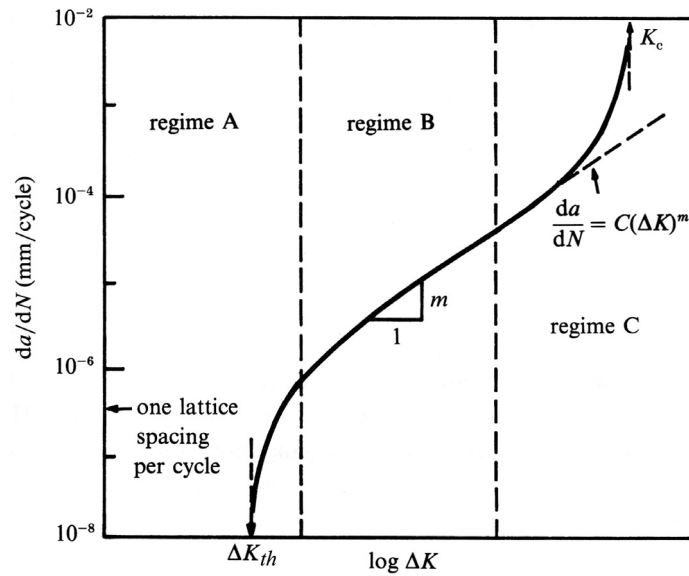


Figure 2.3: Typical fatigue crack growth curve of a metallic material [48, p. 203].

Three stages of crack growth can be distinguished: regime A, the so-called near-threshold regime, regime B, also called Paris-regime, and the high growth rate regime C.

Below a certain value of ΔK , the crack does not grow at all. This value is called the *threshold stress intensity factor range* ΔK_{th} . The existence of such a threshold value implies that at a certain applied stress range there are cracks which are too small to grow. Or in other words, for each crack length there exists a critical stress amplitude which is necessary for the growth of the crack.

Regime A is characterised by a non-continuous failure process where the crack advance per loading cycle is in the order of one lattice spacing or even considerably lower. Failure mode is the so-called *Stage I*, meaning single shear in the direction of the primary slip system leading to a crystallographic and tortuous crack path as depicted in fig. 2.4. Crack growth in the near-threshold regime strongly depends on microstructure, load ratio, environment and crack closure effects [48, p. 204]. The cyclic plastic zone, i.e. the zone around the crack tip which is plastically deformed, is typically smaller than the grain size (or the characteristic microstructural dimension).

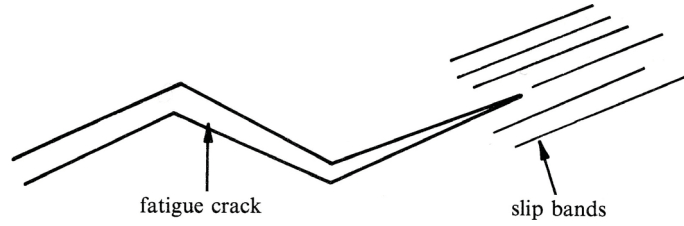


Figure 2.4: *Stage I* crack growth [48, p. 195].

Crack growth in regime B can be described by the Paris law:

$$da/dN = C (\Delta K)^m \quad (2.14)$$

where C and m are constants characterising the material. m is typically between 2 and 4 for ductile alloys [48, p. 193]. Crack growth occurs in this regime via *Stage II* failure mode, which is a duplex shear mechanism (see fig. 2.5), where the plastic zone at the crack tip encompasses many grains. The formation of striations on the fracture surfaces and a crack path normal to the loading axis are typical features of Stage II.

In regime C, K_{max} reaches the fracture toughness of the material. Here again large microstructural and load ratio effects can be observed [48, p. 204].

2.3.1 Influence of load ratio

The *load ratio* (R) is a further important parameter in addition to the stress intensity factor range:

$$R = \frac{K_{min}}{K_{max}} = \frac{\sigma_{min}}{\sigma_{max}} \quad (2.15)$$

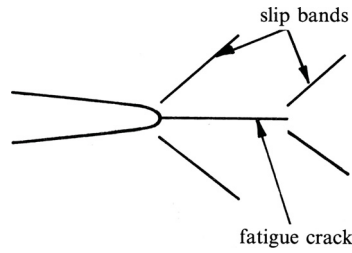


Figure 2.5: Stage II crack growth [48, p. 196].

Fig. 2.6 shows three different types of loading curves with the same $\Delta\sigma$ (and therefore in case of equal crack lengths also the same stress intensity factor range) but different load ratios. It is obvious that mainly due to the different values of σ_{max} resulting in the same ΔK , the stress intensity factor range alone is not enough to fully characterise the testing conditions. Fatigue crack propagation experiments are usually conducted under positive load ratio.

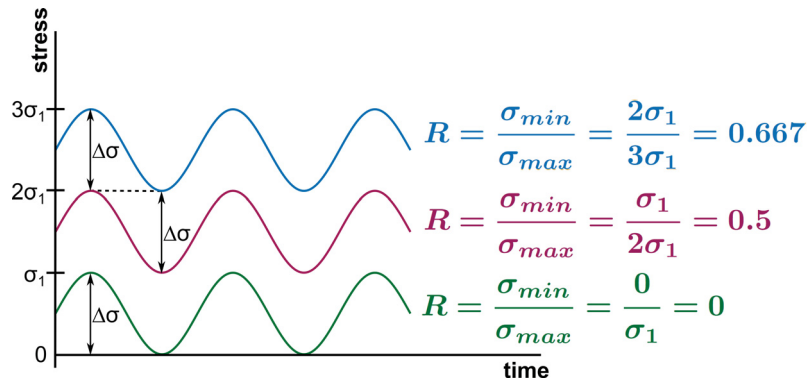


Figure 2.6: Sketch of fatigue loading curves having the same stress range ($\Delta\sigma$) but different load ratios (R).

The effect of the load ratio on the measured crack growth curves is especially high in regime A and C, see fig. 2.7. A higher R -value leads to a smaller threshold stress intensity factor range and a faster propagation rate in the near-threshold regime due to smaller crack closure effects [48, p. 245]. Crack growth in the high growth rate regime is also increased because a higher value of R means that K_{max} reaches the fracture toughness of the material at lower values of ΔK .

2.3.2 Retardation of crack growth & crack closure effects

It is obvious that a fatigue crack can only propagate during the fraction of the loading cycle in which the crack faces are completely separated [48, p. 228]. The phenomenon that a fatigue crack can be closed even under tensile load is called *crack closure*. A variety of mechanisms can cause such a behaviour, a detailed description can be found for example in the book of Suresh [48, p. 222ff]. The most prominent closure effects

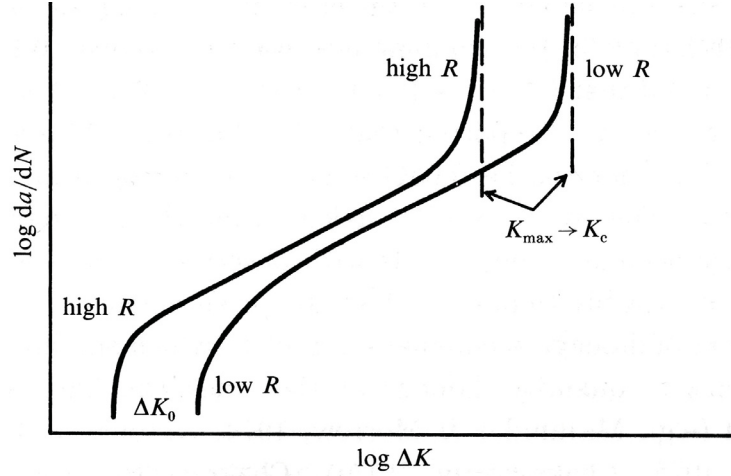


Figure 2.7: The effect of load ratio (R) on fatigue crack growth curves [48, p. 220].

are *plasticity-induced crack closure*, where the zone of residual strain, which is left in the wake of the fatigue crack, causes premature contact between the faces of the crack, *oxide-induced crack closure*, and *roughness-induced crack closure*. The latter means that deflections of the crack path, which particularly form during crystallographic *Stage I* crack growth, lead to a certain roughness of the crack path. The smallest mismatch between the fracture surface asperities can now lead to premature contact of the crack sides.

All these crack closure effects cause a retardation of the fatigue crack growth. They are generally more prominent at low ΔK and at small load ratios [48, p. 252].

By determining the stress intensity factor above which the crack is fully open (K_{op}), e.g. by measuring the crack opening displacement [48, p. 225ff], it is possible to calculate the effective stress intensity factor range [48, p. 228]:

$$\Delta K_{eff} = K_{max} - K_{op} \quad (2.16)$$

The effective threshold stress intensity factor range $\Delta K_{th, eff}$ determined this way shows no dependence on the load ratio [54, p. 37], confirming that the R -dependence of the threshold value is due to crack closure effects.

3 Nanostructured materials by Severe Plastic Deformation

In this work the terminus “*nanostructured materials*” is used for materials – more precisely metals – exhibiting grain sizes in the range of some tens to some hundreds of nanometer. Several authors distinguish between *ultra-fine grained* materials having grain sizes between 100 nm and 1 μm and “truly” *nanocrystalline* materials possessing grain sizes below 100 nm [55]. As there is usually no reason for an explicit distinction (no discrete change of properties at this point), the terminus “nanostructured” will be used in a more general way within this chapter.

3.1 Production techniques

There are several methods for the production of bulk nanostructured materials. They can be separated into the two big groups of *top-down* and *bottom-up* techniques [10]. Top-down techniques start with a bulk, coarse grained piece of metal and introduce defects and grain boundaries until the material becomes nanostructured. This can be done either by *Ball Milling* [56] (which usually results in powder samples which have to be compacted afterwards) or by the various techniques of *Severe Plastic Deformation* (SPD) which will be described below.

Bottom-up techniques are for example *Electrochemical Deposition* [57] or *Inert Gas Condensation* [58]. Thereby, you build up the nanostructured material from small parts like individual atoms or clusters of atoms. These methods can provide either powder or bulk samples – anyway, not in too large amounts.

As bottom-up techniques as well as Ball Milling are not part of this work, they will not be described further. Also for the special features of nanostructured materials produced by these methods, e.g. problems with contamination and consolidation in case of powder samples, the reader is referred to literature (e.g. [58–60]).

3.1.1 Severe Plastic Deformation

Since the early 1990s several methods of processing nanostructured materials by plastic deformation have been established [61]. They all have in common that the workpiece is deformed to very high strains – which is also reflected in the name “Severe Plastic Deformation” (SPD). Such a large deformation can only be done when preventing free flow and fracture of the material by using a proper sample and tool geometry and thereby producing a significant hydrostatic pressure [62]. This also implies that the shape of the sample stays more or less the same during processing. The most prominent SPD methods are *Equal-Channel Angular Pressing* (ECAP) and *High-Pressure Torsion* (HPT) [6]. The second one is used in this work, while results on materials processed by the first method will

be used for comparison. Both methods will therefore be explained in more detail in this section. Further SPD methods would be for example *Accumulative Roll-Bonding* (ARB) or *Rolling and Folding* (R&F) [63], *Hydrostatic Extrusion* (HE) [64] and *Multi-Directional Forging* [61]. Several further methods to produce nanostructured materials and combination of different SPD techniques are recently discussed, see for example [65].

Equal-Channel Angular Pressing is the most prominent SPD technique – probably because it was the first one capable to produce large-scale samples. This technique repeatedly presses a billet through a die containing two channels with a certain angle in between, see fig. 3.1. At the intersection of the two channels, the sample is deformed by shear.

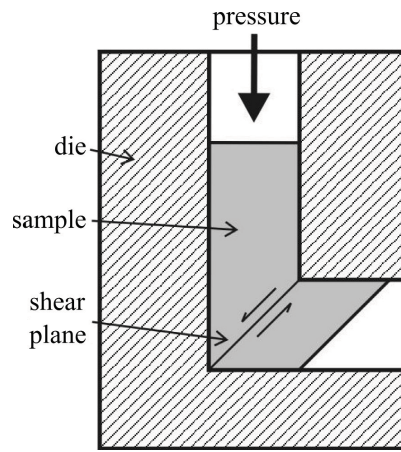


Figure 3.1: The principle of Equal-Channel Angular Pressing.

The strain during each ECAP pass is described by the following equation [66]:

$$\epsilon = \frac{1}{\sqrt{3}} \left[2 \cot \left(\frac{\Theta}{2} + \frac{\Psi}{2} \right) + \Psi \operatorname{cosec} \left(\frac{\Theta}{2} + \frac{\Psi}{2} \right) \right] \quad (3.1)$$

where Θ is the angle between the channels and Ψ specifies the curvature at the intersection of the channels. The strain during each pass is approximately 1, consecutive ECAP passes increase the total strain. The sample can be rotated between the passes, leading to different routes of deformation (the most prominent are called A, B_C and C) which can strongly influence the grain refinement process [67].

In case of hard-to-deform or brittle materials, a larger intersection angle is used, or the whole die and the sample are heated up to elevated temperatures.

There are also ECAP tools available where a back pressure can be applied to the sample. Back pressure can lead to a more uniform deformation and a better workability of the sample material [68].

High-Pressure Torsion deforms a disc-shaped specimen by shear under high hydrostatic pressure [1, chap. 9]. The sample is placed between two anvils with cavities fitting to the diameter of the sample. The desired pressure (typically 1 – 8 GPa) is applied and then one anvil is rotated against the other, see fig. 3.2. The sample and the anvils have a certain surface roughness (usually obtained by sand blasting) which – together with the high pressure – prevents sliding of the sample.

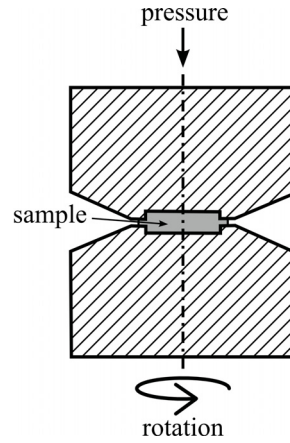


Figure 3.2: Sketch of the principle of HPT processing.

The degree of deformation depends on the applied number of rotations (N), the sample height (h) and varies over the radius (r) of the sample. It can either be expressed in terms of torsional strain (γ_t) or equivalent von Mises strain (ϵ) [1, p. 219]:

$$\gamma_t = \frac{2\pi Nr}{h} \quad (3.2)$$

$$\epsilon = \frac{1}{\sqrt{3}} \frac{2\pi Nr}{h} \quad (3.3)$$

As the shape of the sample does not change during deformation, the strain which is applied to the sample can be freely chosen and high strain values can be obtained easier than through ECAP. Also rotation speed and deformation temperature can be varied, the later by inductive heating of the anvils or by cooling the anvils and the sample in a bath of liquid nitrogen or solid carbon dioxide snow.

HPT is also capable to deform brittle materials like intermetallics [69] or ceramics [70].

3.2 Structure

The main feature of nanostructured materials is a grain size in the sub-micron or nanometer range. Especially when they are produced by SPD techniques, also other types of defects which are induced by the large plastic strain have to be taken into account – i.e. dislocations and vacancies.

Moreover, each SPD technique produces a specific texture, e.g. shear texture in case of HPT or ECAP and typical rolling texture in case of ARB. The grains are sometimes also elongated along a certain direction of the sample.

3.2.1 Stages of deformation and grain refinement

In the deformation curve of an fcc (face-centered cubic) single crystal different stages can be distinguished [27, p. 232]. Stage I, “easy-glide”, means that only one slip system is activated and occurs only if the crystal is aligned for single slip. Stage II is characterised by a linear hardening with relatively high work hardening rate due to the activation of a secondary slip system and the interaction between the dislocations acting on the two slip systems. In stage III the work hardening rate decreases due to the cross slip of screw dislocations and the resulting dynamic recovery [71].

During stages II and III the dislocations change from a homogeneous arrangement to a cell structure [72, 73], in case of wavy glide materials thick dislocation cell walls containing dislocation dipoles form [74]. With further deformation and the transition to stage IV the cell walls become thinner, separating increasingly misoriented dislocation free regions [74] thereby building sub-grain or low-angle grain boundaries (LAGBs). The global dislocation density increases steadily [75]. The subsequent stage V can be characterised by the onset of the annihilation of edge dislocations through climb [76].

Due to the large strains applied during SPD processing, sub-grain boundaries and LAGBs formed during the early stages of deformation transform into high-angle grain boundaries (HAGBs) resulting in a reduction of the grain size. Furthermore, recovery and recrystallisation processes play a role, especially when deforming pure metals or when the deformation is done at rather high homologous temperature. Recovery means the rearrangement and annihilation of dislocations, while recrystallisation describes the formation of new grains within highly deformed and defect-rich areas [77, p. 1ff].

It should be noted that the grain refinement process described here may not be valid for all lattice structures. Papers report that in case of hexagonal magnesium the grain refinement occurs not by the formation of sub-grain boundaries but by the formation of nanosized recrystallized grains at the grain boundaries of the original structure [78, 79].

Evolution of grain size with strain

The grain size of a sample decreases with increasing SPD strain, an example is given

in fig. 3.3. Furthermore, the fraction of HAGBs and the average misorientation angle between neighbouring grains increase [5].

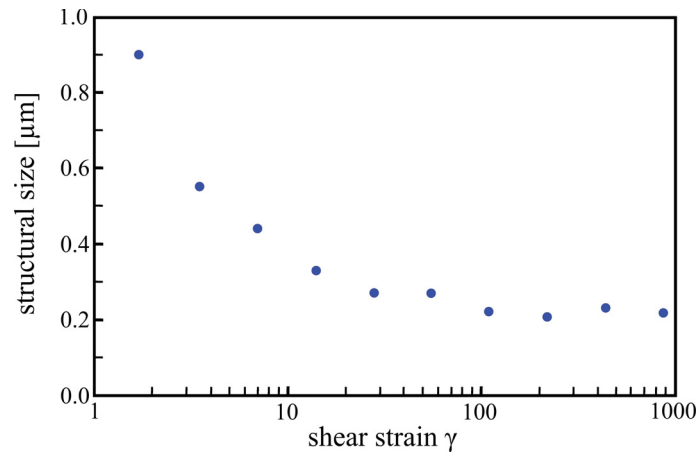


Figure 3.3: Grain size (as determined from back scattered electron micrographs) as a function of applied shear strain for 99.99% pure Cu processed by HPT at room temperature using a pressure of 2 GPa. Data from [80].

For a complete characterisation not only the average grain size, but also the grain size distribution and the grain shape have to be taken into account. Fig. 3.4 shows the structure of ECAP processed aluminium after only one ECAP pass. It can be seen that there is still a large number of LAGBs and that the grains are elongated along the shear plane. The structure becomes generally more homogeneous with increasing deformation.

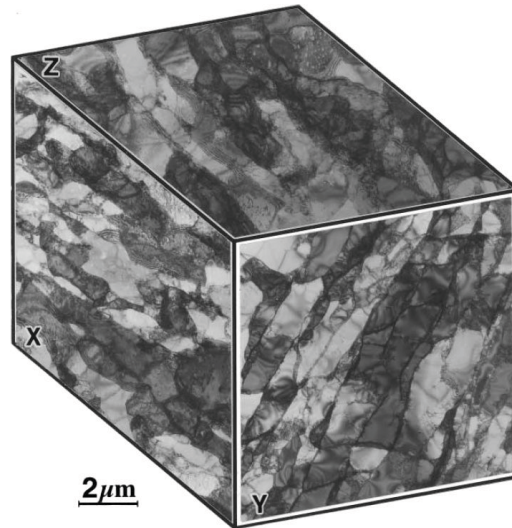


Figure 3.4: Microstructure of pure Al after 1 ECAP pass at room temperature. The extrusion direction is perpendicular to the x-plane. From [81].

It can also be seen from fig. 3.3 that after a certain applied strain the grain refinement saturates, meaning that with further increase of strain the grain size remains unchanged.

This limit of grain refinement or saturation grain size strongly depends on the material, the processing temperature and also the strain path [1, p. 231]. Alloying or impurities as well as deforming at lower temperatures lead to smaller grain sizes in the saturation regime [5].

3.2.2 Defects in SPD materials

With increasing SPD strain not only the number of grain boundaries increases, but also the dislocation density and the number of vacancies increase. Due to the large plastic deformation and increased hydrostatic pressure during deformation, the number of dislocations and vacancies after SPD is higher than after conventional deformation. The increased hydrostatic pressure restricts diffusion as well as the mobility of the lattice defects leading to a lower level of defect annihilation during deformation [62].

The dislocation density of HPT processed materials increases not only with strain but also with hydrostatic pressure during deformation [3]. It has been shown recently [82] that during the release of the hydrostatic pressure after deformation, dislocations partially annihilate and rearrange to a low-stress arrangement. This process is accompanied by a decrease of hardness [83].

For the dislocation density and the vacancy concentration there is – just like for the grain size – a saturation at a certain amount of strain. In case of the dislocation density the saturation value is in the range of $10^{15} - 10^{16} \text{ m}^{-2}$ and in case of the vacancy concentration it is in the range of 10^{-4} , depending on the material and process parameters [4, 84, 85]. It has to be pointed out that this high level of vacancy concentration is close to the equilibrium concentration at the melting temperature.

3.3 Mechanical properties of SPD materials

This section gives an overview of the mechanical properties of SPD processed nanostructured materials. The focus is on properties investigated within this work, i.e. strength, ductility, fatigue strength and fatigue crack propagation behaviour.

3.3.1 Tensile strength & ductility

Due to the very small grain size and also the remarkably high dislocation density, SPD processed nanomaterials show extraordinary high **strength** and hardness. Just to mention a few of the various examples given in literature: ECAP processing increases the yield strength of pure Cu from initially 230 MPa to about 400 MPa in the saturation regime [86]. The ultimate tensile strength of grade 2 Ti is increased from 420 MPa to 670 MPa after 6 ECAP passes [87]. The microhardness of pure Ni after HPT processing up to a strain of $\epsilon=58$ is 3.7 GPa compared to only 0.7 GPa in the annealed state [88].

Increasing the degree of SPD deformation and thereby decreasing the grain size and increasing the defect concentration leads to an increase in strength and hardness, an example can be seen in fig. 3.5 for HPT processed Cu. When grain refinement and defect accumulation saturate, also the level of strength or hardness saturates.

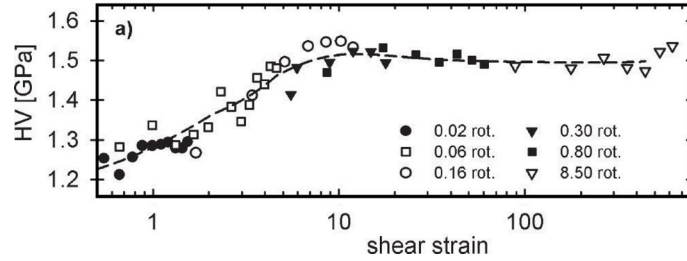
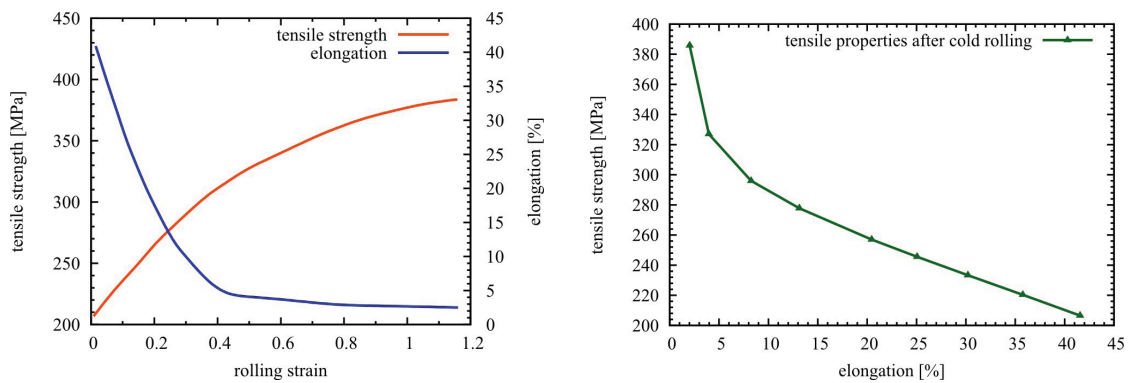


Figure 3.5: Microhardness of HPT processed Cu as a function of shear strain. HPT pressure 8 GPa, number of rotations and measurement radius varied. From [89].

At first, the increase of strength through SPD follows the Hall-Petch relationship (see eq. 2.8) and is therefore not unexpected. However, there are reports that below a certain grain size in the range of 10 nm, the Hall-Petch relationship breaks down, and that there is a yield strength plateaus below a critical grain size or even an inverse Hall-Petch behaviour [10]. Beside the grain boundary strengthening also the increased dislocation density plays a big role in the strength of SPD processed materials. This can be described by the Taylor equation which is given in eq. 2.7.

In contrast to their influence on strength, a small grain size and a large number of defects obtained by plastic deformation are detrimental for the **ductility** of a material. Fig. 3.6 shows an example for conventionally cold rolled Cu. The increasing rolling strain increases the tensile strength but drastically decreases the ductility.



(a) Evolution of tensile strength and ductility with rolling strain.

(b) Correlation between tensile strength and ductility.

Figure 3.6: Strength and ductility of cold rolled Cu (purity 99.94%, initial grain size 40 μm , Data from [90, p. 11]).

Strength and ductility are usually contrary quantities and maintaining the ductility in high-strength materials is a big issue in materials science. The ductility of SPD processed nanostructured materials is generally rather poor. But anyway, they usually have a uniform elongation of some few percent and are not entirely brittle. Many efforts have been made to regain some ductility, see for examples [91–94].

There are two famous papers reporting high strength and simultaneously high ductility in pure materials just after SPD processing [95, 96]. However, such results are very rare and not well reproduced.

When inspecting and comparing the various literature about ductility of nanostructured materials one should be aware of the following points: Nanostructured materials are often tested with non-standard and small-scale sample geometries due to the limited amount of material. As shown in section 2.1.3, the total elongation in a tensile test depends on the specimen geometry. Thus, one should rather compare the values of the uniform elongation of different materials tested with different sample geometries, not the values of the total elongation. Furthermore, strain measurement of small-scaled samples is crucial and has to be done with utmost care. Moreover, some publications show true stress-strain curves where the true stress is obviously calculated by eq. 2.5 even in the necking region where this equation is not valid any more. In some cases this can lead to values of the uniform elongation which seem to be higher than they really are.

The reason for the low ductility of nanostructured materials is the lack of strain hardening and thus the localisation of plastic flow and the formation of a neck [94]. One approach to increase the ductility of nanostructured materials is therefore to produce a bi- or multimodal grain size distribution where the strength is still high due to the small grains while the ductility is large due to the work hardening ability of the larger grains [92]. A bimodal grain size distribution can for example be gained by a proper heat treatment after SPD processing [97].

Another interesting approach is the incorporation of a large amount of twin boundaries into the material [92]. Examples of a large ductility in materials with high twin density can be found for example in [98, 99] for nano-scaled growth twins. The use of highly coherent low-energy twin boundaries instead of high angle grain boundaries and the initially low dislocation density of the material are supposed to allow dislocation storage during tensile straining and restrict dynamic recovery [92].

Meanwhile, also the interactions between twin boundaries and dislocations are believed to make twins effective in simultaneously increasing strength and ductility of nanostructured materials [100]. The interaction depends on the type of dislocation and theoretically possible reactions range from transmission across the twin boundary to glide on the twin plane or detwinning [100], all of them are supposed to have a positive effect on the ductility. As all these interactions have an activation energy, twin boundaries are at first barriers to dislocation slip, consequently increasing the strength of the material.

In case of SPD processed materials, several researcher tried to increase the twin density by lowering the deformation temperature and using alloys with low stacking fault energy, e.g. Cu-Zn [20] or Cu-Al [15, 18, 19].

To investigate the effect of twin boundaries on strength and ductility of SPD materials, Cu-Al alloys processed by HPT at room temperature as well as at liquid nitrogen temperature (77K) are investigated within this thesis. The low stacking fault energy of the alloys as well as the low deformation temperature are believed to increase the twin density in the HPT processed materials.

Other approaches to improve the ductility of nanostructured materials comprise the introduction of very small second-phase particles [101], deformation at low temperatures [102], or materials exhibiting transformation-induced and twinning-induced plasticity [92].

3.3.2 Cyclic deformation behaviour

It was already mentioned in section 2.2.1 that the fatigue limit of a material at first depends on its tensile strength. This is in general also true for SPD processed materials, as can be seen in fig. 3.7. Thus, nanostructured materials typically possess a higher fatigue strength than their coarse grained counterparts.

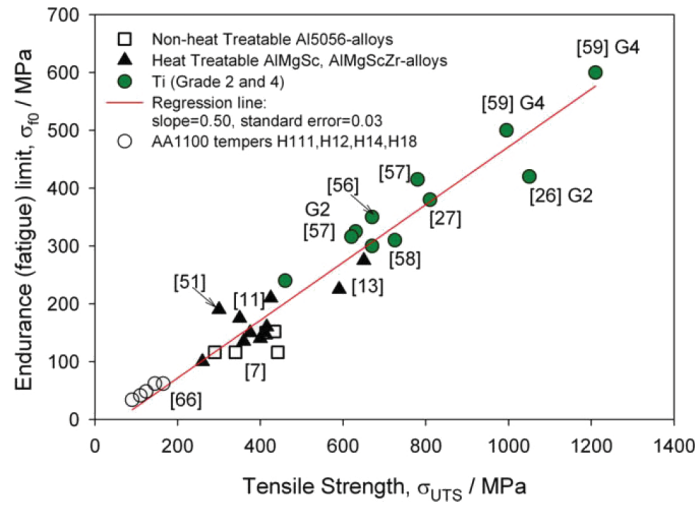
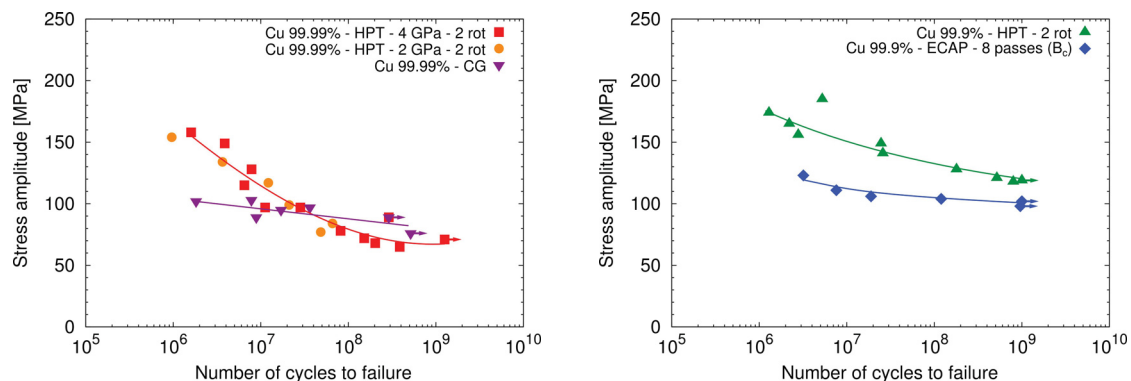


Figure 3.7: Correlation between tensile strength and fatigue limit for Ti and Al alloys processed by different SPD and ageing treatments. From [103].

For a deeper understanding, different influences have to be taken into account as specified by Mughrabi and Höppel [25]: the purity of the investigated material, the mode of fatigue testing and the SPD processing parameters. In the same paper they summarise the results gained by various groups on ECAP processed Cu, which is the most investigated material in this field. They are: generally larger fatigue lives than

coarse grained samples in S-N plots, cyclic softening in strain-controlled tests but not in stress-controlled ones, macroscopic shear bands on the surface serving as crack initiation sites and a cyclically unstable microstructure [25].

The cyclic deformation behaviour of HPT processed Cu was – as far as I know for the first time – investigated in my diploma thesis [22]. The S-N curves obtained in this work ranging from the high cycle to the ultra-high cycle regime can be seen in fig. 3.8. The load ratio was $R = -1$ and the samples were notched stripes with a width of 0.6 mm.



(a) S-N curves of coarse grained (CG) and HPT processed high purity Cu.

(b) S-N curves of HPT and ECAP processed commercial purity Cu.

Figure 3.8: Cyclic deformation behaviour of HPT and ECAP processed Cu. Applied cyclic stress amplitude against number of loading cycle to failure. From [22].

It can be seen from these S-N curves that below 10⁷ loading cycles the fatigue life curve of HPT processed high purity Cu is shifted to higher stress amplitudes compared to coarse grained Cu. This is due to the small grain size and also the higher tensile strength of the nanostructured material. The rather steep decrease of the S-N curve is due to the instability of the microstructure. Fig. 3.9 shows the microstructure of the cycled HPT specimens. Grain coarsening can be detected, which is more pronounced at higher number of loading cycles. The results also show a strong influence of purity. Commercial purity HPT Cu has improved fatigue performance not only due to the smaller grain size and the higher strength compared to high purity HPT Cu, but also due to an enhanced microstructural stability. Grain coarsening in this material was only observed at the highest number of cycles and only next to a crack.

Fatigue properties in the HCF regime of ECAP Cu of different purities were also investigated by Lukáš et al. [104, 105] with the same results like for the HPT samples concerning the effect of purity on the S-N curves. However, they found no grain coarsening even in the high purity samples. It has been claimed that this is due to stress-controlled instead of strain-controlled cycling [25]. Experiments with the latter technique showed grain coarsening in high purity ECAP [25, 106] as well as HPT Cu [22].

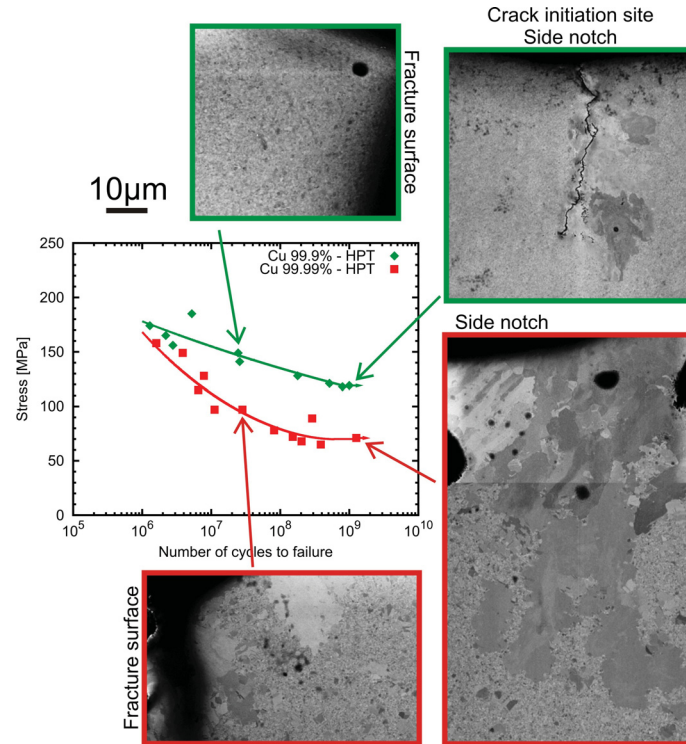


Figure 3.9: Microstructure of cyclically loaded HPT processed Cu (Data and pictures from [22]).

Fig. 3.8b also shows that HPT processed Cu has better fatigue performance than ECAP processed Cu. This is not unexpected as HPT leads to smaller grain sizes (in this case 250 nm compared to 300 nm) and thus to a higher tensile strength (here 500 MPa compared to 400 MPa) than ECAP.

The top right picture in fig. 3.9 raises the question how grain coarsening during fatigue loading influences the crack propagation behaviour of nanostructured materials. Therefore, it was an aim of this thesis to determine fatigue crack propagation rates in HPT processed Cu of different purities and therefore different microstructural stabilities.

The cyclic deformation behaviour in the *low cycle fatigue (LCF) regime* is controlled by the ductility of a material [25]. As nanostructured materials usually exhibit a rather poor ductility, also decreased fatigue life times in the LCF regime compared to CG materials are expected. This has been shown for example for ECAP Cu [107].

The influence of both, increased strength and decreased ductility, can be schematically expressed in terms of the total cyclic strain amplitude leading to a picture of the overall fatigue performance of nanostructured and CG materials as shown in fig. 3.10.

One attempt to increase the overall fatigue performance (LCF and HCF) of nanostructured materials is to regain ductility by introducing a bimodal grain size distribution

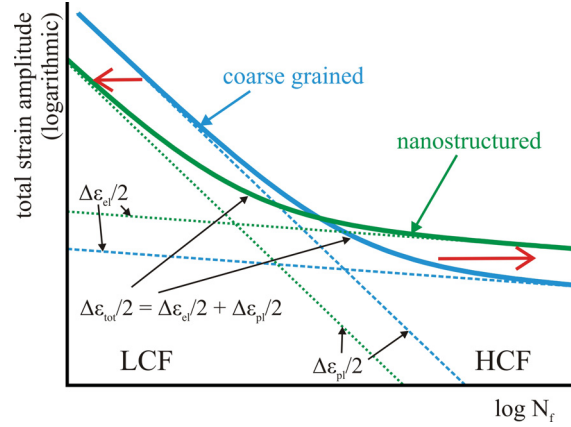


Figure 3.10: Total strain fatigue life diagram comparing coarse grained and nanostructured materials (after [108]).

through a proper heat treatment. It was shown for ECAP Cu that such a heat treatment increases the fatigue life times during plastic strain-controlled cycling [106, 109], but decreases the life times under stress-controlled cycling [110].

It is therefore one of the questions in this thesis how a bimodally structured HPT Cu behaves when it is cyclically loaded in the high and especially in the ultra-high cycle fatigue regime and how the stability of this material during loading influences the fatigue strength.

3.3.3 Fatigue crack growth

One of the first studies of fatigue crack growth in nanostructured materials was published by Vinogradov et al. in 1999 [111]. They investigated an Al-Mg alloy and found out that ECAP processing on the one hand increases the tensile and fatigue strength but on the other hand leads to faster crack propagation in the microstructural sensitive low ΔK -regime and decreases the threshold stress intensity factor range (ΔK_{th}). In the ECAP processed material (grain size 0.5 μm) the crack propagates very straight with only small deflections while the initial material (grain size 25 μm) shows a zig-zaged crack path. The periodicity of the deflections is in the range of the grain size. The authors concluded that roughness-induced crack closure and crack deflections decrease the driving force for crack advance and therefore retard crack growth in materials with larger grains.

Higher crack growth rates and lower threshold values have meanwhile been reported for several nanostructured materials, e.g. cryomilled Al-Mg [112], electro-deposited Ni [113], ECAP Cu (see fig. 3.11) [114], ECAP Al alloys [115, 116] and ECAP steels [117, 118]. All the mentioned experiments have been conducted under load ratios between 0.1 and 0.5 and in the majority of cases compact tensions specimens have been used.

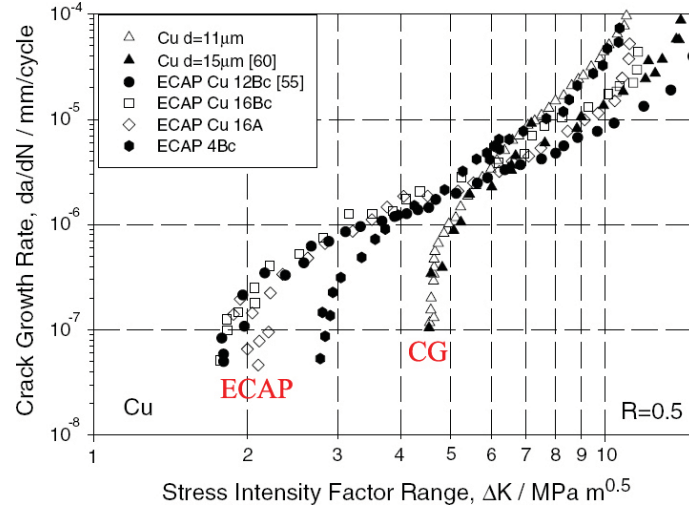


Figure 3.11: Fatigue crack growth in coarse grained and ECAP processed Cu. The threshold stress intensity factor range depends on the number of ECAP passes as well as the used deformation route. From [114].

These results are not unexpected since smaller grain sizes generally lead to lower threshold values [48, 112, 119, 120]. The transition from the microstructure-sensitive near-threshold regime to the microstructure-insensitive Paris-regime particularly depends on the grain size [48, p. 207]. The transition typically occurs when the size of the cyclic plastic zone becomes comparable to the characteristic microstructural dimension of the material [48, p. 208]. If no phases or precipitates are present in the material, the grain size is this characteristic microstructural dimension. The cyclic plastic zone size is proportional to $(\Delta K / \sigma_y)^2$, which leads to the following relation between the value of the stress intensity factor range, where this transition takes place (ΔK_T), and the grain size (d):

$$\Delta K_T \propto \sigma_y \sqrt{d} \quad (3.4)$$

However, this equation is based on linear elastic fracture mechanics and in case of nanostructured materials the theoretically calculated plastic zone size is considerably larger than the grain size – even in the threshold regime. As grain boundaries significantly influence the plastic behaviour of a material, it can be expected that the above-mentioned formula has to be adopted for nanostructured materials.

In addition to the low threshold stress intensity factor ranges, also straight crack paths are a common feature of nanostructured materials, an example can be seen in fig. 3.12 for titanium.

It is therefore supposed that the lower threshold stress intensity factor range in nanostructured materials is due to a less tortuous crack path leading to a smaller roughness-induced crack closure effect. The amount of closure is dependent on the load ratio R : higher R -values cause less closure effects. It has been shown by Hanlon et al. [113] that

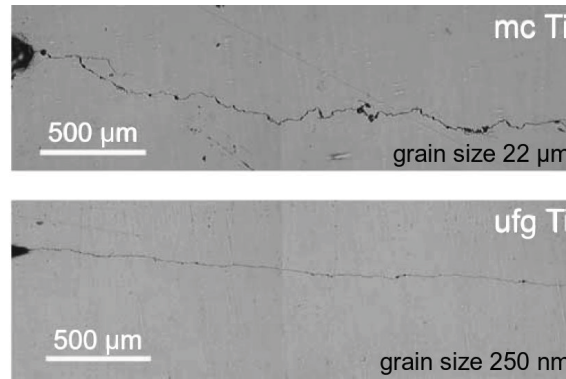


Figure 3.12: Crack paths in coarse grained (mc) and nanostructured (ufg) titanium (ECAP, 8 passes, tested at $R = 0.3$). From [113].

the load ratio effect in nanostructured Ni is in fact reduced. This is confirmation that the absence of roughness-induced crack closure is responsible for faster crack propagation in nanostructured materials.

The reduced threshold stress intensity factor range is disadvantageous for an application of nanostructured materials because the maximum size for non-propagating cracks is reduced. Again, efforts have been made to overcome this problem.

For an ECAP Al alloy an improvement of the fatigue crack growth behaviour was achieved by Meyer et al. [121]. They conducted a proper aging heat treatment which restored the ductility of the material and increased the threshold stress intensity factor range, see fig. 3.13. In this case the improved strain hardening capability had a beneficial effect on the fatigue crack growth rates. However, in this alloy also the nature and size of precipitates influences the crack propagation rate [115].

Generally – and especially when comparing different materials – one has to keep in mind that not only grain size (and grain size distribution) but also factors like precipitate content, size and distribution, stacking fault energy and crystallographic texture are known to have considerable effects on the fatigue and crack growth characteristics of metallic materials [8, 48].

Another finding concerning the fatigue crack growth behaviour of nanostructured materials was done by Hohenwarter et al. [122] investigating HPT processed and afterwards heat treated Ni and Armco-iron with different grain sizes. They observed intercrystalline crack paths in materials with grain sizes smaller than $1\text{ }\mu\text{m}$ whereas materials with larger grain sizes showed transcrystalline crack paths, see. fig. 3.14.

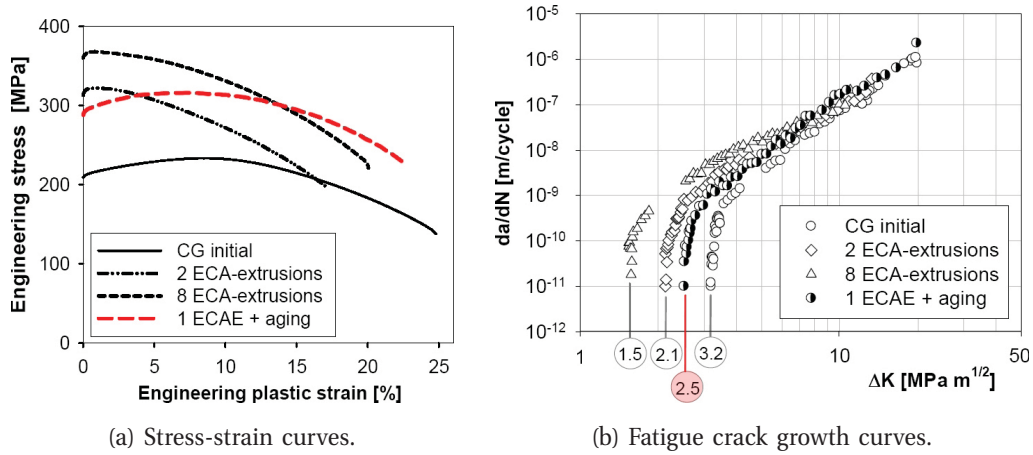


Figure 3.13: Tensile and crack propagation behaviour of the Al alloy AA6060 deformed by ECAP with different numbers of passes and also with an additional aging heat treatment for 18 min at 170°C. From [121].

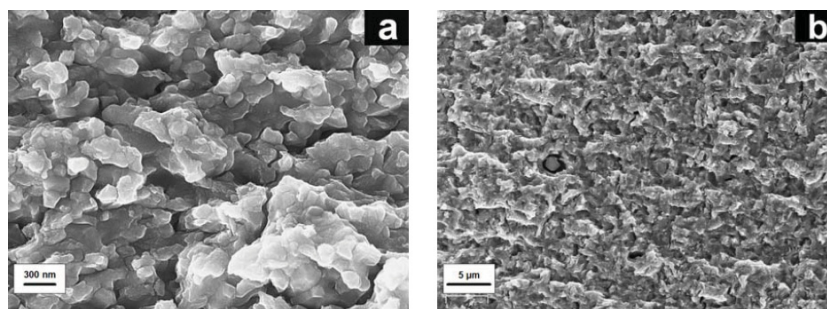


Figure 3.14: Fatigue fracture surfaces of HPT processed Fe. a) Grain size 300 nm: intercrystalline crack path; b) grain size 1 μm : transcrystalline crack path. From [122].

PART II

EXPERIMENTAL TECHNIQUES

FOR SMALL-SIZED SPECIMENS

This part of the thesis describes the experimental set-ups used to determine the mechanical properties of HPT processed nanostructured materials. Since no standard geometries can be used for these samples due to their limited size, special attention is given to calibration measurements and evaluation of the obtained data.

Different types of sample geometries and testing conditions have been used to determine different mechanical properties. They will be specified within the following three chapters. The first one deals with tensile tests and the static mechanical properties obtained thereby, i.e. strength and ductility. Special attention is given to the strain measurement during tensile testing of small-scaled samples. A section within this chapter has already been published in the *Proceedings of the 20th IMEKO TC2 Symposium on Photonics in Measurement* in 2011.

The second chapter describes the cyclic deformation tests performed to determine fatigue life time curves in the high cycle fatigue regime and the fatigue strength of the samples. The set-up was obtained in an earlier work [22].

The set-up used for the crack growth measurements is specified in the third chapter. As these measurements use the same principle of ultrasonic resonance fatigue testing like the fatigue strength measurements, this chapter is shorter and describes only the sample geometry and calibration measurements.

4 Tensile tests

4.1 Sample geometry

Miniaturised dogbone-shaped samples used for tensile tests were cut out of HPT discs by spark erosion. The copper electrode used to obtain the proper geometry was manufactured by the company C. & H. Wöls GmbH, Kottingbrunn. Before cutting, both sides of the HPT discs were polished to get the desired sample thickness in the range of 0.3 mm to 0.6 mm. Special care was taken to get the top and bottom surface parallel within $\pm 5 \mu\text{m}$. Spark erosion was done as gentle as possible to get the surface roughness at the lateral sides as small as possible because it was not possible to polish the lateral sides after cutting. The shape and dimensions of the tensile specimens can be seen in fig. 4.1. The radius at the top and the bottom of the gauge length was 0.5 mm, which means that the samples had parallel gauge lengths of 2.5 mm. The dimensions of the samples are very close to the standard given in eq. 2.9.

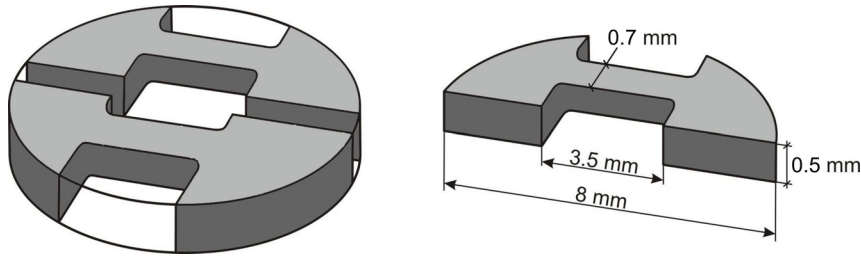


Figure 4.1: Dimensions of the small-scaled tensile test samples (right) and position of the samples on the HPT disc (left).

4.2 Experimental set-up and strain measurement

Published in: Proceedings of the 20th IMEKO TC2 Symposium on Photonics in Measurement (2011) under the title “Application of a locally operating laser-speckle strain sensor on tensile deformation of miniaturized nanostructured specimens”

Authors: J. Horky, M. Lederer, B. Weiss, M. Zehetbauer and B. Zagar

The small specimen size requires special effort on the strain measurement. Thus, we have chosen a laser-speckle strain sensor providing the possibility to measure strains with high local resolution. The sensor is based on the theoretical work of Yamaguchi [123] where the objective laser speckle shift caused by a displacement of the specimen is evaluated in general form. In our geometrical set-up depicted in fig. 4.2 the laser beam is pointing along the z-axis perpendicular to the specimen surface, and the line-scan cameras are in the same x-z-plane perpendicular to the incident light.

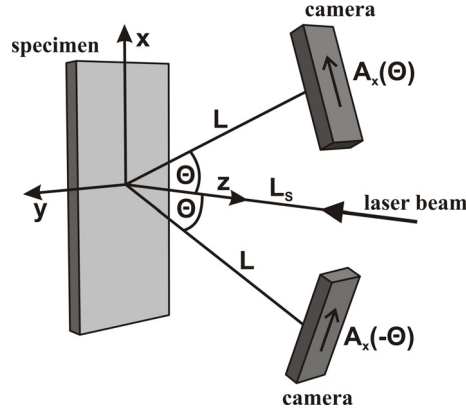


Figure 4.2: Sketch of the measurement set-up with laser beam and two line-scan cameras.

The speckle displacement A_x on the camera plane is then given by [124]:

$$A_x(\Theta) = a_x \left(\frac{L \cos^2 \Theta_S}{L_S \cos \Theta} + \cos \Theta \right) - a_z \left(\frac{L \sin \Theta_S \cos \Theta_S}{L_S \cos \Theta} + \sin \Theta \right) - L \left[\epsilon_{xx} \left(\frac{\sin \Theta_S}{\cos \Theta} + \tan \Theta \right) - \Omega_y \left(\frac{\cos \Theta_S}{\cos \Theta} + 1 \right) \right] \quad (4.1)$$

Here, Θ is the observation angle, L is the distance between specimen surface and observation plane (camera) and L_S is the distance between specimen surface and laser source. The angle Θ_S is the angle between the incident laser beam and the surface normal (z-axis) being approximately zero and therefore not indicated in the sketch (fig. 4.2). It can be seen from this equation that the speckle displacement along the line-scan camera depends on the rigid body displacements along x- and z-axis (a_x and a_z , respectively), the rigid body rotation around the y-axis (Ω_y) as well as the strain along the x-axis (ϵ_{xx}).

To separate the strain ϵ_{xx} from the rigid body motions, two line-scan cameras under angles $\pm\Theta$ are used, and the difference between the two speckle displacements is then only sensitive to ϵ_{xx} and a_z (Θ_S is set zero):

$$\Delta A_x = A_x(-\Theta) - A_x(\Theta) = 2L \epsilon_{xx} \tan \Theta + 2a_z \sin \Theta \quad (4.2)$$

If we neglect the out-of-plane displacement a_z , we can directly measure the true strain on the sample at a surface area with diameter of the illuminating laser beam, which is in the case of the He-Ne laser used equal to the width of our tensile specimens.

$$\epsilon_{xx} = \frac{\Delta A_x}{2L \tan \Theta} \quad (4.3)$$

The displacement A_x is detected by image correlation based on the covariance function. The algorithm realises a correlation based pattern matching (tracking) with the

salient feature that it guarantees equal sensitivity of displacement estimation for both directions. This is a feature of utmost importance since the total speckle displacement from the start of the experiment up to the current position is to be summed up over tiny contributions of motion between two successive exposures. This behaviour is guaranteed by the fact that the speckle pattern is modelled by a higher order polynomial which can then be differentiated analytically to finally give the desired displacement result.

Test measurements and verification of accuracy

We used the locally operating laser-speckle strain sensor now to survey stress-strain curves of our miniaturised tensile samples (fig. 4.1). The theoretical strain sensitivity of the sensor is of the order of 10^{-6} , but in practice one has to deal with imperfections of the geometrical set-up as well as cross-section reduction and change of specimen surface when straining until failure. The different contributions to experimental errors were investigated theoretically and experimentally by Schneider et al. [124].

However, our miniaturised specimens lead to additional difficulties and uncertainties which were carefully analysed within this work. In particular, the precision of the geometrical set-up as well as the influence of specimen mounting were investigated and sources of errors were suppressed wherever possible.

Displacement tests

It was shown by Schneider [124, 125] that a locally operating laser-speckle strain sensor can be used to determine stress-strain curves. However, because we use a laser source with smaller spot size leading to larger laser speckles, we first verified our system with displacement tests. As it can be seen from eq. 4.1 and fig. 4.2, pure in-plane displacement along the x-axis leads to a symmetric speckle displacement $A_x(\Theta) = A_x(-\Theta)$ on the two cameras. The accordance of the two values is therefore a check for the symmetry of the set-up as well as for the stability of the whole system and the image correlation algorithm. Thus, we conducted a series of displacement tests and analysed the difference between the resulting values of the two cameras.

The tests over a distance of 40 mm or 100 mm showed that the random difference of displacements observed by the two cameras can be kept as low as 2 μm (average of at least 20 measurements) when optimising the speckle intensity by the camera exposure time. If this optimisation is not done, the difference can be as large as 7 μm . The exposure time is optimised when the shoulder or slope of the individual laser speckles has a maximum resolution. This is because the image correlation algorithm is based on the derivative of the speckle pattern. A saturation or cutting-off of the peaks of the speckle intensities does not affect the image correlation due to the algorithm used in the present investigation.

In course of the displacement tests we recognized that the absolute displacement values measured by the optical sensor showed some discrepancy compared to the values

of the encoder of the tensile machine. A good accordance of these values is a proof for a precise geometrical set-up in terms of the absolute values of Θ and L . In fig. 4.3 one can see the displacement measured with the laser-speckle sensor versus the displacement measured with the tensile test machine. At first sight the line appears to be very straight but at a closer look variations from the linear behaviour are clearly visible (green graph in fig. 4.3). They are in the range of $\pm 20 \mu\text{m}$ and have a rather constant period.

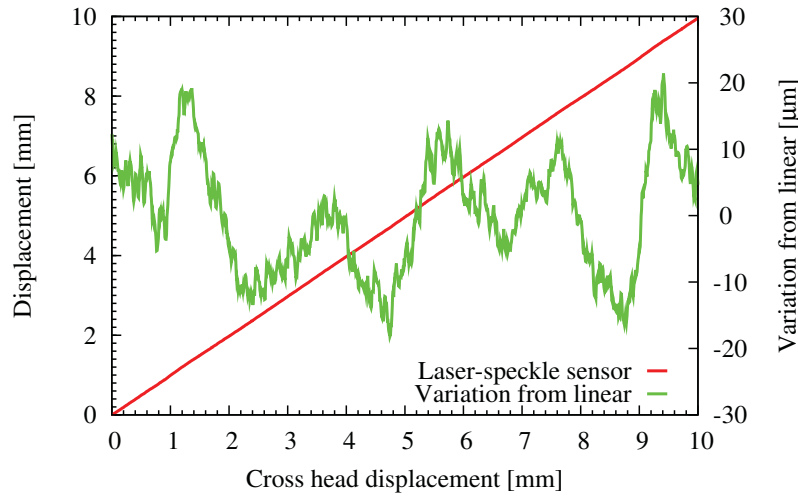


Figure 4.3: In-plane displacement test: Displacement measured by the laser-speckle sensor (average of the two camera values) and variations from the fitted linear slope.

A series of such measurements showed that the positions of the maxima and minima are not random but depend on the absolute cross head position only. Moreover, the effect is symmetric for the two cameras. Thus, we could conclude that the origin of this behaviour is a very slight tilting of the cross head around the y-axis of less than one tenth of a degree. The period is approximately 2 mm which corresponds to the thread pitch of the tensile test machine. Although this tilting could not be prevented it has no influence on the strain measurement due to the fact that its effect is symmetric on both camera planes and the strain measurement is based on the difference of the speckle displacement values of the two cameras.

In the long term, the accordance of the displacement values gained with the laser-speckle sensor and the encoder of the tensile test machine revealed a precise geometrical set-up, as shown in fig. 4.3.

Specimen mounting

Fig. 4.4 shows a small-sized sample mounted for a tensile test together with the incident laser beam. The specimen is fixed with four pins on its shoulders. Additional markers for a commercial video extensometer were placed on the holder close to the specimen.

The equipment and specifications for all the following tensile tests are summarised in table 4.1.

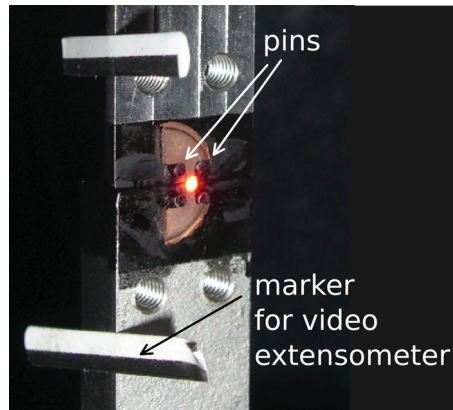


Figure 4.4: Experimental set-up: Mounting of the dogbone-shaped sample with four pins, incident laser beam of the speckle sensor and additional markers for the video extensometer.

Table 4.1: Used equipment and specifications for the tensile tests.

Tensile test machine	Messphysik ME30-1 1kN
Laser	HeNe-Laser, 5 mW, 0.6 mm spot size
Cameras	Eureca LPV-1024HT-8EPP, 1024 pixels (7.8 μm \times 125 μm)
Observation angle Θ	24°25'
Observation distance L	106 mm

The first investigation was to compare the results obtained by the laser-speckle sensor with results of a video extensometer measuring close to the sample on the holder. A direct strain measurement on the specimen with the video extensometer was not possible due to the small sample size.

The stress-strain curves obtained by the different strain measurement techniques from one and the same experiment on a copper sample are shown in fig. 4.5. One can see the clear improvement of the local laser-speckle measurement compared to both, strain measurement by the cross head displacement and by a video extensometer.

Also the values of Young's modulus (table 4.2) obtained from this test show the necessity of a strain measurement directly on the sample. Although the markings of the video extensometer are quite close to the specimen, the elongation of the specimen holder as well as the compliance of the pins have a tampering effect, and the obtained Young's modulus is far from literature values of copper (80 – 180 GPa, depending on the texture).

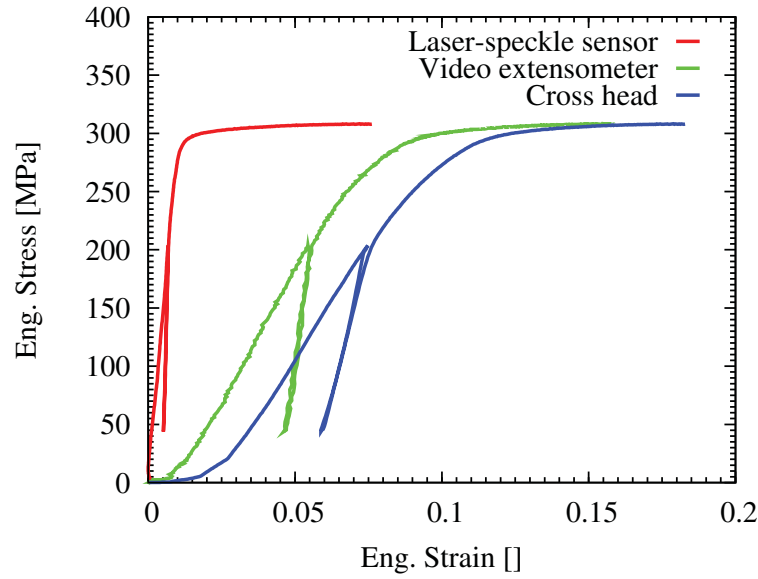


Figure 4.5: Tensile test of a miniaturised Cu specimen (including a load removal to measure Young's modulus): Comparison of strain measurement via laser-speckle sensor, video extensometer and cross head movement.

Table 4.2: Young's modulus obtained by different strain measurement techniques.

strain measurement technique	Young's modulus
local laser-speckle sensor	105 GPa
video extensometer	19 GPa
cross head displacement	12 GPa

The second investigation concerned the specimen mounting. Fig. 4.6 shows the influence of misalignment. If the laser illuminates not only the sample surface but also some part of the holder, the speckle pattern is a superposition of speckles from the samples which change their position upon straining and constant speckles from the holder. The resulting superposition speckle pattern shows strong intensity variations upon straining and the strain measurement becomes inaccurate. Therefore, a misalignment of the specimen has to be avoided through very careful adjustment. The absence of excessive intensity variations of the speckles during straining is a verification of a proper alignment.

After verifying the geometrical set-up by displacement tests, the laser-speckle strain sensor was applied to tensile test on HPT processed specimens.

4.3 Data evaluation and measurement accuracy

As shown in the previous section, the laser-speckle sensor is highly capable to directly and precisely measure strain during tensile tests. Anyhow, the measurement is quite local, restricted to the area of the sample which is illuminated by the laser beam. If

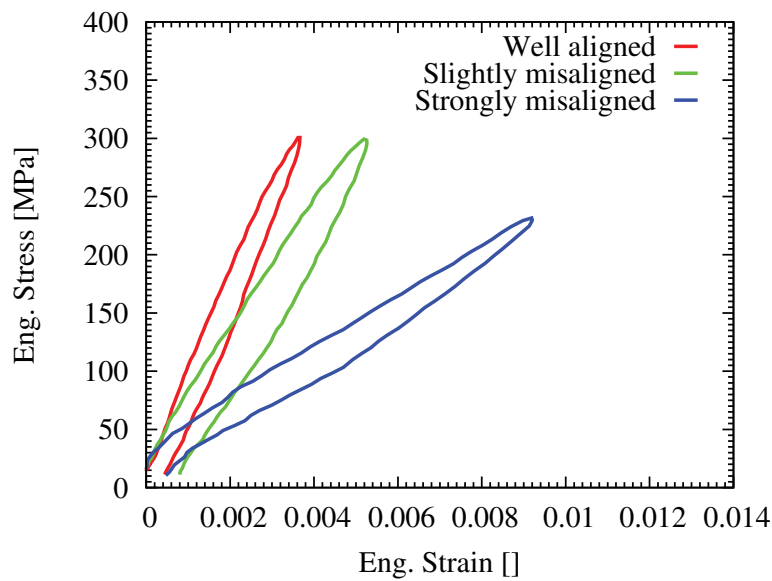


Figure 4.6: Dependence of the measured strain value on the specimen alignment. Three loading and unloading tests were performed using the same Cu specimen.

necking takes place beyond the ultimate tensile strength, any further deformation of the tensile specimen is located in the necking area. The laser can now illuminate either the necking area or any other part of the parallel gauge length. In all cases the strain data obtained by the laser-speckle sensor does not give the engineering strain for the whole gauge length.

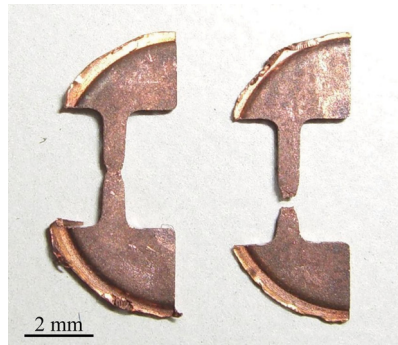


Figure 4.7: Picture of two Cu tensile specimens nearly fractured (left) and totally fractured (right).

The second possibility to measure the strain is to divide the change of the cross head position of the tensile machine (Δl) by the initial parallel gauge length ($l_0 = 2.5$ mm). As shown previously, this method is not precise enough and gives wrong Young's moduli by one order of magnitude. Anyhow, it is the only possibility to get the strain in the post-necking region of the tensile curve. To get the strain measurement by cross head movement a bit more precise, one has to measure the compliance of the tensile machine

(including the holder for sample mounting). Therefore, samples of the spring steel C75S have been deformed. This material has been used due to its high yield strength of more than 1 GPa and the high Young's modulus of ~ 206 GPa [126] which ensures linear elastic behaviour over a wide loading range. Using such samples the difference in displacement measurement (i.e. the error of the displacement measurement by cross head movement) depending on the applied load has been determined, see fig. 4.8. The linear part has been fitted and the obtained formula was used to correct displacement (and thereby also strain) data measured by the cross head movement of the tensile test machine. The results are still not good enough to determine Young's moduli but the measurement accuracy of the fracture strain is in the range of ± 1 percentage point.

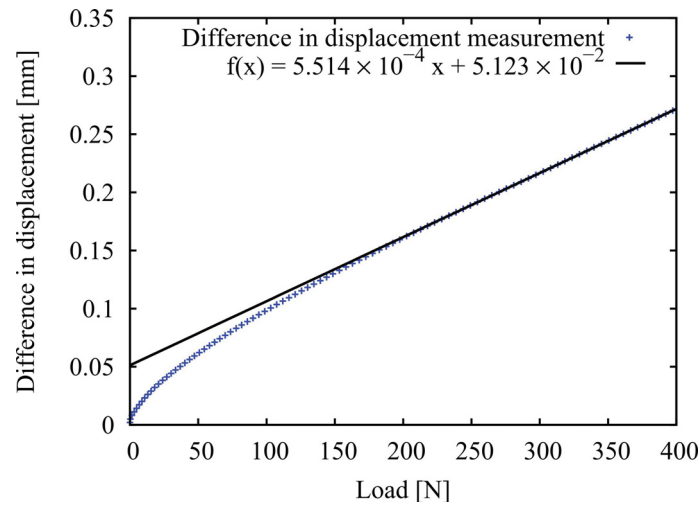


Figure 4.8: Calibration of the strain measurement by cross head movement: difference in displacement between laser-speckle sensor and cross head movement depending on the applied load.

The procedure to get the best possible overall engineering stress-strain curve is now the following: the strain of the first part of the curve up to the ultimate tensile strength is directly and very precisely measured by the laser-speckle sensor. In the second part, where necking takes place, the strain is determined from the cross head movement using the correction of the obtained displacement values.

Fig. 4.9 shows an example of two Cu-5at%Al tensile samples. When testing sample 1 the laser beam was located outside the necking region, in case of sample 2 directly inside the neck. It can be seen that beyond the UTS the strain values of the two samples obtained by the laser-speckle sensor differ extremely (dashed lines) while the curves obtained from the cross head movement show a good reproducibility.

The stress is measured with a commercial load cell. As the samples are quite small, the parallelism of the surfaces is very important. The cross-section area of each sample

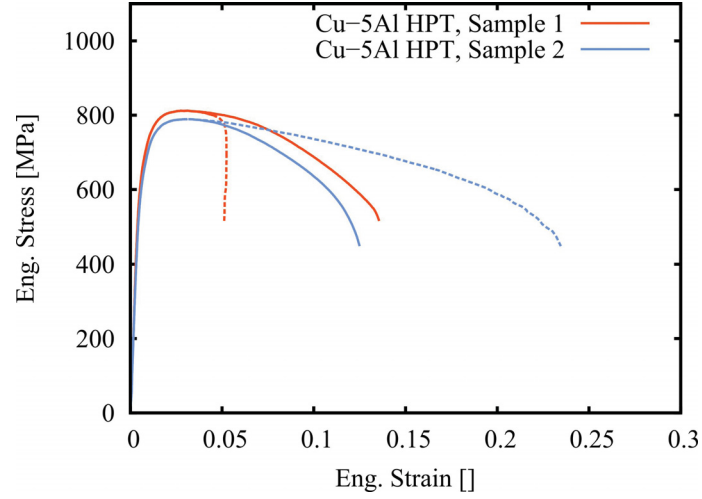


Figure 4.9: Tensile curves of two Cu-5at%Al samples. The solid lines are the engineering stress-strain curves obtained by a combination of laser-speckle and cross head measurements as described in the text. The dashed lines are the strain values received by the laser-speckle sensor when necking takes place. In case of sample 1 (red line) necking took place outside the measurement area while in case of sample 2 (blue line) the neck evolved in the measurement area.

is measured with an optical microscope and only samples meeting the requirement of parallel surfaces within $\pm 5 \mu\text{m}$ are used. This ensures that the uncertainty of the stress values is below 1%.

5 High cycle fatigue

5.1 Ultrasonic resonance fatigue testing

To reach the required number of cycles for the high or even ultra-high cycle fatigue regime, a high testing frequency is desired. This can be achieved by using an ultrasonic resonance fatigue testing system. A system working at 20 kHz performs 10^{10} cycles within a week, which is a marked contrast to a conventional 100 Hz testing device, which would require three years to reach this ultra-high number of loading cycles.

In an ultrasonic resonance fatigue testing system, a piezoelectric converter or shaker creates a mechanical vibration with a fixed frequency of 20 kHz and a selectable amplitude. Thereby, a longitudinal standing wave is introduced into the whole system. The system consists of the converter, an acoustic (amplifying) horn, an (optional) extension and the sample or a sample holder, see fig. 5.1.

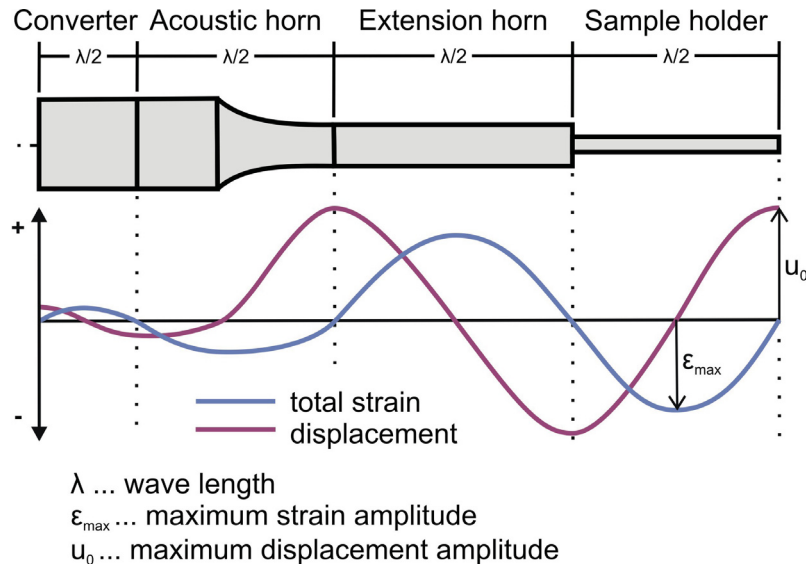


Figure 5.1: Sketch of the ultrasonic resonance fatigue testing system and distribution of displacement and strain (after [127]).

All parts of the system must have a length corresponding to half of the wave length. The speed of longitudinal acoustic waves in a long solid bar is given by:

$$c = \sqrt{\frac{E}{\rho}} \quad (5.1)$$

where E is the Young's modulus and ρ the density of the material. Moreover, $c = \lambda f$, with λ being the wave length and f the frequency, leading to the result that each part

of the ultrasonic resonance system must have a length l of:

$$l = \frac{\lambda}{2} = \frac{1}{2f} \sqrt{\frac{E}{\rho}} \quad (5.2)$$

The vibrations of the piezoelectric shaker introduce a sinusoidal wave of displacement. The strain is the derivation of the displacement, therefore the maximum of the strain amplitude is at the position of zero displacement. This is the case in the center of the sample holder.

A sample holder is only necessary when testing small-scaled specimens. If the size of the available sample material is as large as $\lambda/2$ (e.g. 9 cm in case of copper, according to eq. 5.2), one can use a whole sample instead of a sample holder.

The strain amplitude during each test can be set by adjusting the displacement amplitude which is created by the piezoelectric shaker. This can be selected within a certain range. Furthermore, this range can be shifted by choosing different acoustic horns which can increase or also decrease the strain amplitude by a certain factor depending on the geometry. The ratio of the cross-sectional areas of the two sides of the horn is thereby decisive.

Using an ultrasonic resonance fatigue testing system, the experiments are conducted under constant total strain amplitude – usually in the range of 10^{-4} or below. This is a strain range where the elastic part predominates, but a small part of the total strain amplitude is always plastic, otherwise the samples would not break in the end. Stanzl-Tschegg et al. [128] determined plastic strain amplitudes in ultrasonic fatigue by measuring the damping heat. They found out that the plastic strain amplitude is about two orders of magnitude smaller than the elastic one.

Monitoring the hysteresis loop and determining cyclic hardening or softening behaviour is not possible with this equipment.

Moreover, tests can only be conducted under symmetrical push-pull loading, meaning zero mean stress and a load ratio of $R = -1$. In principle it is possible to superimpose a non-zero mean stress but this would require further experimental efforts [129, p. 55].

5.2 Sample geometry

The sample geometry used for the high cycle fatigue tests can be seen in fig. 5.2. Disc-shaped HPT processed samples with a diameter of 10 mm were used. Two equal stripes were cut out of one disc by means of spark erosion at a radius of 2 mm. After polishing all four sides, the stripes had a width of 0.6 mm and a thickness of 0.2 mm. The thickness was small enough to ensure uniform straining, but large enough to avoid size effects (compare [130]). To measure free-standing samples, they were glued over a circular hole in the center of the sample holder. To ensure breaking of the samples in the center

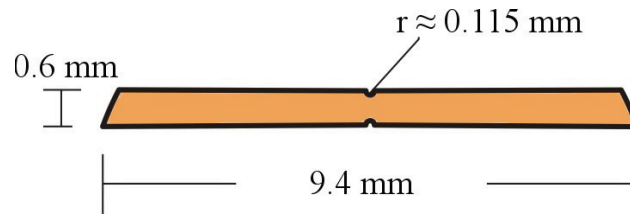


Figure 5.2: Sketch of the fatigue sample cut out of an HPT disc.

and not at the edge of the hole, it was necessary to introduce semi-circular side notches to the samples. These notches were also cut by spark erosion using the smallest possible current and thereby achieving the smoothest sample surface possible with this technique. The radius of the notches was about 0.115 mm.

The sample holder had a through circular hole with a diameter of 1.5 mm in the center (this is the position of maximum strain amplitude and zero displacement), see fig. 5.3. The sample was glued on the holder over the hole using Z70 strain gauge glue from HBM. A strain gauge (type 1-LY11-0.6/120 from HBM or similar) was glued at the side of the holder.

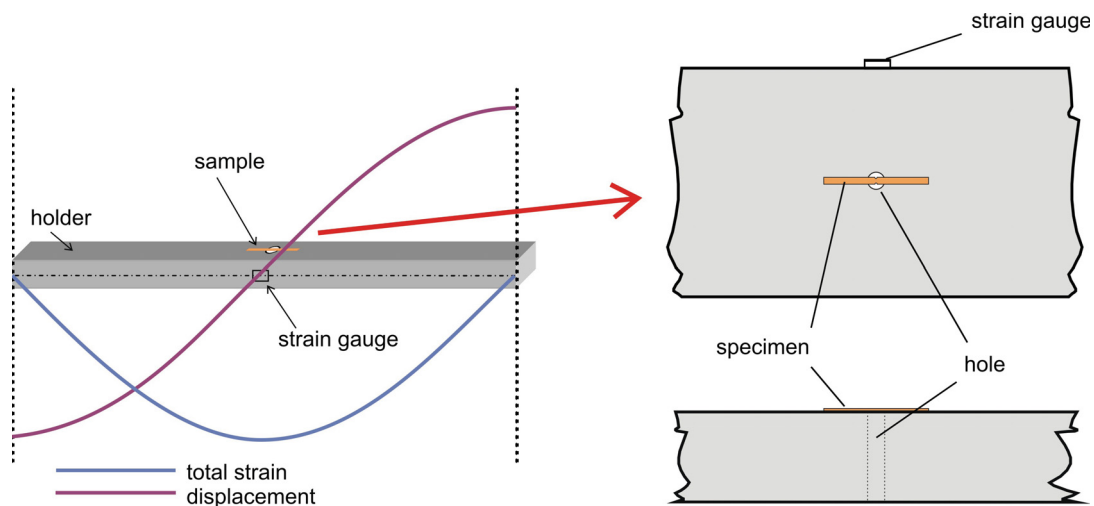


Figure 5.3: Sketch of the geometry of the sample holder with a sample glued on it.

Another part of the experimental set-up not shown in the sketches was a light microscope equipped with a video camera to observe the sample surface during testing. Thereby, it was possible to see the sample fracturing and to determine the number of cycles (via the measurement time) at which the sample did fail. This was also possible afterwards by examining the recordings.

Furthermore, the sample was cooled during testing by a blast of compressed air to prevent heating of the specimen due to the high frequency used.

5.3 Calibration and determination of stress amplitude

During each test, the strain on the sample holder was measured with a strain gauge. This strain value was calibrated to the strain on an unnotched sample leading to a calibration factor K_{specimen} . The notches of the sample cause a stress (and strain) concentration [47, p. 184ff]. For each sample the theoretical value of the stress concentration due to the notches (K_t) was calculated using the book of Peterson [51, p. 84]. The exact dimensions were measured in the light microscope. The strain on the sample is then given by:

$$\Delta\epsilon/2 = (\Delta\epsilon/2)_{\text{holder}} \times K_{\text{specimen}} \times K_t \quad (5.3)$$

As this total strain amplitude is nearly entirely elastic, one can get the stress amplitude from Hook's law:

$$\Delta\sigma/2 = E \times \Delta\epsilon/2 \quad (5.4)$$

Table 5.1: Names of the symbols used in eq. 5.3 & 5.4.

Symbol	Name
$\Delta\sigma/2$	stress amplitude
$\Delta\epsilon/2$	strain amplitude
E	Young's modulus
$(\Delta\epsilon/2)_{\text{holder}}$	strain amplitude on the holder
$K_{\text{specimen}} = \frac{(\Delta\epsilon/2)_{\text{unnotched sample}}}{(\Delta\epsilon/2)_{\text{holder}}}$	calibration factor
K_t	theoretical notch factor

Determination of K_{specimen}

A very small strain gauge of type EA-06-015DJ-120/LE with a measurement grid size of $0.51 \times 0.51 \text{ mm}^2$ from the company Vishay was glued on a Cu-stripe which had the same width and thickness as the samples, but no notches. This stripe was then glued on the sample holder over the hole as if it would be a test specimen. Different loading amplitudes have been applied and the strain values on the sample holder and on the calibration sample have been determined simultaneously. The results of this calibration, which has been conducted on two samples, can be seen in fig. 5.4 together with a sketch, which shows the positions of the strain gauges. The calibration factor K_{specimen} determined this way was 1.6.

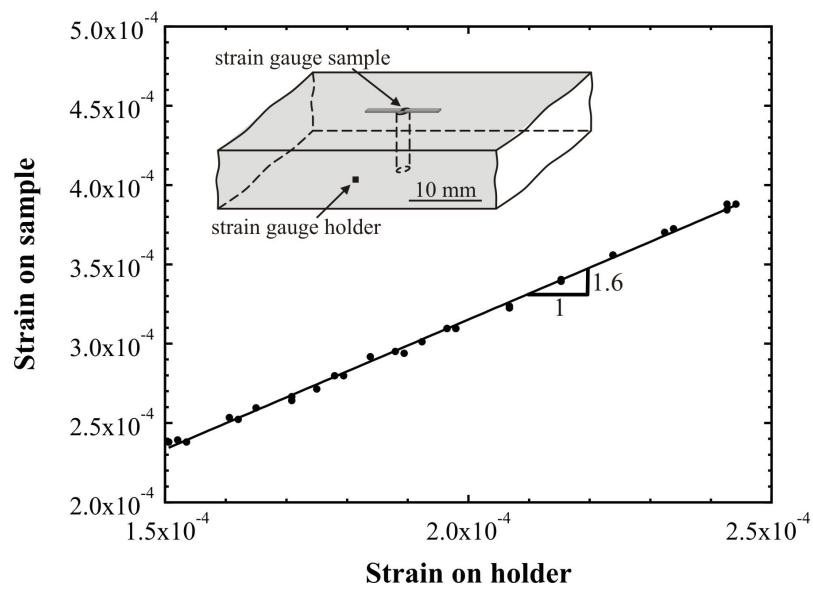


Figure 5.4: Relationship between the strain value of the miniaturised fatigue specimen to the specimen holder (calibration curve) [23].

6 Fatigue crack growth

Fatigue crack growth was measured in a similar way as the fatigue strength. Again, the ultrasonic resonance fatigue testing system was employed, but the geometries of the samples and the holder were different.

6.1 Sample geometry

The HPT processed samples had a diameter of $W = 10$ mm and were polished down to a thickness of about 200 μm . Thereby a mirror-like surface was obtained. An elliptical notch was introduced in the center of the sample by using a proper spark-erosion electrode. This was made of copper and manufactured by the company C. & H. Wöls GmbH, Köttingbrunn, according to our specifications. The dimensions were $l = 1.5$ mm and $b = 0.5$ mm, compare fig. 6.1. According to the book of Peterson [51], this geometry results in a stress concentration factor K_t of approximately 6 at the edges of the elliptical notch. Therefore, the crack which evolves during cyclic loading at these points has to grow a certain distance until the stress field of the notch is negligible. A formula for this length (a_0) is given in [50, p. 401]:

$$a_0 = \frac{l/2}{1 + (1.122 K_t)^2} + l/2 = \frac{1.5/2}{1 + (1.122 \times 6)^2} + 1.5/2 = 0.766 \text{ mm.} \quad (6.1)$$

Numerical solutions of this problem show that this value can be quite larger [50] and to ensure not to have an influence of the stress concentration of the notch, crack growth measurements were started not before the crack reached a length of $a = 1.5$ mm. Please keep in mind that the crack length is always measured from the center of the elliptical notch.

Furthermore, crack growth measurements were stopped at the latest when the crack reached a length of $a = 2.5$ mm to avoid an influence of the finite sample width.

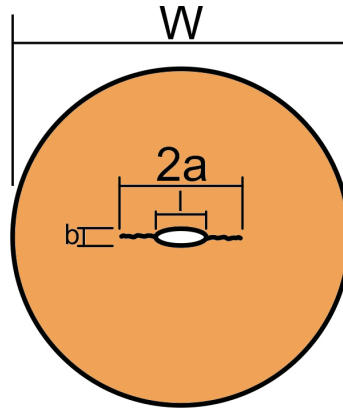


Figure 6.1: Sketch of the HPT sample prepared for crack growth measurement.

6.2 Experimental set-up

The sample holder which was part of the ultrasonic resonance testing system described in section 5.1 had a length of 125 mm and a cross-section of $20 \times 8 \text{ mm}^2$. Grooves (width: 2 mm, depth: 1 mm) were made in the center of the holder at the position of maximum strain on the top as well as the bottom side. To fix the sample to the holder, Z70 strain gauge glue from HBM was used (single component, cold curing adhesive made of cyanacrylate [131]). The glue was dried under slight pressure over night at room temperature. The sample was glued over the groove to ensure a free standing measurement area, see fig. 6.2.

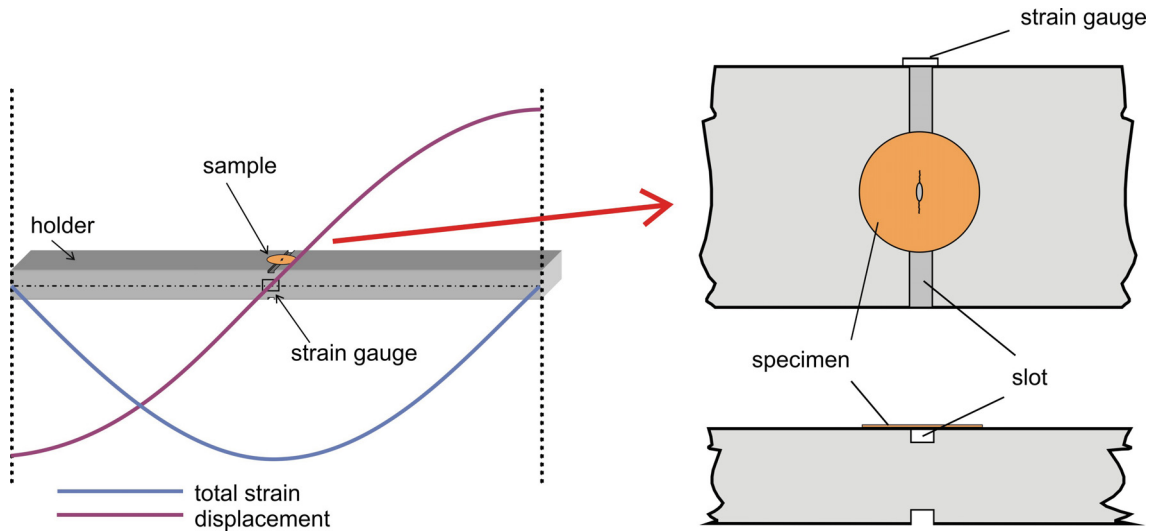


Figure 6.2: Sketch of the geometry of the sample holder with a sample glued on it.

During testing, the sample surface and the crack were observed using a travelling light microscope. After the crack has reached the minimum length for the crack propagation experiments, the fatigue loading was stopped periodically and the crack length was determined. Therefore, the software measured the way the light microscope had to travel from the position of the former crack tip to the point where the new crack tip is in the center of the picture. A photograph of the experimental set-up is shown below (fig. 6.3).

It can also be seen from this picture that the acoustic horn used in these experiments was straight, i.e. it does not increase or decrease the strain amplitude. An extension horn was not used. Furthermore, cooling by compressed air was performed to prevent heating of the sample.

6.2.1 Calibration and determination of stress amplitude

During each test, the strain was recorded with a strain gauge (type 1-LY11-0.6/120 from company HBM, measurement grid $0.6 \times 1 \text{ mm}^2$) which has been glued on the side surface of the sample holder. Due to the used geometry of the grooves, the strain on the sample

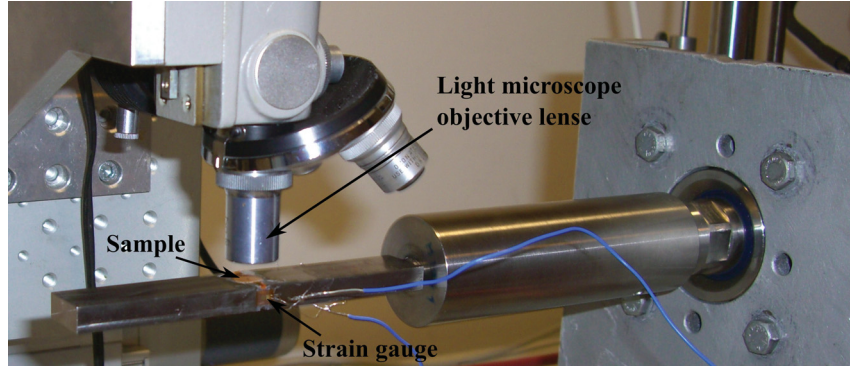


Figure 6.3: Photograph of the experimental set-up consisting of the ultrasonic fatigue testing system including sample holder and sample, as well as a light microscope for crack length measurement and a strain gauge on the sample holder.

is larger than the strain measured on the holder and therefore a calibration factor had to be determined. Thus, a sample without elliptical notch was glued onto the holder and a strain gauge was glued on top of it. Now the strain value of the sample was compared to the strain on the holder at different loading amplitudes. Data from two measurements (two samples and two holders with the same geometry) was collected and the result can be seen in fig. 6.4. The calibration factor K_{specimen} determined this way was $1.644(\pm 0.008)$.

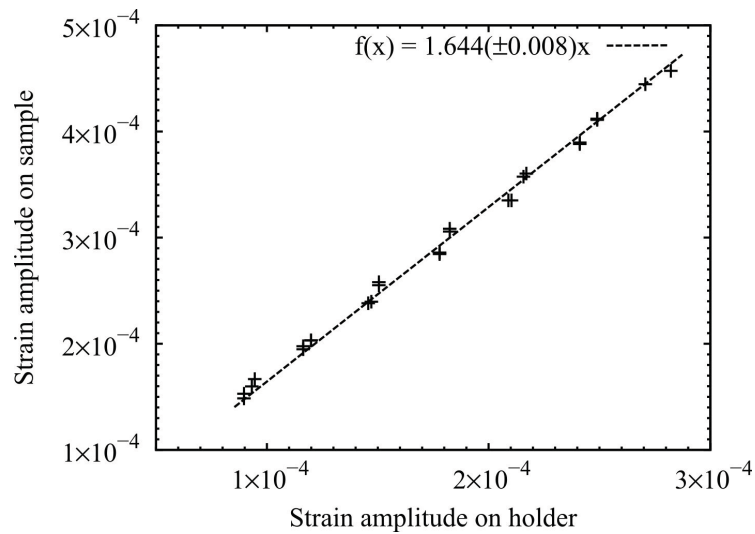


Figure 6.4: Relationship between the strain value of the miniaturised crack growth specimen to the specimen holder and fitted line (calibration curve).

The stress amplitude was determined like in section 5.3:

$$\Delta\sigma/2 = E \times (\Delta\epsilon/2)_{\text{holder}} \times K_{\text{specimen}} \quad (6.2)$$

PART III

RESULTS & DISCUSSIONS

The results of this thesis will be presented and discussed in three chapters. The first and until now unpublished part deals with the tensile strength and ductility of HPT processed Cu and Cu-Al alloys. The alloys which were chosen due to their low stacking fault energy contain a high number of deformation twins after SPD processing and are believed to exhibit high strength and good ductility simultaneously (e.g. [16–19]). However, there are several open questions as will be discussed in the beginning of this chapter. A possible influence of short-range order in Cu-Al alloys with 10at%Al or more has for example not been considered so far. This is one of the subjects of this investigation.

More important, not only deformation twins but also a large number of grain boundaries and dislocations are present in the materials. It will be shown that the strength of HPT processed Cu-Al alloys can be reasonably discussed in terms of the dislocation density. Concerning the uniform elongation in tension, it will be shown that the SPD technique and the dislocation arrangement obtained thereby have by far a larger influence than the stacking fault energy or the twin density.

The other two chapters are represented by two papers which have already been published in peer-reviewed international journals.

The first paper (chapter 8) deals with the crack propagation behaviour of high and commercial purity HPT Cu whose fatigue strengths have been determined in my Diploma thesis [22]. Beside these two Cu materials with different purities also high purity HPT Cu with a bimodal grain size distribution is investigated for its fatigue strength as well as crack propagation rate. The results of my diploma thesis which were already summarised in section 3.3.2 can be seen as the motivation of this work. The aim was to expand the knowledge from high cycle fatigue to fatigue crack growth and to focus on the structural parameters of the different HPT materials and their influence on the cyclic mechanical properties. Consequently, the threshold stress intensity factor range and near-threshold crack propagation rates have been determined for the HPT processed materials as well as for coarse grained (CG) copper. Furthermore, the microstructure in the vicinity of the crack was examined, and it will be shown that grain coarsening during cyclic loading not only affects the fatigue strength but also the fatigue crack propagation.

The second paper (chapter 9) focuses on the influence of the microstructural stability on the fatigue and crack propagation behaviour of HPT Cu. It will be shown that grain

coarsening in the vicinity of a crack retards the fatigue crack propagation which is, nevertheless, in HPT materials faster than in CG Cu. The occurrence of grain coarsening during cyclic loading in the HCF regime as well as during crack growth in HPT Cu of different purity and grain size distribution is being discussed with respect to the thermal stability of the microstructure in terms of annealing temperature and stored energy.

A subsequent summary will recapitulate the results of the three parts and an outlook will raise some so far unsolved questions stimulating further interesting investigations.

7 Strength and ductility of HPT processed nanostructured Cu and Cu-Al alloys

7.1 Introduction and motivation

Copper with nanoscale growth twins is reported to exhibit a high strength, which is comparable or even higher than that of SPD Cu, in combination with a uniform elongation higher than that of the nanograined counterpart [98, 99, 132]. According to literature [100] the different interaction possibilities between the highly coherent twin boundaries and moving dislocations are responsible for this promising combination of properties. The good ductility is also associated with the initially fairly low dislocation density of the materials which leads to an effective strain hardening [98]. Furthermore, it is supposed that the dislocation density during tensile straining increases only slowly because the numerous twin boundaries are able to absorb the moving dislocations [99].

As these materials were produced by electro-deposition, they were only available in form of foils with a thickness below 50 μm . An attempt to produce larger samples of nano-twinned material is the generation of twin boundaries by SPD deformation.

It has been shown for different pure metals [11] and for Cu based alloys [12, 13, 20] that the twin density or twin fault probability of SPD processed materials increases with decreasing stacking fault energy (SFE). The reason for this correlation is the larger splitting distance of partial dislocations in materials with low SFE leading to deformation by mechanical twinning instead of dislocation glide.

Adding Al to Cu considerably decreases the SFE of the material [133]. Therefore, and because of the promising reports about the effects of growth twins, several publications deal with the tensile properties of Cu-Al alloys deformed by SPD techniques like ECAP [16–18], HPT [19, 134] or LNT-DPD (“liquid nitrogen temperature dynamic plastic deformation”: high strain rate compression at 77K) and quasi-static compression (QSC) [15]. A summary of the materials and processing methods used in these publications is given in table 7.1 and in more detail in appendix D.

It should be noted that Cu-Al alloys with an Al content of 10at% or more show a tendency to short-range ordering (SRO) [135]. A possible influence of SRO to the mechanical properties of SPD Cu-Al alloys has not been considered so far. The solid solution limit in this alloy system is at an aluminium content of approximately 20at% [136].

The compared papers concordantly state that with decreasing SFE the twin density of SPD processed Cu-Al alloys increases and the grain size decreases. It is argued that the grain refinement mechanism changes from a dislocation-based mechanism, where

Table 7.1: Summary of investigated materials and processing methods of available literature on tensile properties of SPD nanostructured Cu-Al alloys. More details of the cited papers concerning grain sizes and tensile properties can be found in appendix D.

Publication	Investigated Cu-Al alloys (at% Al)	SPD processing	Equivalent strain
An2008 [16]	2.3, 7.2, 11.6	ECAP: 1 pass, RT	~ 1
Qu2009 [17]	5, 8, 16	ECAP: 4 or 2 passes (Cu-16Al), B_c , RT	4.6 (2.3)
An2011 [19]	0, 2.3, 5, 8, 16	HPT: 6 GPa, 5 rotations, RT	max. 128
Zhang2011 [15]	0, 1.17, 1.75, 2.3, 3.5, 5, 10	LNT-DPD (strain rate 10^3 s^{-1} , 77K)	2 (Cu-10Al: 1.7)
Zhang2011 [15]	0, 1.17, 1.75, 2.3, 3.5, 5, 10	QSC (quasi-static compression) at RT	2 (Cu-10Al: 1.7)
Huang2012 [18]	0, 2.3, 7.2, 11.6	ECAP: 8 passes, B_c , RT	8

the fragmentation of the original grains occurs by the formation of dislocation cells, to deformation by twinning and intersection of the twins [17]. The second mechanism is reported to occur below a SFE of about 28 mJ/m^2 (being the SFE of Cu-5Al) [18]. However, looking at measured twin densities, which are only available in the paper by Zhang et al. [15], the picture is not that clear. In case of room temperature deformation the authors report an increasing volume fraction of nanoscale twins/matrix lamellae starting at about 2.3at%Al but in case of SPD processing at high strain rate and liquid nitrogen temperature (LNT-DPD) pure Cu has the highest volume fraction of twin/matrix lamellae, and the value slightly decreases with increasing Al content.

Beside the SFE, also the process parameters according to the Zener-Hollomon parameter Z (eq. 1.1) influence the deformation and thereby the microstructure achieved by SPD. It was shown for pure Cu that deformation with an increased Zener-Hollomon parameter leads to smaller grain size, higher dislocation density, higher strength and a higher volume fraction of deformation twins [14]. Thus, a higher value of Z is supposed to have the same effect on strength and twinning probability as a lower SFE [15].

It is obvious from the literature [15–19] that a higher alloy content as well as a higher Zener-Hollomon parameter during SPD processing of Cu-Al alloys lead to a stronger grain refinement and an increased **strength**. This is also supported by investigations on Cu-Zn alloys [12, 20] and Cu-Mn alloys [137], where it was shown that also in these systems the strength of SPD processed materials increases with increasing alloy content. Cu-Mn is especially interesting because the SFE in this alloy system is nearly constant. The reason for the increased grain refinement in alloys is due to the limitation of the dislocation and grain boundary mobility by the alloy atoms and hence better thermal stability of alloys compared to pure metals, this way decreasing dynamic and static recrystallisation [27, p. 320ff].

When comparing the grain size of SPD Cu-Al alloys with the ultimate tensile strength (UTS) or with the yield strength, it can be seen that surprisingly the same grain size leads

to the same strength, regardless of deformation technique and parameters chosen, and alloy content as it is depicted in fig. 7.1. Such a comparison is also seen in [15, 18, 19] and the Hall-Petch equation is used to explain this behaviour [15]. However, the Hall-Petch coefficient for an alloy is generally different to the one of the pure material [138, p. 144]. An increase of the Hall-Petch coefficient as well as of the friction stress with increasing alloy content was shown for several systems, e.g. for Cu-Al [139–141], Cu-Ni [139], Ni-C [142], and Cu-Ti [143]. The Hall-Petch coefficient of Cu-15Al determined by Nakanishi and Suzuki [139] for example is $0.5 \text{ MPa}\sqrt{\text{m}}$ compared to only $0.11 \text{ MPa}\sqrt{\text{m}}$ for pure Cu.

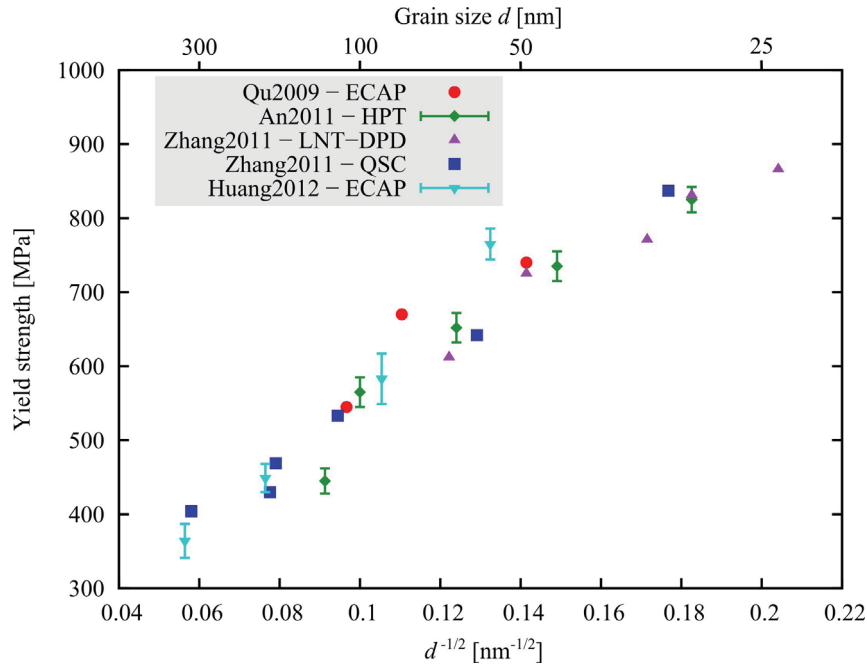


Figure 7.1: Comparison of yield strength and grain size (d) for pure Cu and for different Cu-Al alloys from available literature [15, 17–19]. (Detailed data in appendix D.)

Thus, the question arises if the Hall-Petch relation is really suitable to explain the strength obtained in SPD processed Cu-Al alloys. The Hall-Petch effect is typically observed in well-annealed coarse grained materials and the pile-up of dislocations at the grain boundaries is the most common theoretical explanation [32, p. 434f][144]. It has been shown several times (e.g. [10, 12, 145–147]) that in deformed and nanostructured materials deviations from the Hall-Petch behaviour are observed. Above all, the particularly high dislocation density in SPD processed materials has to be taken into account [12, 148, 149]. However, values of the dislocation densities of SPD Cu-Al alloys are not given in the literature so far [15–19].

Concerning the influence of alloy content or stacking fault energy in SPD processed Cu-Al alloys on the **ductility**, namely the uniform elongation in tension, the picture is even less clear.

A higher uniform elongation is reported for SPD materials with lower SFE [16–19] – although the values are quite small and in the range of 2% to 4%. It is argued that the better ductility is due to a higher strain hardening rate, which is caused by twins and stacking faults which “offer room for dislocation storage and suppress dynamic recovery” [17].

The paper by An et al. [19] reports an optimum stacking fault energy – the uniform elongation increases with decreasing SFE up to Cu-8Al but then decreases for Cu-16Al. It is stated that the grain size in the latter material (30 nm) is too small to permit storage of defects during tensile straining.

Unfortunately, the strain measurement during tensile testing is not described in any of the papers, except of the publication by Zhang et al. [15]. Especially in case of the HPT processed samples with a gauge length of only 2 mm [19, 134] very careful strain measurement is needed. When comparing the plotted tensile curves with the average values of the uniform elongation given in the papers [16–19, 134], it seems that the elastic part of the stress-strain curve is always included in the values of the uniform elongation. Subtracting the elastic part reduces the values of the uniform elongation by approximately 0.5 – 1 percentage point. The trends (increase or decrease of the uniform elongation with increasing SFE) stay thereby mainly the same but become considerably smaller.

The available literature data are plotted in fig. 7.2. It can be seen that there is no unambiguous correlation of the uniform elongation with the SFE. Also plotting the uniform elongation against grain size or strength would not reveal such a correlation.

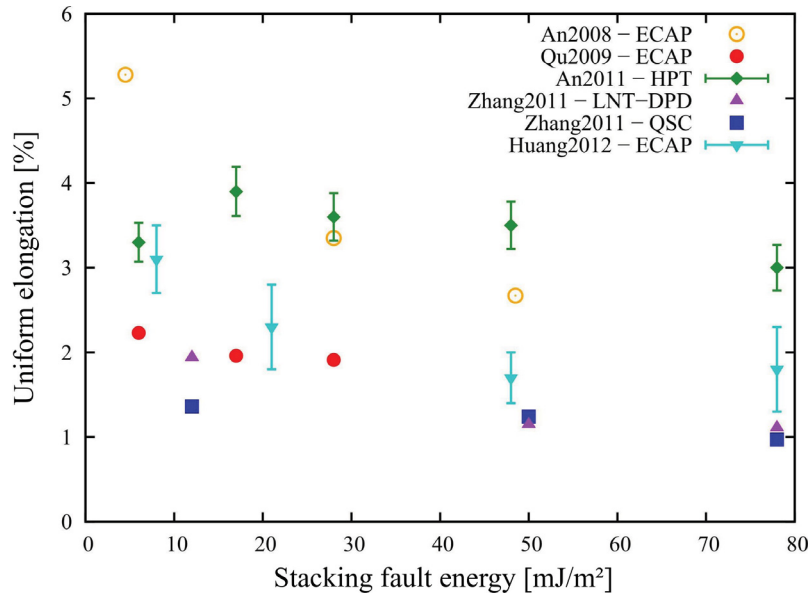


Figure 7.2: Comparison of uniform elongation (including the elastic part of the tensile curve) and stacking fault energy for Cu and different Cu-Al alloys from available literature [15–19]. (Detailed data in appendix D.)

A simultaneous increase of strength and ductility by decreasing the SFE was reported in SPD processed Cu-Zn alloys [20, 21]. Differing results are reported in a paper investigating Cu-Mn alloys deformed by die-forging [137]. Although the SFE in this alloy system stays nearly constant (at around 40 mJ/m²) and the measured twin density was very low, an increase of uniform elongation with increasing Mn content was observed (beneath the increase of strength). It is argued that this behaviour is due to short-range order leading to a higher work hardening rate. Unfortunately, no values of grain sizes or degree of SRO are given in the paper.

The values of the uniform elongation are in the range of 2.2% – 3.8% in case of the Cu-Zn alloys [20, 21] and between 0.5% and 1.25% in case of Cu-Mn [137], in both cases including the elastic part of the tensile curves.

On the basis of this literature review, the aim of the current investigation was:

- to measure the tensile properties – especially the yield strength and the uniform elongation – of HPT processed Cu and Cu-Al alloys. The direct strain measurement using the laser-speckle sensor is used to get reliable results of the uniform elongation.
- to evaluate the SRO in HPT processed Cu-Al alloys and to determine if SRO has any influence on the mechanical properties of the alloys.
- to perform the HPT processing at a higher value of Z , i.e. at liquid nitrogen temperature, and to investigate the influence of this processing parameter on the tensile properties.
- to determine dislocation density, twin probability and domain size of the HPT processed Cu-Al alloys by X-ray profile analysis and to clarify the influence of these parameters on the tensile strength.
- to combine own and literature data on the uniform elongation of SPD processed Cu and Cu-Al alloys to determine the influence of SFE, twins and processing parameters and to critically inspect the conclusions drawn in the papers summarised above.

7.2 Investigated materials and measurement methods

Pure Cu (99.99%), Cu-5at%Al and Cu-15at%Al were first cut into discs with 8 mm diameter and approximately 0.7 mm height. The alloys were then annealed at 550°C for one hour and quenched from 500°C into water. Pure Cu was annealed at 550°C for one hour and furnace cooled. HPT processing was performed at room temperature and at liquid nitrogen temperature (77K). Five rotations were done at an applied pressure of 6 GPa.

The different alloys were chosen due to their different stacking fault energies (SFE), the values are given in table 7.2.

Table 7.2: Stacking fault energies (SFE) of the investigated materials [150]. It should be noted that different values of the SFE of pure Cu exist the literature, ranging from 40 mJ/m² [27, p. 243] to 78 mJ/m² [19].

Material	SFE [mJ/m ²]
Cu	45.5
Cu-5Al	24.5 ± 0.5
Cu-15Al	5.5 ± 0.2

Average values of the tensile properties of HPT processed samples were gained from four to six stress-strain curves. In case of the quenched materials, only two tests have been done. The tensile tests were performed at a constant cross head speed of 1 µm/s resulting in an initial strain rate of $4 \times 10^{-4} \text{ s}^{-1}$. The dog-bone shaped samples had an average cross-section area of $0.8 \times 0.3 \text{ mm}^2$ and a parallel gauge length of 2.5 mm. Two samples were cut out of one polished HPT disc by spark erosion with the gauge length being off-centered at a radius of approximately 2.5 mm as shown in section 4.1. The strain was measured directly with a laser speckle-based strain sensor described in detail in chapter 4. The engineering stress was calculated using a load cell with 1 kN maximum load and the exact dimensions of each individual sample as measured by light microscopy.

Short-range order and defects were investigated by differential scanning calorimetry (DSC) using a NETZSCH DSC 204, the heating rate was 20 K/min. Discs with 6 mm diameter were therefore cut out of the HPT discs off the center.

To determine domain size, dislocation density and twin fault probability, X-ray diffraction measurements were performed in reflection geometry at the synchrotron ELETTRA in Trieste (Italy) using monochromatic radiation with a wave length of approximately 0.155 nm. The beam size was $200 \times 500 \text{ µm}^2$ and the measurements were conducted at a radius of 3 mm of the HPT discs. The detected X-ray profiles were analysed by the convolutional multiple whole profile (CMWP) fitting algorithm as given in detail in [151–153]. The domain size, which represents the dislocation cell or subgrain size in plastically deformed materials, is given as an area weighted average value. Grain sizes determined from electron microscopy pictures are usually larger [12].

Microhardness measurements were done using a Vickers indenter type MHT-4 PAAR with an indentation force of 1 N applied for 10 s. To get an average value, 7 indentations were done in case of the annealed materials and at least 10 values were measured at a radius of 3 mm in case of the HPT processed materials.

Scanning electron microscopy (SEM) investigations were done on mechanically polished samples using a Zeiss Supra 55 VP equipped with a detector for backscattered electrons.

7.3 Results

The materials before HPT can be characterised as follows: the grain sizes are large (roughly speaking between 50 μm and 500 μm) and the strength increases with increasing alloy content. The ultimate tensile strength is approximately 210 MPa for Cu, 280 MPa for Cu-5Al and 300 MPa for Cu-15Al. Details about microstructure and strength of the as-quenched materials can be found in appendix B.

7.3.1 Microstructure of HPT processed Cu & Cu-Al alloys

In case of pure Cu and Cu-5Al processed by HPT at room temperature (RT) it was possible to determine the **grain size** in the SEM using the backscattered electron detector. The grain sizes obtained from these pictures by the line intercept method are summarised in table 7.3. In case of Cu-5Al HPT processed at 77K and HPT Cu-15Al the grain sizes are too small to see the individual grains in the SEM.

The **domain sizes** evaluated by X-ray profile analysis are also specified in table 7.3. The measurement accuracy of these values is in the range of 10-20% [149].

Table 7.3: Grain sizes and domain sizes of the investigated materials as determined by SEM micrographs and XRD analysis, respectively.

Material	Grain size [nm]	Domain size [nm]
Cu, HPT RT	224 ± 43	
Cu, HPT 77K	123 ± 20	
Cu-5Al, HPT RT	86 ± 21	78
Cu-5Al, HPT 77K		65
Cu-15Al, HPT RT		79
Cu-15Al, HPT 77K		38

The **twin fault probabilities** of the alloys determined by XRD are given in table 7.4. In case of Cu-15Al processed by HPT at RT it was not possible to get a reliable value. However, the other values confirm the trends already reported in literature. They show that a lower stacking fault energy as well as a lower processing temperature lead to a higher twin density.

Pure Cu was not measured within this work, but a paper by Balogh et al. [12] shows that HPT processing (with the same strain and pressure) of pure Cu at RT doesn't result in a detectable twin density.

Table 7.4: Twin fault probability evaluated by XRD analysis.

Material	Twin fault probability [%]
Cu-5Al, HPT RT	1.2
Cu-5Al, HPT 77K	2.1
Cu-15Al, HPT 77K	3.5

The **dislocation densities** of the alloys were also gained from XRD line profile analysis assuming an outer cut-off radius of the dislocation strain fields of 8 nm. The results are summarised in table 7.5. For pure Cu the value was taken from a previous publication of our group [4]. It can be seen that the dislocation density increases with increasing alloy content as well as with decreasing processing temperature.

Table 7.5: Dislocation density determined by X-ray profile analysis.

Material	dislocation density ρ [m^{-2}]
Cu, HPT RT	4×10^{15} [4]
Cu-5Al, HPT RT	1.6×10^{16}
Cu-5Al, HPT 77K	2.0×10^{16}
Cu-15Al, HPT RT	2.1×10^{16}
Cu-15Al, HPT 77K	3.3×10^{16}

The results of the DSC investigations shown in fig. 7.3 are used to examine the **short-range order**. In case of pure Cu (fig. 7.3a) and Cu-5Al (fig. 7.3b) one single exothermic peak due to the annealing of defects can be seen. In both cases the peak temperature is shifted to lower values for the samples deformed at 77K. In these cases also the peak areas are larger. This means that deformation at the lower temperature leads to a higher number of defects and less thermal stability of the microstructure. Furthermore, the thermal stability of Cu-5Al is markedly enhanced compared to pure Cu. From the DSC scans of the second runs which are shown in appendix C it can be concluded that pure Cu and Cu-5Al do not exhibit short-range order at all.

Cu-15Al (fig. 7.3c) shows a more complex behaviour. Only the peak at about 350°C is due to the annealing of defects and connected to a decrease of hardness. Heating up the material to a temperature below this peak (320°C) leads to an increase in microhardness from 304 ± 4 to 334 ± 7 in case of a sample processed by HPT at RT. Therefore, it can be concluded that the first peak is due to the formation of short-range order which is associated with order hardening [135, 154]. This result implies that the HPT processed samples without any heat treatment possess no SRO due to the quenching and the large degree of deformation, which are both known to decrease the amount of SRO.

Thus, short-range order doesn't play a role in the investigation of HPT processed Cu-5Al and Cu-15Al. This issue is in more detail discussed in appendix C.

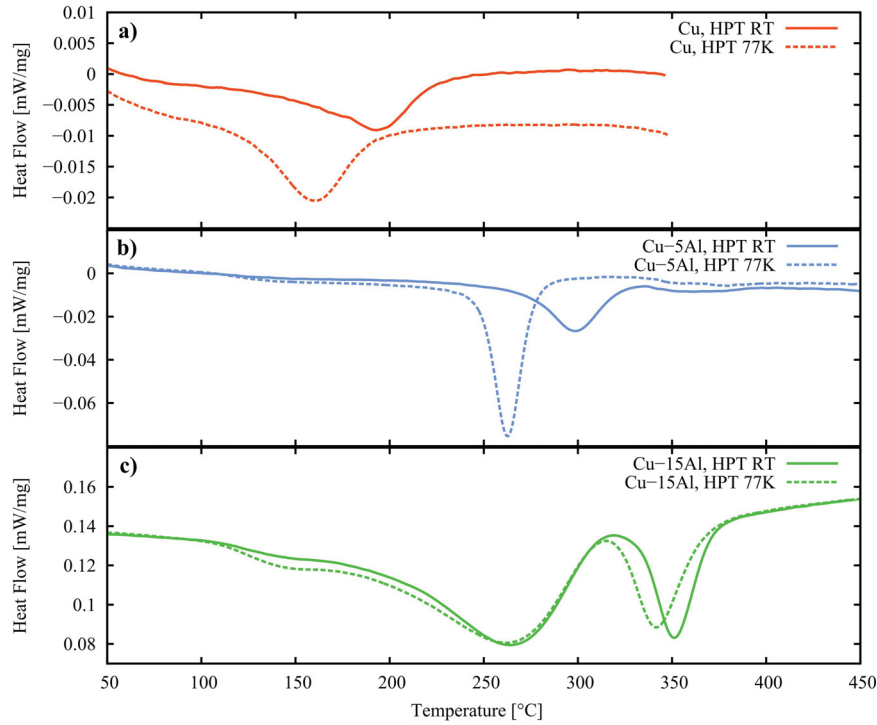


Figure 7.3: DSC scans of (a) pure Cu, (b) Cu-5at%Al and (c) Cu-15at%Al (first-heating curves, exothermic down). The curves from the second DSC runs look the same those from the as-quenched state (fig. C.1 in the appendix).

7.3.2 Strength and ductility

Exemplary engineering stress-strain curves obtained by testing micro-tensile specimens can be seen in fig. 7.4, the average values and standard deviations of strength and ductility measures gained from several specimens are summarised in table 7.6.

Table 7.6: Tensile test results: yield strength ($\sigma_{0.2}$), ultimate tensile strength (UTS), uniform elongation and total elongation. Always average value and standard deviation.

Material	$\sigma_{0.2}$ [MPa]	UTS [MPa]	ϵ_{unif} [%]	ϵ_{total} [%]
Cu HPT@RT	375 ± 23	510 ± 16	2.6 ± 0.4	17 ± 2
Cu HPT@77K	407 ± 37	576 ± 14	3.1 ± 0.3	20 ± 4
Cu-5Al HPT@RT	588 ± 74	784 ± 16	3.0 ± 0.7	15 ± 2
Cu-5Al HPT@77K	559 ± 75	835 ± 18	3.1 ± 0.6	15 ± 3
Cu-15Al HPT@RT	747 ± 86	948 ± 29	2.1 ± 1.0	9 ± 2
Cu-15Al HPT@77K	718 ± 55	977 ± 29	2.3 ± 0.6	8 ± 1

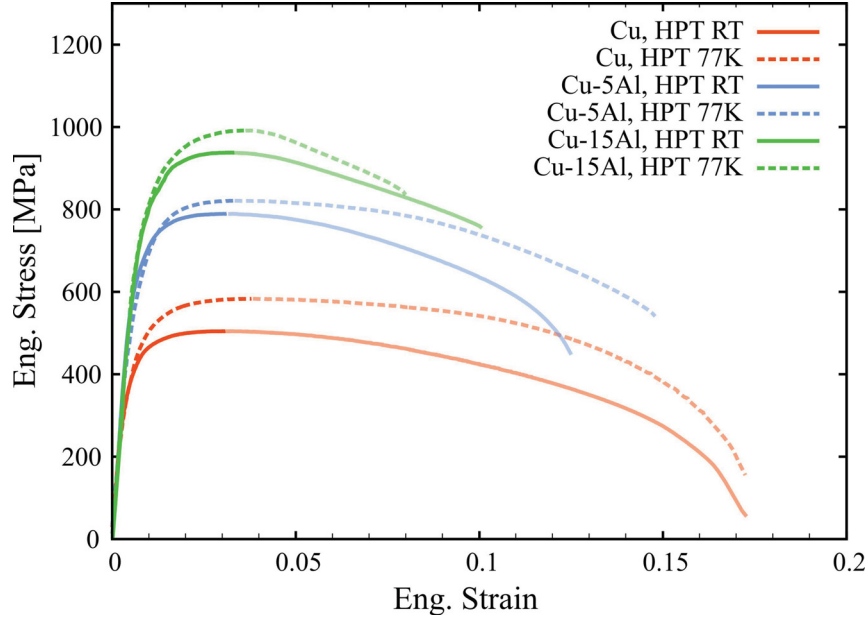


Figure 7.4: Exemplary tensile test curves of the HPT processed materials. The bold parts of the tensile curves up to the ultimate tensile strength are directly measured by the laser speckle strain sensor. The parts of the curves where necking takes place are plotted with thinner lines and are gained from the cross head movement of the tensile machine.

It can be seen that a higher alloy content as well as processing at liquid nitrogen temperature both lead to higher values of the ultimate tensile **strength**. The second trend cannot be seen in the average values of the yield strength. However, the error bars or standard deviations of these data are rather high (see table 7.6). Also the standard deviation values of the uniform elongations are rather high. As the strain measurement itself has been done with great care, it seems that the reproducibility of the specimen geometry and especially of the specimen mounting on the pins should be enhanced. However, due to the small samples size it is difficult to improve these issues.

The UTS values of the investigated Cu and Cu-Al alloys are compared in fig. 7.5. The increase in tensile strength when comparing the HPT processed materials with the as-quenched ones is also plotted (right hand legend). It is in the range of approximately 240% to 325% and increasing with increasing alloy content.

The uniform elongation as a measure for the **ductility** is plotted against the stacking fault energy in fig. 7.6a. As already mentioned, the error bars are rather large, but from the average values the following conclusions can be arrived: Performing HPT at liquid nitrogen temperature leads to somewhat higher values of the uniform elongation. The difference is small and in the range of the error bars in case of the alloys but considerable in case of pure Cu. Cu-15Al processed by HPT at RT and at 77K has the lowest uniform elongation, the highest value in case of HPT at room temperature is obtained for Cu-5Al.

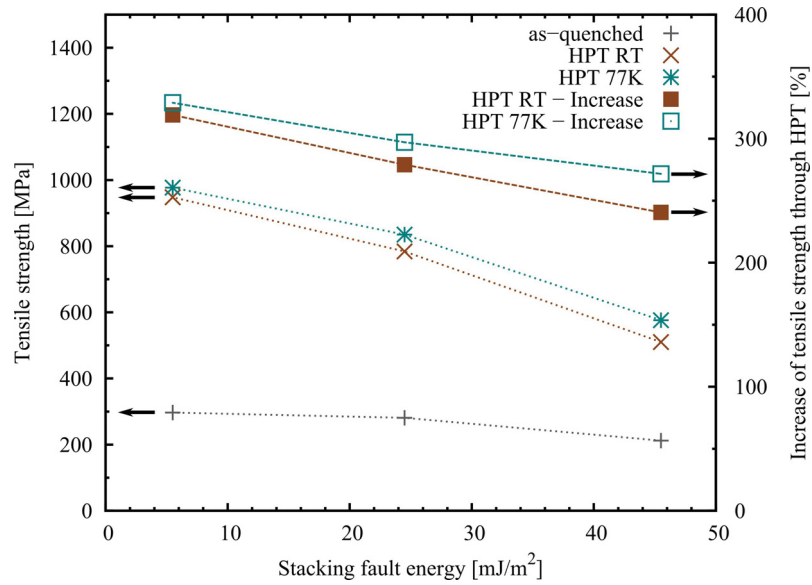
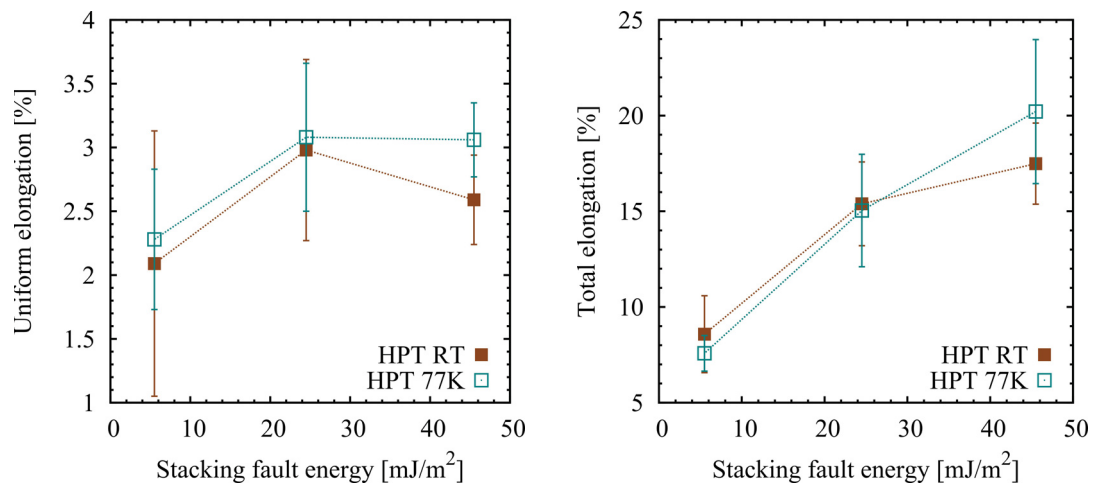


Figure 7.5: Cu and Cu-Al alloys: Ultimate tensile strength vs. stacking fault energy as well as increase of strength by HPT processing. (Error bars smaller than the symbol size. Lines are guides for the eye.)

However, the total elongation as given in fig. 7.6b has a different trend and is clearly decreasing with increasing alloy content or decreasing stacking fault energy.



(a) Uniform elongation as a function of the SFE.

(b) Total elongation as a function of the SFE.

Figure 7.6: Ductility of the investigated materials as a function of the stacking fault energy. (Lines are guides for the eye.)

7.4 Discussion

7.4.1 Strength

When comparing the measured values of tensile strength with available literature on Cu and Cu-Al alloys processed by HPT at room temperature, a very good agreement is obtained as depicted in fig. 7.7.

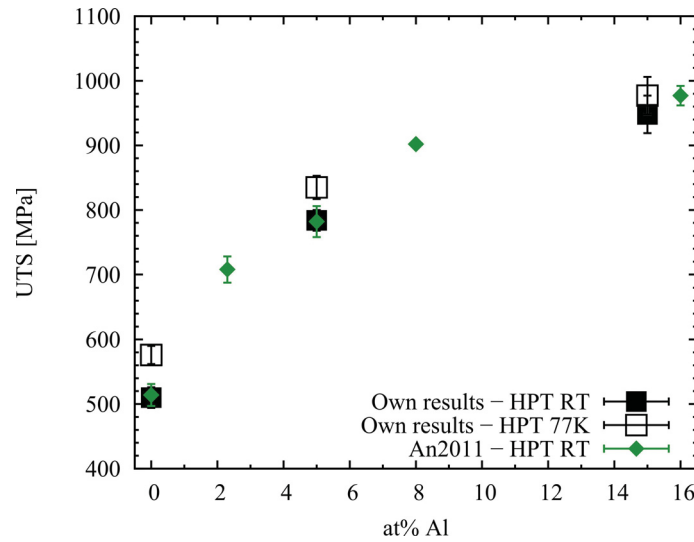


Figure 7.7: Cu and Cu-Al alloys: Comparison of ultimate tensile strength (UTS) with literature data [19] on HPT processed materials (6 GPa pressure, 5 rotations). Due to different values of SFE given in the literature, the alloy content was taken for comparison.

To examine the correlation between the strength and the specific microstructure obtained by SPD, fig. 7.8 shows a Hall-Petch plot for literature as well as own data. It seems that all the available data, irrespective of processing technique and Al content, fall within some scatter on one line thereby suggesting a simple Hall-Petch correlation between the grain size and the yield strength. This conclusion is for example drawn by Zhang et al. [15], and the Hall-Petch coefficient for the various Cu-Al alloys calculated in this paper is the same as for pure Cu.

However, measurements on coarse grained Cu-Al show a considerable increase of the Hall-Petch coefficient with increasing alloy content [139–141]. These values of the Hall-Petch coefficient determined for example by Nakanishi and Suzuki [139] on well annealed Cu and Cu-Al alloys with grain sizes between 400 μm and 10 μm would predict a much higher yield strength for the nanostructured materials as actually measured (see blue lines in fig. 7.8). Only in case of pure Cu the predicted values are slightly below the experimental ones. For example, the predicted value for Cu-16Al exhibiting a grain size of 30 nm (as given for HPT processed material by An et al. [19]) is approximately

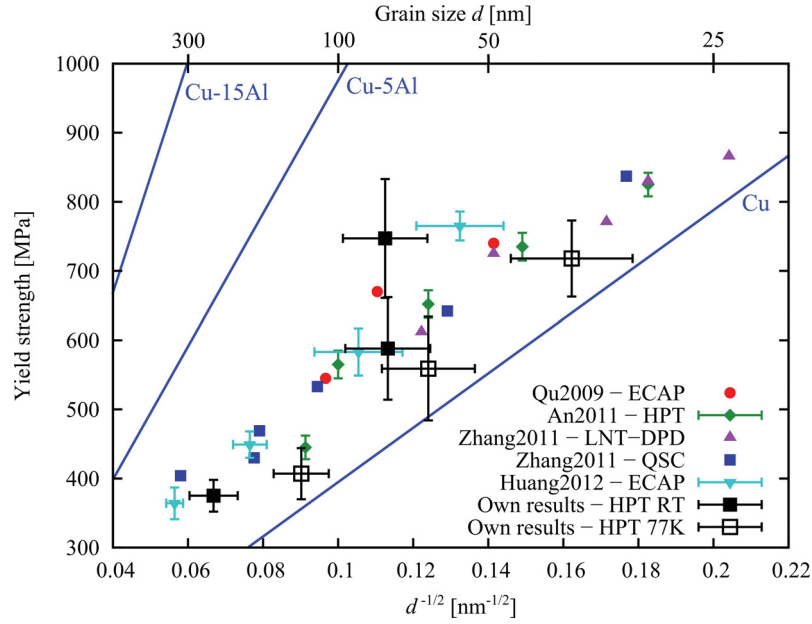


Figure 7.8: Hall-Petch plot of yield strength against inverse square root of grain size. The grain size data from literature are gained by TEM investigations while own grain size values of pure Cu are from SEM and in case of the alloys the domain size obtained by XRD was used. A measurement accuracy of 20% of these values was taken for the error bars. The blue lines are the extrapolations of the results obtained by Nakanishi and Suzuki [139] on annealed coarse grained samples.

2800 MPa which is 3.4 times larger than the measured value of 825 ± 17 MPa. It should be mentioned that a different and less intense dependence of the Hall-Petch coefficient on the concentration is reported by Johnston and Feltner [141]. However, the value of the Hall-Petch coefficient of Cu-15Al reported in this paper is still approximately three times larger than the value for pure Cu, resulting again in predicted values for nanostructured Cu-Al alloys which are far too high.

This serious discrepancy has not been under discussion so far. As a consequence, the origin of the high strength of SPD processed materials should be seen rather in the large dislocation density than in the grain boundaries. Such an analysis was also done for HPT Cu-Zn [12] and for different HPT processed pure metals [11, 155].

According to these statements, the Taylor equation [39] is used to describe the yield strength (σ_y) of HPT processed Cu and Cu-Al alloys:

$$\sigma_y = \sigma_0 + \alpha M G b \sqrt{\rho} \quad (7.1)$$

where σ_0 is a friction stress, α is a parameter which represents the arrangement of dislocations and thereby also shows how efficient the dislocations are in increasing the strength, M is the Taylor factor ($M = 3.06$ for polycrystalline material [27, p. 250]), G is

the shear modulus (Cu: 48 GPa, Cu-5Al: 47.5 GPa, Cu-15Al: 46 GPa; taking the Hashin-Shtrikman averaging scheme [156] and the elastic constants given by Cain and Thomas [157]), b is the absolute value of the Burgers vector (Cu: 0.2556 nm, Cu-5Al: 0.2565 nm, Cu-15Al: 0.2584 nm [157]), and ρ is the measured dislocation density as given in table 7.5.

The friction stress, σ_0 , was chosen as follows: in case of pure Cu it is 20 MPa [155] and in case of the alloys it was increased by the same amount as the tensile strength of the initial (as-quenched) materials increases with alloying. Thereby we get 27 MPa for Cu-5Al and 29 MPa for Cu-15Al.

The values of the dislocation arrangement parameter α obtained by this calculation are given in table 7.7.

Table 7.7: Parameter α in the Taylor equation describing the arrangement of dislocations. The error ranges are obtained by assuming a 20% accuracy of the XRD results which is a rather conservative estimation.

Material	parameter α
Cu, HPT RT	0.14 ± 0.02
Cu-5Al, HPT RT	0.12 ± 0.02
Cu-5Al, HPT 77K	0.10 ± 0.02
Cu-15Al, HPT RT	0.14 ± 0.02
Cu-15Al, HPT 77K	0.10 ± 0.01

In his original paper [39], Taylor suggested that the value of α is between 0.1 and 0.3. A small value of α means a large screening effect of the strain fields of the dislocations. Detailed investigations [158] showed that a structure consisting of a large amount of polarised dipolar walls [74] leads to limited screening effects and thereby to a relatively large value of α , while thin polarized tilt walls [74] evolving during stage IV deformation lead to a small value of α .

Our results show fairly low α -values between 0.10 and 0.14. Therefore, we can conclude that the dislocations existing in the heavily deformed HPT materials are in a low-stress arrangement where their strain fields in large extent cancel each other. This is for example the case when they are arranged in polarised tilt walls, or a kind of low-angle grain boundary structure. It was also shown for HPT processed Ni that the dislocations are not randomly distributed but mainly concentrate into boundaries [5].

The dislocation structure in HPT materials is strongly influenced by the unloading process, meaning the release of the hydrostatic pressure after the HPT deformation. Investigations on this effect [82, 83] show that a strong rearrangement of dislocations occurs during unloading of the pressure. Thus, the low-stress arrangement of the dislocations is not fully developed during the HPT deformation but to a significant part evolves afterwards. During release of the pressure, the dislocation density also decreases [82], however, the remaining dislocation density is still extraordinarily high.

Performing HPT at liquid nitrogen temperature results in even smaller values of α . Although the difference is not too large, this result shows the significance of the unloading process. During deformation at liquid nitrogen temperature the dislocations are less mobile [159, p. 131]. This would constrain the formation of ordered dislocation structures and result in a rather large value of α . However, not only the release of the pressure after the deformation but also the heating up to room temperature contributes to the driving force for a rearrangement of the dislocations, which is therefore increased after low temperature processing. Hence, it is assumed that an even stronger rearrangement of the dislocations occurs after HPT at 77K which results in the small value of the α -parameter.

This analysis shows that the high strength in HPT processed Cu-Al alloys can be explained more reasonably in terms of the high dislocation density and the Taylor equation than when assuming a Hall-Petch-like behaviour.

Of course, the extremely high dislocation density present in SPD processed materials cannot be achieved without the nanoscale grain structure. The boundaries restrict the glide distance of the dislocations and thereby also reduce the chance of mutual annihilation. And as already mentioned, the small value of the dislocation arrangement parameter means that a large amount of dislocations is arranged in a strongly ordered way which could also be called a low-angle grain boundary.

7.4.2 Ductility

Literature and own values of the uniform elongation of SPD processed Cu and Cu-Al alloys are compared in fig. 7.9. Again, we get a very good agreement with the work of An et al. [19].

Before discussing in detail, it should be noted that the differences and tendencies become smaller when subtracting the elastic part of the stress-strain curve from the uniform elongation, as seen in fig. 7.9b. The uniform elongation values given in the references [15–19] include the elastic part, therefore both possibilities of presenting the data are shown in the figure.

It can be seen from the figure that there is no unambiguous correlation between the uniform elongation and the Al content or the stacking fault energy, the second being monotonously decreasing with increasing alloy content. Also a correlation with grain size cannot be found as already stated in the introduction.

However, there are tendencies within the individual measurements to higher uniform elongations with increasing alloy content or decreasing stack fault energy, especially when including the elastic elongation in the measure for uniform tensile strain. Obvious exceptions are the HPT processed samples with the highest Al content. The increases of the uniform elongation values are not too big, but nevertheless very interesting because they co-occur with an increase of strength. This has been widely discussed in the

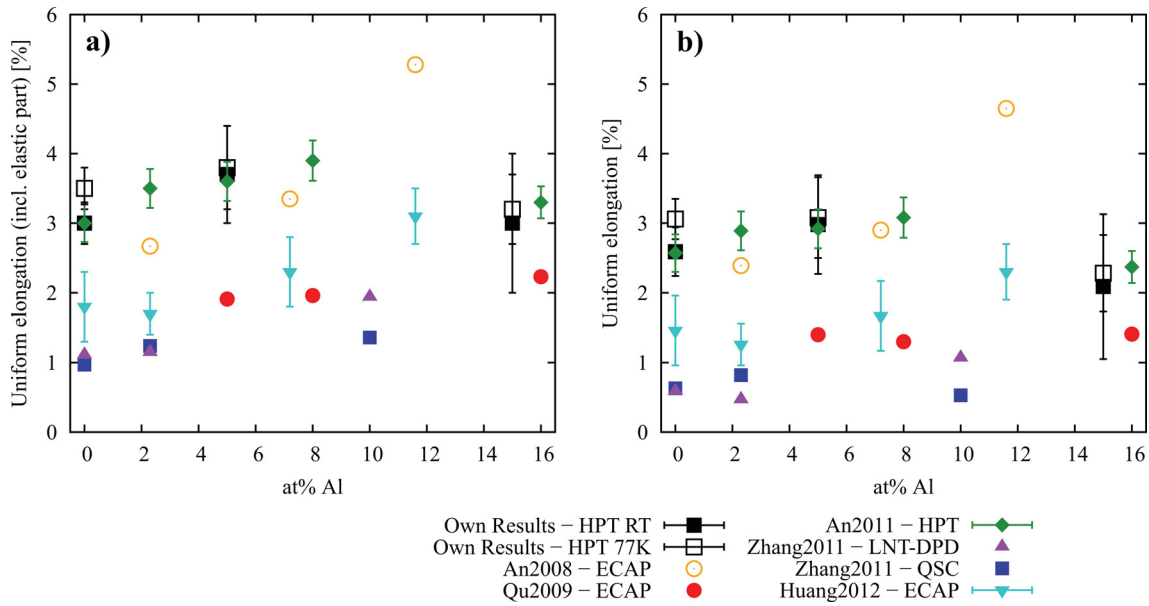


Figure 7.9: Cu and Cu-Al alloys: Comparison of uniform elongation with available literature data [15–19]. (a) Uniform elongation data as given in the literature, including the elastic part of the stress-strain curve. (b) Uniform elongation data without the elastic part of the tensile curve. Due to different values of SFE given in the literature, the alloy content was taken for comparison.

literature (e.g. [17–19, 21]) as the positive effect of decreased SFE resulting in an increased amount of twin boundaries. SPD processed materials with lower SFE are reported to exhibit an increased work hardening rate but the origin of this is not really clear. It is associated with the suppression of dynamic recovery during tensile straining of the SPD processed materials [17] due to an increased splitting distance of partial dislocations in low SFE materials [21]. Other authors associate it with the existence of the numerous twins and stacking faults themselves [19]. Another explanation is the decrease of the critical stress to emit partials from grain boundaries by lowering the SFE [18].

However, when comparing all the uniform elongation values depicted in fig. 7.9a the largest influence seems to come from the processing technique. The samples deformed by compression (LNT-DPD & QSC) show the lowest values of the uniform elongation (1-2%), then come ECAP processed samples (1.8-3%, except of the work of An et al. [16] where larger values are reported), and finally HPT processed samples (3-4%).

Thus, one assumption would be that HPT produces a higher fraction of twin boundaries than ECAP or compression. But this cannot be verified because first of all the twin probability of Cu-5Al processed by HPT at 77K is approximately twice that of the same material processed at RT (2.1% and 1.2%, respectively, see table 7.4) but their uniform elongation values are rather similar. Secondly, the results of Zhang et al. [15] show very similar uniform elongation values for pure Cu processed by LNT-DPD and QSC but many

twins in case of LNT-DPD and no twinning in case of RT-QSC. Therefore, other parameters seem to have far more influence on the ductility than the increase of twin density.

One difference of the individual SPD techniques which may influence the ductility is the texture. There are some publications investigating the effect of texture on the ductility of ECAP processed materials by cutting tensile samples along different directions of the ECAP billets. But these studies show no clear trend. Frint et al. [160] investigated an Al alloy and observed a larger ductility when testing specimens cut parallel to the extrusion direction while the stress-strain curves of rather pure Al plotted in the work of Horita et al. [161] show an opposite trend. A further study of iron [162] showed no dependence of the total elongation on the test direction.

In case of HPT similar investigations are presented in a paper of Rathmayr et al. [163] who performed tensile tests on HPT processed nickel with the tensile axis being parallel to different directions of the HPT disc. While the ultimate tensile strength is markedly influenced by the texture and the reduction in area is influenced by the grain aspect ratio, the uniform elongation is not affected by any of these quantities.

From these investigations it is rather unlikely that texture is responsible for the different values of the uniform elongation of Cu and Cu-Al alloys achieved by different SPD techniques.

A further main difference between the SPD methods compared here is that ECAP as well as LNT-DPD are stepwise processes while HPT is a continuous deformation process which in addition introduces much higher strains and generally uses a higher hydrostatic pressure. The samples processed by ECAP have experienced an equivalent strain between 1 and 8 (see table 7.1) and the pressure used for the ECAP technique is usually in the range of 1 GPa. In case of HPT both values are clearly enhanced, the equivalent strain at the position of the gauge length of the tensile samples is above 50 and the used pressure is 6 GPa.

The increased hydrostatic pressure during SPD processing increases the vacancy migration enthalpy and thereby prevents annihilation of edge dislocations [62]. Thus, a higher amount of dislocations is stored in the material at a higher applied pressure. Although edge dislocations can annihilate via climb during release of the hydrostatic pressure leading to a reduction of dislocation density and vacancy concentration [82], the remaining dislocation density is still higher compared to SPD processing with lower hydrostatic pressure. This was shown by Schafler et al. [3] who measured the dislocation density in HPT processed copper as a function of the applied pressure. During the release of pressure, the dislocations not only annihilate but also change to a low-stress arrangement, i.e. form ordered dislocation structures [82]. It has also been shown that the low-stress arrangement is more pronounced when applying a higher hydrostatic pressure [82, 146].

We can thus expect a difference in the amount and arrangement of dislocations between a process which releases the hydrostatic pressure regularly between the deforma-

tion steps (ECAP), and a process which only releases the hydrostatic pressure after the entire deformation process (HPT). The effect of the extent of applied plastic strain during SPD processing is qualitatively similar to the described effect of pressure. A larger strain increases the dislocation density [3], and the low-stress arrangement of the dislocations is also more pronounced after a higher degree of deformation [82].

From this we can conclude that a low-stress arrangement of dislocations after SPD processing is beneficial for the uniform elongation. Thus, the higher uniform elongation of HPT processed materials compared to ECAP processed ones can be ascribed to the higher pressure and strain used by HPT. These quantities not only lead to a higher density of dislocations but also to a low-energy arrangement of the dislocations after release of the hydrostatic pressure and less internal stresses. The stepless deformation process of the HPT technique may also have an additional beneficial influence.

The low values of the dislocation arrangement parameter α of the order of 0.1 (see table 7.7) obtained by analysing the yield strength of the HPT processed Cu-Al alloys with the Taylor equation support our assumption.

A lower stacking fault energy is expected to decrease the ability of dislocation rearrangement during or after SPD processing due to the larger splitting distance of partials and the thereby reduced mobility of the dislocations [164]. Therefore, a less pronounced low-stress arrangement can be expected in Cu-Al alloys with higher alloy content. This can be the reason for the low uniform elongation in HPT processed Cu-15Al. However, fig. 7.9 clearly shows that this effect is much smaller than the effect of the processing technique and the hydrostatic pressure and strain used thereby. The measurement uncertainties of the α -parameter as well as of the uniform elongation in this alloy are a handicap for a stricter conclusion. Furthermore, no data on dislocation density or especially dislocation arrangement are available in the literature on SPD processed Cu-Al alloys.

At the end it should be noted that the total elongation does not go in parallel with the uniform elongation. It considerably decreases with increasing alloy content or decreasing SFE. This is also the case in the paper by Qu et al. [17] and partially in An et al. [16] and Huang et al. [18]. A decreased workability with increasing alloy content as reported for ECAP and LNT-DPD processed samples [15, 17] supports this finding. It means that as soon as necking starts during tensile testing (which means that the deformation becomes localised) a higher alloy content leads to an increased brittleness of SPD processed Cu-Al alloys.

A comparison of the total elongation values obtained by the different SPD techniques is not possible in a reliable way because of differences in the sample geometry and the direct influence of the gauge length on the measured value of the total elongation [44].

7.5 Conclusions

Higher alloy content as well as lower deformation temperature lead to higher tensile strength of HPT processed Cu-Al alloys. A detailed analysis of own and literature values shows that the dislocation density as part of the Taylor equation is more suitable to explain and predict the yield strength of these materials than the grain size as part of the Hall-Petch equation. As the dislocation density in HPT processed Cu-Al alloys is particularly high, the resulting yield strength is also substantially higher than in case of undeformed or conventionally deformed materials. This analysis furthermore revealed that the dislocations are arranged in a way which results in very effective screening of their strain fields.

This low-stress arrangement of dislocations seems to have a beneficial influence on the ductility expressed by the uniform elongation. This is reflected in higher uniform elongation values of materials processed by SPD techniques which achieve higher strains and use higher pressures during processing – two quantities which strongly affect the dislocation arrangement. The rearrangement of the dislocations into a low-stress arrangement thereby occurs mainly during release of the hydrostatic pressure. Thus, it is also relevant if the SPD technique is a continuous deformation like HPT or if it has an iterative character like ECAP.

The influences of stacking fault energy and of deformation temperature on the uniform elongation are considerably smaller than the influence of the specific SPD technique in terms of the obtained dislocation arrangement. This issue has so far attained too little attention. A proper low-energy dislocation arrangement is thus an important condition in establishing nanostructured materials with high strength and good ductility.

8 Fatigue strength and fatigue crack growth rates in HPT processed nanostructured Cu

Published in: Journal of Alloys and Compounds 509S (2011) S323-S327

Authors: J. Horky, G. Khatibi, B. Weiss, M.J. Zehetbauer

Original title: Role of structural parameters of ultra-fine grained Cu for its fatigue and crack growth behaviour

8.1 Introduction

Using High-Pressure Torsion (HPT), disc-shaped specimens are deformed by shear under high hydrostatic pressure [2] and large degrees of deformation can be achieved leading to bulk ultra-fine grained or nanostructured materials [3, 165].

Literature on the fatigue crack propagation behaviour of ultra-fine grained materials provided by Equal Channel Angular Pressing (ECAP) [114] and Accumulative Roll Bonding (ARB) [166] reports enhanced crack growth rates when compared to coarse grained (CG) materials due to a straight crack path and less roughness-induced crack closure effects [113].

The aim of the work presented here was to investigate the fatigue crack growth behaviour of HPT processed Cu in the threshold range and microstructural evolution during fatigue loading.

8.2 Experimental

8.2.1 Materials

Disc-shaped specimens (diameter 10 mm, height 0.8 mm) of annealed high purity (99.99%) and commercial purity (99.9%) Cu were deformed by HPT by two rotations leading to a shear strain of 42 at a radius of 2 mm [80]. The resulting microstructure and grain size depends on the purity, the same HPT deformation leads to a smaller grain size in case of the commercial purity Cu (150-200 nm compared to 300 nm). Furthermore, a bimodally structured high purity HPT Cu was investigated. A slight annealing heat treatment (150°C for 3 minutes in an oil bath) leads to a microstructure consisting of grains with sizes of 1 to 5 microns (~ 40% of the volume fraction) embedded in a still ultra-fine grained (UFG) matrix.¹

¹The temperature of the heat treatment was chosen on basis of the tensile tests and SEM pictures shown in appendix A.

8.2.2 Tensile Tests

Tensile tests were conducted on miniaturised samples with a parallel gauge length of 2.5 mm and a cross-section of $0.7 \times 0.7 \text{ mm}^2$ at a strain rate of $5 \times 10^{-4} \text{ s}^{-1}$ (fig. 8.1).

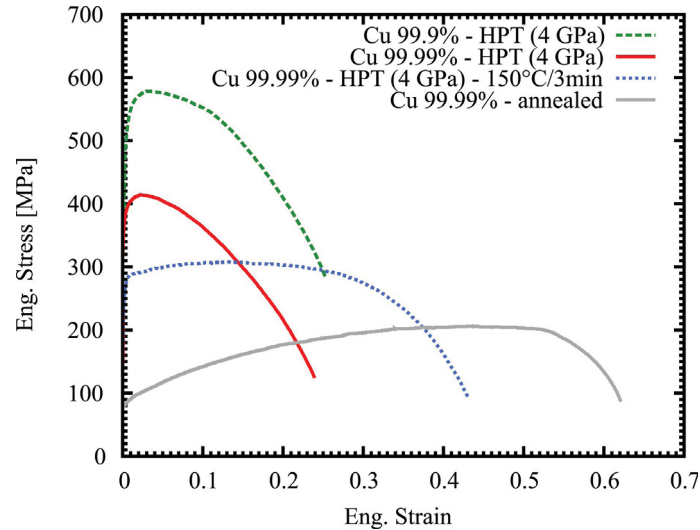


Figure 8.1: Engineering stress-strain curves of the investigated materials.

It can be seen that HPT deformation leads to a strong increase in the ultimate tensile strength (UTS) of the material. Furthermore, the resulting strength depends very much on the grain size, meaning that the finer grain size of the commercial purity HPT Cu leads to a higher strength. The tensile tests also show a decreased ductility after HPT deformation indicated by a lower uniform tensile elongation. Some ductility of the high purity HPT Cu can be regained through the heat treatment, although at the cost of strength. The bimodally structured HPT Cu shows an increase in uniform tensile elongation by 11 percentage points when compared to the ultra-fine grained HPT Cu but a decrease of tensile strength by approximately 100 MPa. The grain sizes and mechanical properties of the investigated materials are summarised in table 8.1.

Table 8.1: Grain sizes and mechanical properties of the investigated materials.

Material	Grain size	Tensile strength [MPa]	Uniform tensile elongation	Fatigue strength (10^9 cycles) [MPa]
HPT Cu 99.9%	150-200 nm	580	0.03	120
HPT Cu 99.99%	300 nm	410	0.02	65
HPT Cu 99.99% - 150°C / 3min	300 nm / 1-5 μm	310	0.14	65
CG Cu annealed	40 μm	200	0.44	80

8.2.3 Ultrasonic resonance fatigue testing system

To investigate the fatigue crack growth behaviour of the small-sized HPT specimens, a set-up previously used for measuring thin foils was adopted [167]. Disc-shaped HPT specimens with a diameter of 10 mm were polished down to a thickness of 200 μm and an elliptical through notch (1.5 $\mu\text{m} \times 0.5 \mu\text{m}$) was introduced in the centre of the specimen. The specimens were electrolytically polished and glued onto a holder over a slot to ensure free standing of the measurement area, see fig. 8.2. The holder as part of an ultrasonic resonance fatigue testing system is subjected to longitudinal push-pull vibrations with zero mean strain (i.e. $R = -1$) at a frequency of 20 kHz. The high frequency used makes it possible to investigate fatigue crack growth rates down to 10^{-12} m/cycle. The crack length was measured using a travelling light microscope with a resolution of approximately 2 μm . Additionally, compressed air was applied for cooling. During each measurement the strain on the holder was monitored using a strain gauge. The strain of the sample was determined by calibration with strain gauges on a notchless sample as well as on the holder. This shows an increase of strain by a factor of 1.64 in consequence of the geometry. The stress amplitude was then calculated from the strain amplitude via Hook's law (Young's modulus for Cu: 120 GPa).

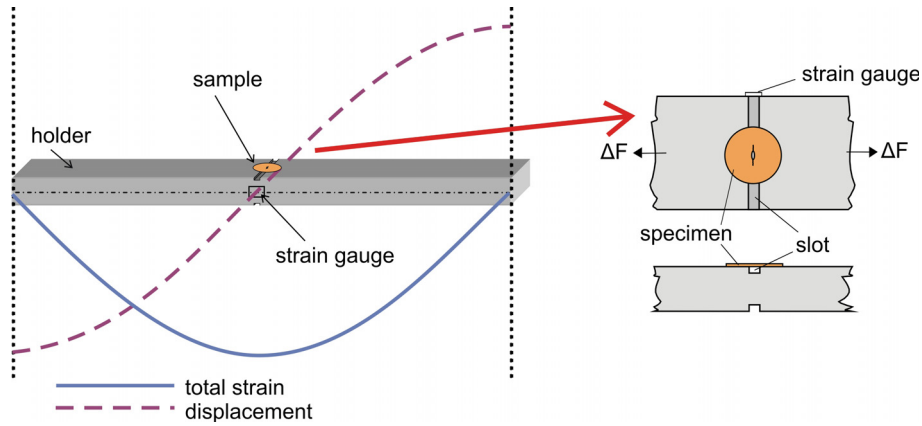


Figure 8.2: Experimental set-up for fatigue crack growth measurement of HPT specimens (schematic).

During cyclic loading the crack emerged on both sides of the notch and crack growth rates were determined in a range of the total crack length $2a$ (including the notch) between 3 and 5 mm. Within the latter limit the microstructure of the HPT specimen can be considered as homogeneous [80]. Fatigue crack growth rates in the threshold regime were determined by the load shedding technique and in addition, constant amplitude tests were conducted. The stress intensity factor range ΔK was calculated via eq. 8.1 where $\Delta\sigma/2$ is the stress amplitude, a is half of the total crack length and $f(a)$ is a geometrical factor taken from [168].

$$\Delta K = \Delta\sigma/2 \sqrt{\pi a} f(a) \quad (8.1)$$

Fatigue life time curves in the high cycle fatigue (HCF) regime were determined by using a similar set-up and flat dumbbell-shaped specimens as described in [23].

8.3 Results and discussion

8.3.1 Fatigue life time curves

When comparing the HCF curves (fig. 8.3), commercial purity HPT Cu shows the best fatigue performance which is not only due to the smaller grain size and the higher tensile strength but also due to a better microstructural stability. Grain coarsening was found to decrease the fatigue life time of high purity HPT Cu at high number of loading cycles [23]. The high purity bimodally structured HPT Cu shows decreased HCF properties in the range of 10^6 to 10^8 cycles to failure when compared to its not thermally treated counterpart which can be explained by the initially lower tensile strength of the material. At number of cycles to failure higher than 10^8 deformation-induced grain coarsening determines the life time and leads to an overlapping of the fatigue life time curves.

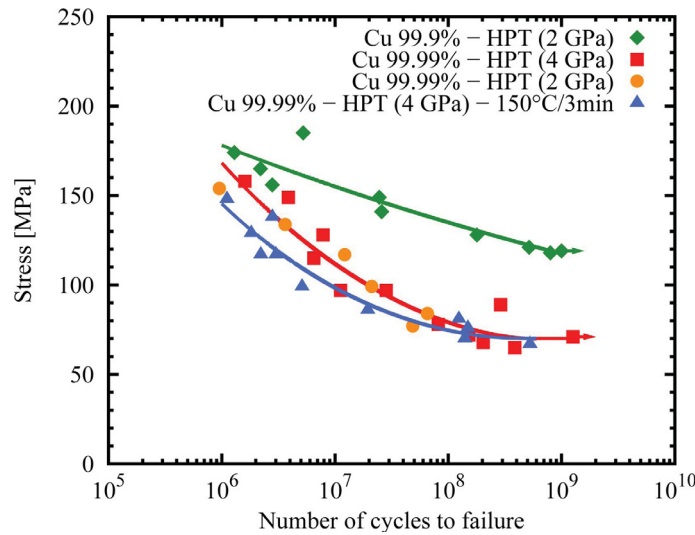


Figure 8.3: High cycle fatigue life time curves for HPT Cu.

8.3.2 Fatigue crack growth threshold

The results of the fatigue crack growth rate measurements are plotted in fig. 8.4 and 8.5, as a function of stress intensity factor range and stress amplitude, respectively.

It can be seen from both figures that all different types of HPT Cu show a lower fatigue crack growth threshold than CG Cu. The threshold stress intensity factor range for HPT Cu is around $3 \text{ MPa}\sqrt{\text{m}}$, which is close to the effective threshold value $\Delta K_{th, eff}$ measured for bulk CG Cu [167]. CG Cu shows a zig-zag crack path and slip marks that cover the surface in a range of $100 \mu\text{m}$ on both sides of the crack. In contrast, crack

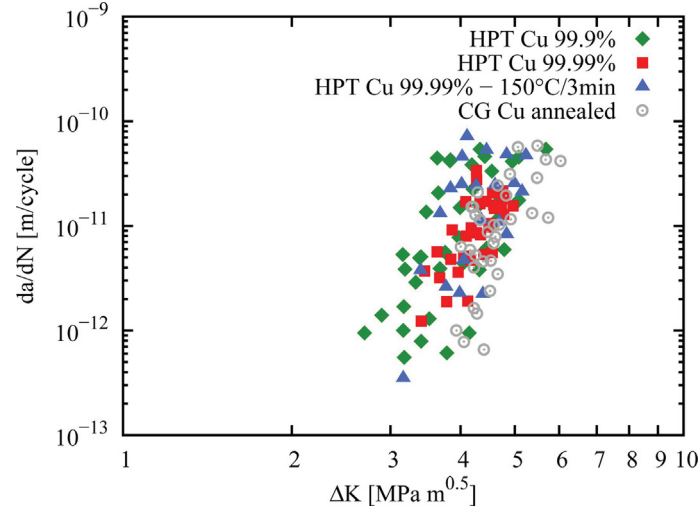


Figure 8.4: Fatigue crack growth rate versus stress intensity factor range ΔK .

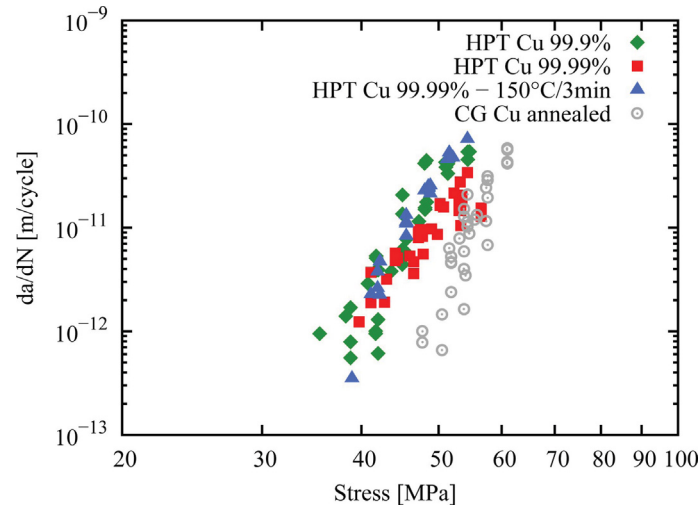


Figure 8.5: Fatigue crack growth rate versus stress amplitude.

paths in HPT Cu are rather straight, see fig. 8.6, leading to higher crack growth rates. This can be related to the reduced effect of roughness-induced crack closure in fine grained materials [48].

A tendency that the commercial purity HPT Cu has the lowest threshold in combination with the straightest crack path can also be seen (fig. 8.6a). Nevertheless, the differences between all tested materials are rather small. Investigations by other researchers (e.g. [114]) on UFG materials show clearly increased crack growth rates in the threshold regime in comparison to CG materials. Contrary to the present study, their works were performed under positive load ratios where crack closure has more influence than at $R = -1$ [169].

When comparing the fatigue life and the crack growth behaviour of the tested HPT materials, the improved fatigue resistance of commercial purity HPT Cu can be related to a reduced sensitivity of the ultra-fine grained and high strength material to crack

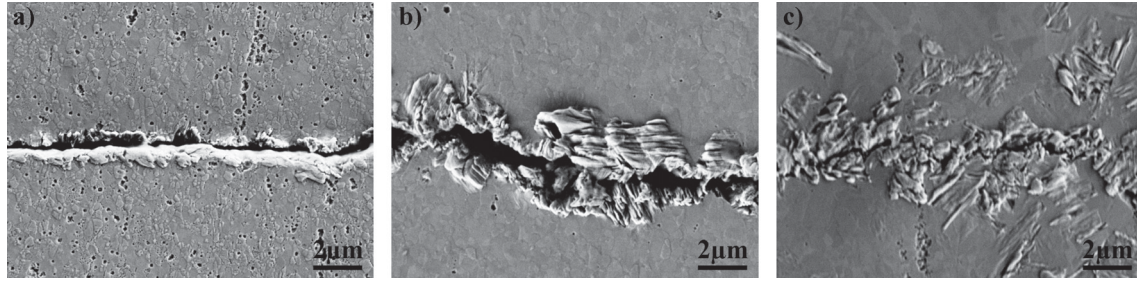


Figure 8.6: Fatigue crack paths in HPT processed Cu at crack growth rates 2×10^{-11} m/cycle: (a) commercial purity, (b) high purity, (c) high purity bimodally structured Cu.

initiation, while the same ultra-fine grained structure leads to a decreased resistance to crack propagation.

The representation of the crack growth rate against the stress amplitude in fig. 8.5 has been chosen because the large scatter in fig. 8.4 raises the question if the concept of ΔK derived from linear elastic fracture mechanics can be applied to this miniaturised specimens with non-standard geometry.

8.3.3 Microstructural evolution in high purity HPT Cu

High purity HPT Cu showed grain coarsening during fatigue loading in the HCF regime. Thus, the microstructure in the vicinity of the crack was investigated at different constant stress amplitudes. Fig. 8.7a shows fatigue slip marks near the crack on the surface of a high purity HPT Cu sample. Their lengths reach up to 20 μm which exceeds the original grain size of 300 nm by about two orders of magnitude. Fig. 8.7b is an electron channelling contrast (ECC) image at the same position after repolishing the surface. The pictures show that there occurs grain coarsening nearby the crack and that surface slip marks form within these coarsened areas. In the remaining UFG area no surface slip marks can be found.

The area of coarsened grains increases with decreasing stress amplitude and accordingly lower crack growth rate. Figs. 8.8a-c compare the microstructure nearby the crack at applied stress amplitudes of 55, 49 and 42 MPa, respectively. At the highest stress amplitude the grains in the vicinity of the crack roughly maintain their original size (fig. 8.8a) while at the lowest stress amplitude they expand up to a size of several micrometer within a radius of approximately 10 μm around the crack tip (fig. 8.8c). The coarsening leads to a behaviour contrary to the behaviour of CG materials where the cyclic plastic zone size decreases with decreasing stress amplitude [48]. It should be pointed out that this grain coarsening near the crack occurs only at crack growth rates considerably beneath 10^{-10} m/cycle.

It is known that the strain energy dissipated per unit surface created during cyclic loading is directly proportional to the stress amplitude and inversely proportional to the

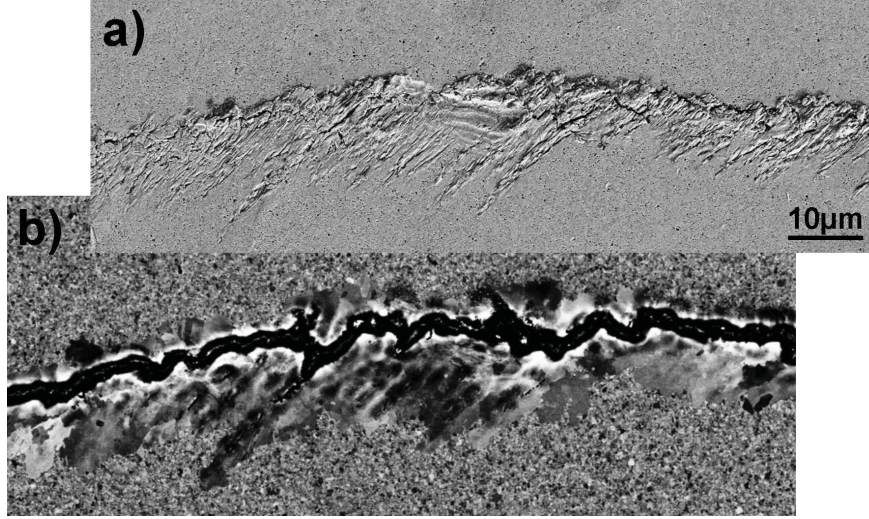


Figure 8.7: (a) Surface slip marks in high purity HPT Cu at a stress amplitude of 42 MPa and a crack growth rate of 5×10^{-12} m/cycle and (b) ECC image of the same sample area.

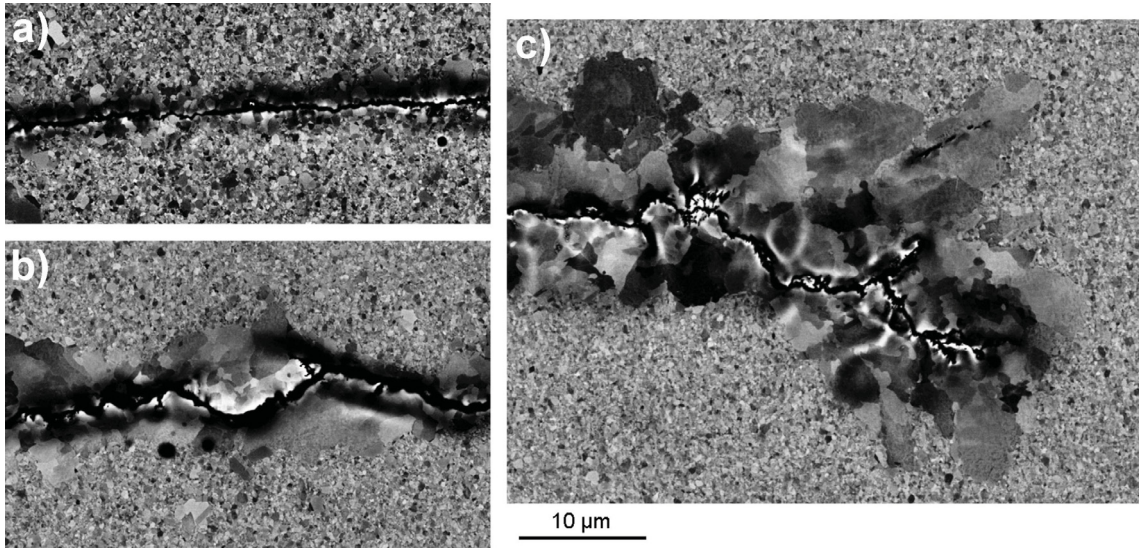


Figure 8.8: Microstructure near the crack in high purity HPT Cu at (a) 55 MPa and 4×10^{-11} m/cycle, (b) 49 MPa and 2×10^{-11} m/cycle (c) 42 MPa and 7×10^{-12} m/cycle.

crack growth rate² [170]. In the threshold regime the crack growth rate decreases faster than the stress amplitude, thus it can be assumed that the required activation energy for dynamic recrystallisation and grain coarsening in the high purity UFG material is provided by an increased dissipated energy during cyclic loading at low stress amplitudes and near-threshold crack growth rates.

²Strain energy dissipated per unit surface created: $U = \frac{Q}{2b} \frac{da}{dN}$ [170]. Q is the hysteresis energy which is as a first approximation proportional to the loading amplitude, b is the thickness of the sample.

Applying constant amplitude loading at various stress amplitudes on high purity HPT Cu with a bimodal microstructure, grain coarsening was not observed (fig. 8.9). Fatigue slip marks can only be found in the initially larger grains, as can be seen in fig. 8.6c. The higher stability and therefore originally fine grain size in this material leads to higher crack growth rates when compared to UFG HPT Cu. This is a hint for a retardation of the fatigue crack propagation through grain coarsening.

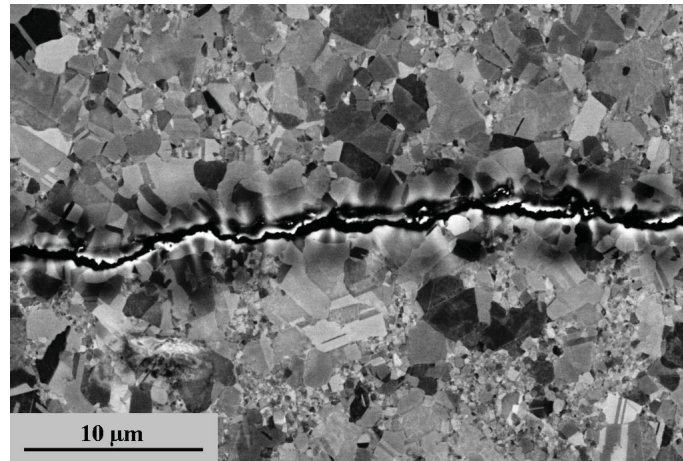


Figure 8.9: Microstructure near the crack in case of the bimodally structured high purity HPT Cu (43 MPa and 3×10^{-11} m/cycle).

8.4 Conclusions

In the present work the high cycle fatigue behaviour and the near-threshold crack growth rates of HPT processed samples were determined. The materials under investigation were commercial and high purity Cu as well as a bimodally structured high purity HPT Cu. The HPT materials exhibit increased HCF life but also increased crack growth rates indicating that the UFG microstructure shows a better resistance against fatigue crack initiation but a lower resistance against crack propagation compared to CG material. In addition to these general findings, the stability of the UFG structure is of utmost importance. It is increased in the case of commercial purity HPT Cu leading to superior HCF life time. The high purity HPT Cu coarsens during cyclic loading and even during crack propagation at very low crack growth rates. This leads in the first case to an earlier crack initiation and therefore decreased HCF life time, and in the second case to a retardation of the crack growth rate. Although the bimodally structured HPT Cu has a higher microstructural stability than the high purity UFG HPT Cu, an improvement of the fatigue performance did not occur.

9 Effect of microstructural stability on fatigue crack growth behaviour of HPT processed nanostructured Cu

Published in: Mechanics of Materials 67 (2013) 38-45

Authors: J. Horky, G. Khatibi, D. Setman, B. Weiss, M.J. Zehetbauer

Original title: Effect of microstructural stability on fatigue crack growth behaviour of nanostructured Cu

9.1 Introduction

The different techniques of Severe Plastic Deformation (SPD) [1, 6], e.g. Equal Channel Angular Pressing (ECAP) [61, 67], High-Pressure Torsion (HPT) [2] or Rolling and Folding [63], are widely used to produce ultra-fine grained (UFG) or nanostructured materials. These materials with grain sizes below some few hundred nanometers generally show enhanced strength and a reasonable ductility [6, 10]. Concerning cyclic deformation, an enhancement of fatigue properties is observed, i.e. longer fatigue life times and higher fatigue strengths, in stress-controlled testing and representation in an S-N “Woehler”-plot [25, 171]. The picture looks different in plastic strain-controlled low cycle fatigue (LCF) tests represented in Coffin-Manson-plots. Here, UFG materials show cyclic softening and shorter fatigue life times than coarse grained materials [107]. Regarding the fatigue crack propagation, higher crack growth rates and lower stress intensity threshold values have been reported for nanostructured materials compared to their coarse grained counterparts (e.g. ECAP Cu [114], electro-deposited Ni [113], ECAP Al alloy [172], ECAP IF steel [117]). Recently, Meirom et al. [173, 174] reported fatigue-induced grain coarsening during crack propagation in nanocrystalline Pt films and related it to the annihilation of (low angle) grain boundaries through dislocation slip near the crack tip.

In a previous investigation of our group [175] it was found that the threshold stress intensity factor range for HPT Cu is lower than that of the coarse grained material. A further result was that crack growth as well as cyclic deformation behaviour in the high cycle fatigue (HCF) regime of high purity HPT Cu is strongly affected by the stability of the material. At crack growth rates beneath 10^{-10} m/cycle the microstructure coarsens in the vicinity of the crack tip. This effect is larger at lower growth rates because of an increased dissipated energy per crack length expansion [170, 175].

The intention of this paper is to obtain a deeper insight in the effect of grain coarsening on fatigue crack growth behaviour of HPT Cu. Therefore, not only high purity but also commercial purity as well as bimodally structured HPT Cu were investigated in detail.

9.2 Material and methods

Coarse grained (CG) Cu of high purity (99.99%) and commercial purity (99.9%) were processed by HPT at room temperature (RT). The disc shaped samples had a diameter of 10 mm, a thickness of 0.8 mm, the applied pressure was 4 GPa and the HPT shear strain was 42 at a radius of 2 mm, corresponding to two rotations [80]. The third investigated material condition was obtained through a slight heat treatment (150°C for 3 min in an oil bath) of the high purity HPT Cu.

For crack propagation measurements, the HPT specimens were mechanically and electrolytically polished down to a thickness of 200 μm and an elliptical through notch was introduced by means of spark erosion in the centre of the disc. The samples were glued on a holder which was part of an ultrasonic resonance fatigue testing system operating under symmetrical push-pull loading (load ratio $R = -1$) at a frequency of 20 kHz. Details can be found elsewhere [175]. The samples were precracked and cooled by compressed air during testing. Control measurements with an infra-red thermometer as well as with a thermocouple showed that in spite of the high frequency used the temperature rise of the samples was below 5°C. Moreover, no significant local temperature rise at the crack tip is expected due to the small stress amplitude applied [176].

Scanning electron microscope (SEM) investigations were carried out on a Zeiss Supra 55 VP equipped with a backscatter detector. Thermal stability measurements were conducted on a differential scanning calorimeter (DSC) Perkin Elmer DSC-7 from RT up to 450°C using a heating rate of 10 K/min. Thereby, annealing of deformation-induced defects results in an exothermic peak where the peak temperature corresponds to the activation enthalpy, while the overall area of the peak is the stored energy corresponding to the defect density [177]. At least two samples were measured to obtain an average value.

9.3 Experimental results

Grain sizes, tensile strengths, uniform elongations, fatigue strengths as well as results from DSC measurements are listed in table 9.1.

HPT treatment leads to a strong grain refinement and therefore an increase of tensile strength. Both effects are more pronounced in case of the commercial purity Cu. A slight annealing heat treatment of the high purity HPT Cu leads to the formation of a bimodal grain size distribution with about 40% of the volume fraction consisting of grains with sizes of some microns embedded in a still ultra-fine grained matrix (fig. 9.1). This causes a decrease of tensile strength but also a considerable increase of ductility [175].

Table 9.1: Grain sizes, DSC results and mechanical properties [175] of the investigated materials.

Material	Grain size	DSC peak temp. [°C]	Stored energy [J/g]	Tensile strength [MPa]	Uniform tensile elongation	Fatigue strength (10 ⁹ cycles) [MPa]
HPT Cu 99.9% (commercial purity)	150-200 nm	223.2 ± 0.5	1.0 ± 0.1	580	0.03	120
HPT Cu 99.99% (high purity)	300 nm	155 ± 4	1.5 ± 0.3	410	0.02	65
HPT Cu 99.99% - 150°C / 3min	300 nm / 1-5 µm	155 ± 3	0.3 ± 0.1	310	0.14	65
CG Cu annealed	40 µm	–	< 0.05	200	0.44	80

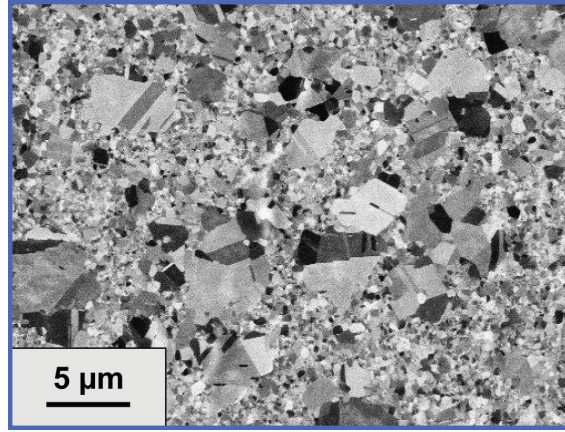


Figure 9.1: Bimodal microstructure of high purity HPT Cu obtained through a slight annealing heat treatment at 150°C for 3 min.

9.3.1 Microstructural stability

DSC measurements revealed that the thermal stability of the commercial purity HPT Cu is markedly higher than that of the high purity material, annealing of defects happens at about 223°C instead of 155°C (fig. 9.2). DSC measurement of the bimodally structured HPT Cu shows a marked drop of the stored energy through the post-HPT heat treatment but the temperature at which the remaining defects anneal stays the same.

During cyclic loading in the HCF regime the accumulated strain leads to grain coarsening in the high purity HPT Cu and hence to a marked decrease of fatigue strength [23]. Especially with increasing number of loading cycles, the stability of the microstructure becomes highly important [23, 175]. The fatigue strength of the bimodally structured HPT Cu is the same as for the high purity HPT Cu because in both materials grain coarsening is the life time determining factor.

9.3.2 Fatigue crack growth at constant stress amplitude

Fatigue crack growth measurements were conducted under two constant levels of stress amplitude (42 MPa and 55 MPa) which were chosen based on our previous investigation [175]. At the lower stress amplitude grain coarsening was detected in high purity HPT Cu, while at the higher value coarsening was not observed.

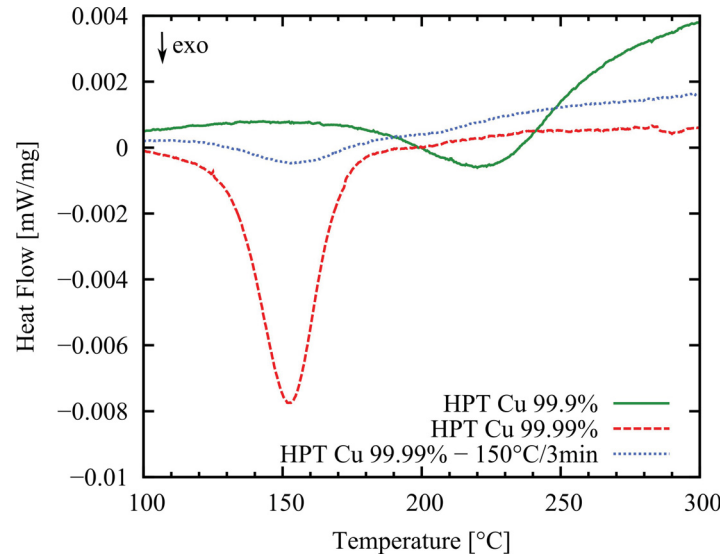


Figure 9.2: DSC scans of the materials as indicated. Each is showing one exothermic peak corresponding to annealing of deformation-induced defects.

Fig. 9.3 shows the change of crack length with increasing number of loading cycles for HPT Cu at an applied cyclic stress amplitude ($\Delta\sigma/2$) of 42 MPa. For each material one representative curve is shown, the measurement accuracy is in the order of the symbol size. The error bars given at the end of the curves represent the average and standard deviation of several measured samples for each material. Hence, it is obvious that the accuracy of measurement of the individual samples is much higher than the difference between them which seems to be due to the small sample size and hence the challenging specimen preparation.

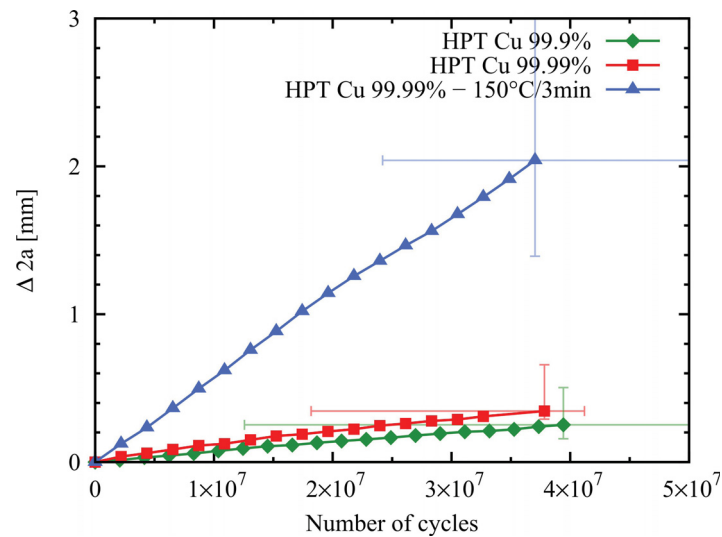


Figure 9.3: Change of total crack length ($\Delta 2a$) against number of loading cycles for HPT Cu at a stress amplitude of 42 MPa.

In fig. 9.3 all tested HPT materials show a linear behaviour, meaning that the crack growth rate does not change with increasing crack length or number of loading cycles. However, due to the small sample size only a short measuring length was available.

Within the error bars both as-HPT processed materials show the same crack growth rate independent of the purity. Only the bimodally structured high purity HPT Cu exhibits clearly faster crack propagation. Extensive grain coarsening in the vicinity of the crack in high and commercial purity samples in the as-HPT condition can be observed (fig. 9.4). While grain coarsening in commercial purity Cu is less pronounced, the heat treated bimodally structured Cu shows no microstructural changes at all (fig. 9.4b).

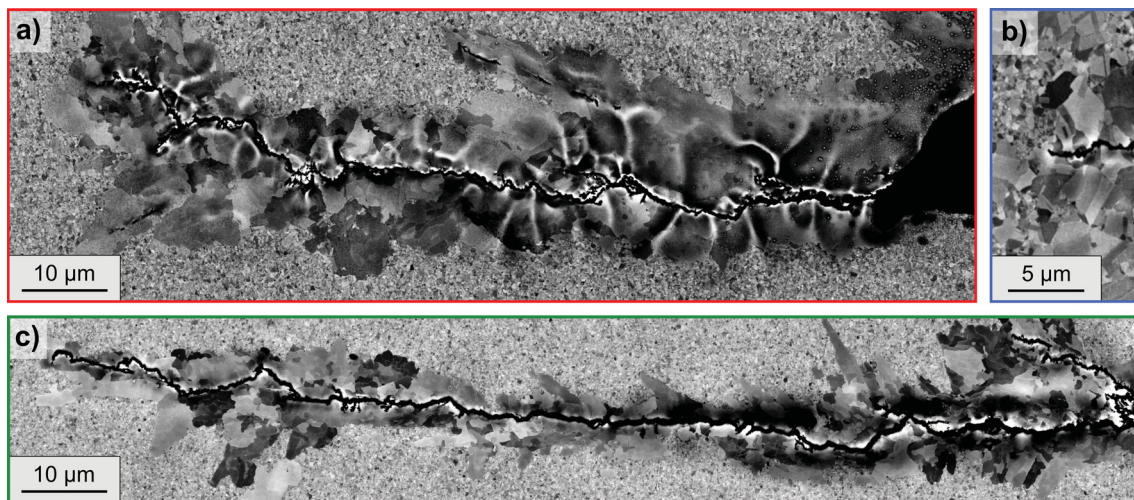


Figure 9.4: Microstructure in the vicinity of the crack at an applied stress amplitude of 42 MPa. (a) High purity HPT Cu, (b) bimodally structured high purity HPT Cu, (c) commercial purity HPT Cu.

Analogous to the previous diagram, fig. 9.5 shows the crack growth behaviour of the tested materials at an applied stress amplitude of 55 MPa. Again, all tested HPT materials show linear behaviour but in contrast to the results for the lower stress amplitude, only minor differences in crack growth rates are observed. It can be seen that CG Cu shows a considerably lower propagation rate at this stress amplitude.

A slight amount of grain growth in the vicinity of the crack in as-HPT materials can be found as shown in fig. 9.6. The grain structure of the bimodally structured HPT Cu is similar to the image shown in fig. 9.4b.

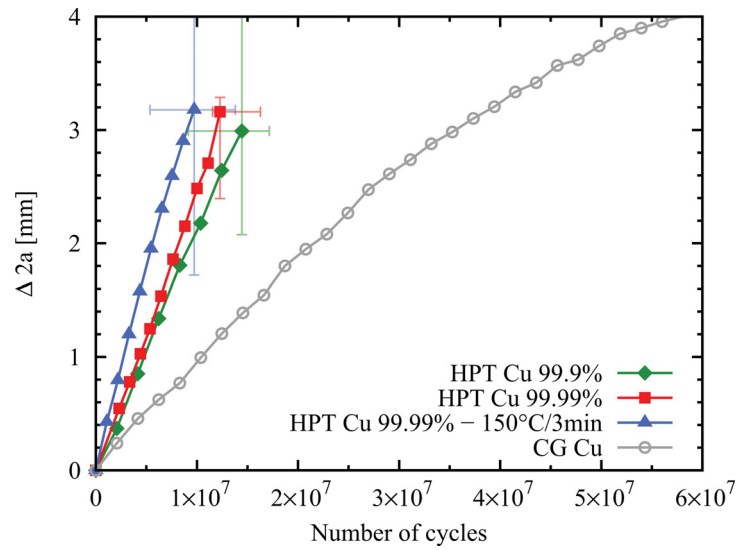


Figure 9.5: Change of total crack length ($\Delta 2a$) against number of loading cycles for HPT and CG Cu at a stress amplitude of 55 MPa.

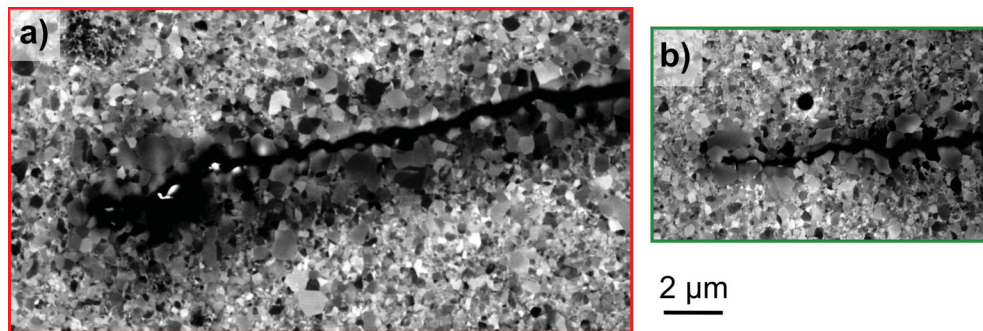


Figure 9.6: Microstructure in the vicinity of the crack at an applied stress amplitude of 55 MPa. (a) High purity HPT Cu, (b) commercial purity HPT Cu. The scale bar is the same for both images.

Fig. 9.7 shows the crack paths in the different HPT materials as well as in CG Cu at a stress amplitude of 55 MPa. The roughness corresponds to the grain size of the material and only in case of bimodally structured HPT Cu and CG Cu a zig-zagged crack path can be observed. For the heat treated bimodal HPT Cu the deviations are in the range of the larger grains of the bimodal size distribution (i.e. a few microns) and for CG Cu they are in the range of tens of microns.

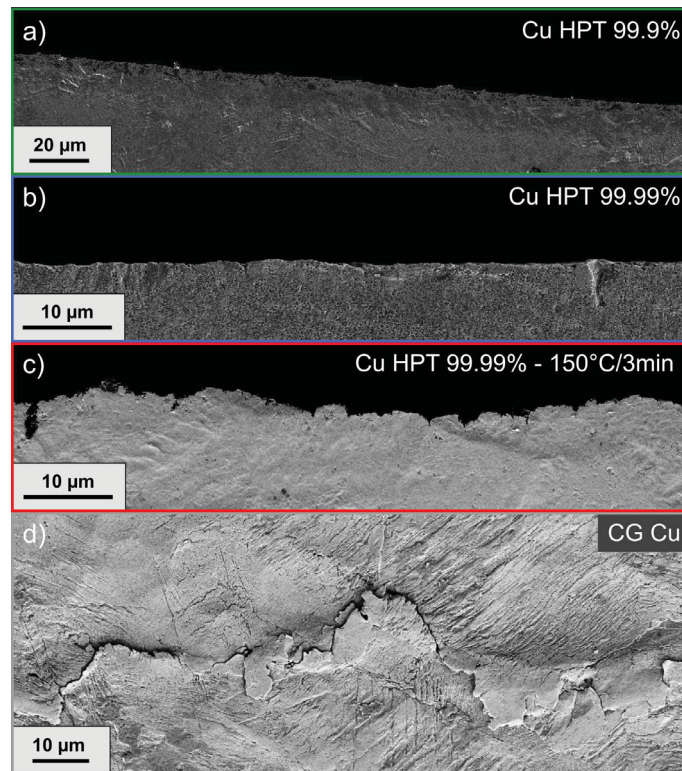


Figure 9.7: Fatigue crack paths in different materials at a stress amplitude of 55 MPa. In case of the HPT materials top view of half of a completely broken sample.

9.3.3 Relation of crack growth and strength in HPT Cu

According to their high strength and low ductility it is not unexpected that nanostructured materials show inferior crack growth behaviour than coarse grained materials. For a better comparison of the three HPT materials tested here the difference in their tensile strength should be taken into account. Fig. 9.8 shows crack propagation rates with applied stress amplitudes corresponding to 13% of the tensile strengths of the materials. At these stress amplitudes none of the tested materials showed grain coarsening.

In this figure commercial purity HPT Cu which has the smallest grain size and largest tensile strength, exhibits the fastest crack propagation while the bimodally structured high purity HPT Cu shows the slowest one. To compare such different materials this

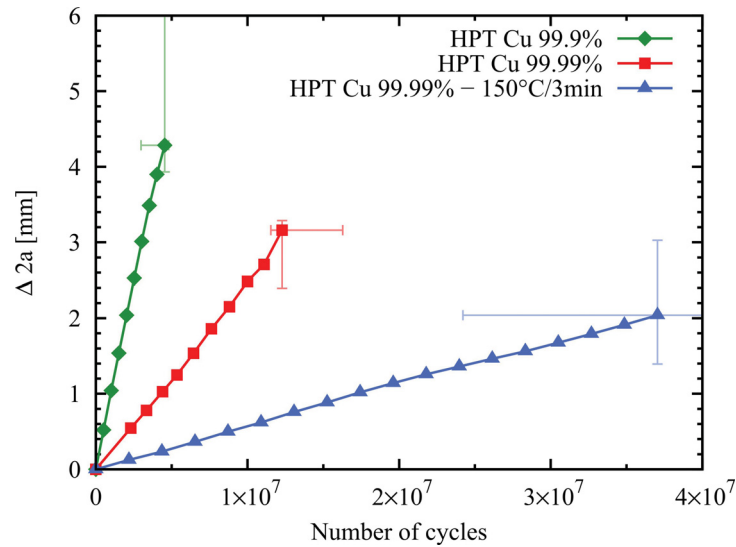


Figure 9.8: Change in total crack length ($\Delta 2a$) against number of loading cycles for different HPT materials, all tested at 13% of their tensile strength (HPT Cu 99.9%: 78 MPa, HPT Cu 99.99%: 55 MPa, HPT Cu 99.99% – 150°C/3min: 42 MPa).

attempt may be useful because it can be expected that higher strength materials are used for applications which have to bear larger loads.

9.3.4 Change of stress amplitude

To obtain a deeper insight into the interdependence of crack growth rate and grain coarsening, the effect of a change of the applied stress amplitude was studied in high purity HPT Cu. Fig. 9.9 shows the effect of an increase of the loading amplitude, while fig. 9.10 presents the effect of a decrease of the applied stress amplitude. The SEM images of the corresponding areas are presented in fig. 9.9a and 9.10a.

On raising the applied stress amplitude, the crack growth rate does not reach the level expected for the new stress amplitude until the crack has grown out of the previously coarsened area. Due to the gradually changing crack growth rate also the size of the coarsened area changes gradually and vice versa. However, after a certain number of loading cycles a distinct crack growth rate is reached for each stress amplitude applied.

On lowering the applied stress amplitude the response of the crack growth rate is also not instantaneous and reaches its final value only after the coarsened area is completely formed. It can be expected that also in this case the change of crack growth rate happens gradually. However, the transition of crack growth rate needs a lower number of cycles.

Similar effects were observed in commercial purity HPT Cu but not in the bimodally structured HPT Cu.

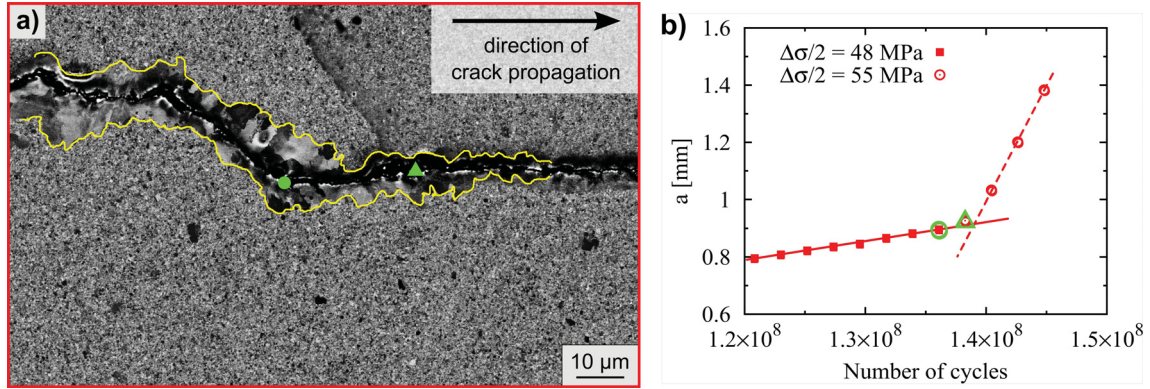


Figure 9.9: Response of the growing fatigue crack in case of raising the applied stress amplitude for high purity HPT Cu. In the SEM-image (a) the corresponding positions of the crack tip for two data points of the diagram crack length vs. number of loading cycles (b) are marked by a circle and a triangle, respectively. Additionally, the spreading of the coarsened area in the vicinity of the crack is drawn by a line.

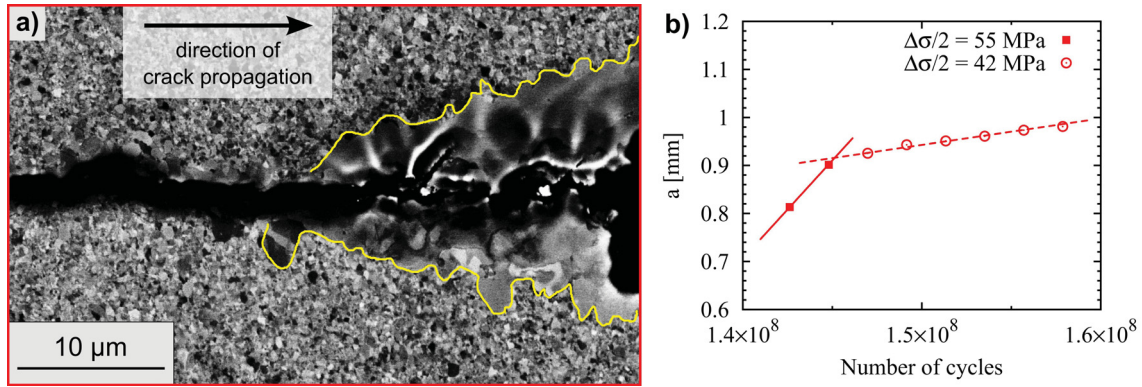


Figure 9.10: Response of the growing fatigue crack in case of lowering the applied stress amplitude for high purity HPT Cu. a) Microstructure; the change of stress amplitude was carried out approximately 4 μm ahead of the first detectable coarsened grains. The spreading of the coarsened area is drawn by a line. b) Crack length vs. number of cycles.

9.4 Discussion

9.4.1 Influence of grain coarsening on crack propagation

The most noticeable feature of fatigue crack growth behaviour in HPT Cu is the occurrence of grain coarsening in the vicinity of the crack. As already reported in our previous publication [175] grain coarsening occurs only at growth rates below 10^{-10} m/cycle and is more pronounced at lower crack growth rates. At a stress amplitude of 42 MPa grain coarsening occurs in the as-HPT processed materials irrespective of the purity (compare fig. 9.4a and c). The only difference is that in case of commercial purity HPT Cu the

size of the coarsened area is only roughly half as large as in case of high purity HPT Cu. At the higher stress amplitude of 55 MPa grain coarsening only happens to a very small extent (fig. 9.6).

The bimodally structured high purity HPT Cu has considerably larger grain size and enhanced ductility in tension than the as-HPT processed materials. From both one may expect decreased crack growth rates due to roughness-induced crack closure and a higher ability to reduce local stresses at the crack tip via deformation. The opposite is observed at a cyclic stress amplitude of 42 MPa giving rise to the conclusion that the occurrence of grain coarsening during cyclic loading leads to a retardation of crack growth. The bimodally structured HPT Cu shows the fastest crack growth rate at 42 MPa with no coarsening. At a higher applied stress amplitude of 55 MPa apparently no coarsening occurs and crack growth rates of HPT materials are all about the same.

The occurrence of grain coarsening can now have two effects: first, it seems reasonable that the dissipated energy during cycling is transmitted into plastic deformation and movement of grain boundaries instead of creation of new surface area and crack advancement. Furthermore, grain coarsening takes place in front of the crack tip (cp. fig. 9.4) leading to a totally different surrounding area for crack growth. In this case crack propagation does not occur in an ultra-fine grained material with high strength and low ductility but in a coarse grained material which is apparently softer and more ductile.

The experiments with raising of the applied stress amplitude (see fig. 9.9) show that crack growth is retarded until the crack grows out of the previously coarsened area. This would suggest that it is rather the existence of the coarsened grains in front of the crack tip which retards crack growth. But on the other hand the existence of coarse grains in the bimodally structured HPT Cu does not lead to lower crack propagation rates.

Literature (e.g. [113]) reports faster crack growth in nanomaterials because of straighter crack paths and therefore less roughness-induced crack closure. Obviously, this is not the case here because at higher stress amplitude where no coarsening takes place, bimodally structured Cu exhibits the most tortuous crack path (fig. 9.7) but its crack growth rate is within the error bar the same as for the other HPT materials tested (fig. 9.5). When comparing with available literature one has to consider two experimental differences, namely the load ratio of $R = -1$ and the particularly low propagation rates. It was shown for example by Silva [169] that roughness-induced crack closure is not a relevant mechanism at $R = -1$ or perhaps the roughness observed in the bimodally structured HPT Cu is too small to cause closure effects at this load ratio.

9.4.2 Comparison of crack growth with cyclic deformation in the HCF regime

Grain coarsening and related cyclic softening behaviour in nano- or ultra-fine grained materials was frequently observed during cyclic deformation in the high cycle fatigue regime

by several groups using different sample geometries and testing frequencies (e.g. [23–25]). It was associated with the low stability of nanostructured materials especially those exhibiting high purity and recently also with the mode of testing, i.e. stress- or strain-controlled cyclic loading [25].

Höppel et al. [24] identified grain coarsening as a thermally activated process which depends also on the plastic strain amplitude. It is a dynamic recrystallisation process, meaning nucleation and growth of grains but it also involves subsequent migration of high-angle grain boundaries. The boundary migration seems to be of particular importance because an exclusive nucleation and growth mechanism would lead to smaller grain sizes due to the large number of nucleation sites in the heavily deformed SPD materials.

Comparing our results of cyclic deformation tests in the HCF regime [23, 175] with the observations during crack propagation where the materials and testing conditions were identical, the most striking difference concerns the effect of purity. With crack propagation, grain coarsening was found in the vicinity of a crack irrespective of the material's purity, but during cyclic deformation, coarsening was only observed in high purity material. In bimodally structured high purity HPT Cu the situation was different as grain coarsening did not occur during crack propagation but during HCF testing (although much less than in the as-HPT state of the same purity).

Cyclic deformation in the HCF regime showed that grain coarsening is mainly time controlled, i.e. it is more intense at higher number of loading cycles and therefore larger accumulated plastic strain. During crack growth a smaller propagation rate and therefore increased dissipated energy per crack length expansion leads to increased grain coarsening. Thus, it seems that in both cases the accumulation of plastic deformation is responsible for grain coarsening.

The processes of dynamic recrystallisation and grain growth responsible for coarsening are both driven by the defect content or rather the stored energy of the material but the annihilation of defects and migration of grain boundaries (grain growth) need some activation energy [77]. As seen from our DSC experiments, the activation enthalpy is directly related to the material's purity while the stored energy in high purity and in commercial purity HPT Cu is about the same but much lower in the heat treated bimodal HPT Cu. Therefore, it seems that grain coarsening in the presence of a fatigue crack depends more on the stored energy of the HPT materials while during cyclic deformation it is more associated with the activation enthalpy for recrystallisation and grain growth phenomena.

A possible explanation for this behaviour is the following: for the occurrence of grain coarsening two conditions have to be fulfilled simultaneously. Namely, (i) the energy stored in the material has to reach a certain critical value and (ii) the activation barrier for the migration of defects has to be overcome. For the first condition the sum of

the stored energy already present in the material plus the energy which is accumulated during cyclic loading is crucial while for the second condition the energy which is put into the material in one cycle is important.

In case of *fatigue crack growth* the energy per cycle is released very locally at the crack tip. Thus, the activation barrier can be overcome also in commercial purity HPT Cu. However, the other parts of the specimen are not cyclically loaded and the stored energy is not markedly raised meaning that in case of the bimodal HPT Cu it stays at a relatively low value. As a result grain coarsening during crack growth is observed in both as-HPT processed materials but not in the bimodally structured one. However, the picture is different in case of *cyclic loading in the HCF regime*. The energy per cycle is released in a much larger part of the specimen so that the activation barrier cannot be overcome in the commercial purity HPT Cu. Thus, no grain coarsening occurs in this material. On the other hand cycling increases the stored energy of the material so that for bimodal HPT Cu the critical value is reached and in combination with the lower activation enthalpy of this high purity material grain coarsening occurs.

Boyce and Padilla [178] proposed a mechanism for crack initiation in nanocrystalline materials. Grain coarsening occurs locally and within the coarser grains traditional persistent slip processes can take place leading to the initiation of a fatigue crack. This seems also applicable to our materials. During cycling in the HCF regime most part of the life time is devoted to crack initiation, which is much easier in larger grains where surface extrusions and intrusions can form. If the material coarsens and larger grains form, crack initiation takes place much earlier and the overall HCF life is markedly reduced. This is exactly what we observed in high purity HPT Cu [23]. Our recent results on the other hand suggest that, if the applied stress is not too high and coarsening occurs also during propagation of the initiated crack, crack growth in nanomaterials can be retarded and the instability of the microstructure which favours crack initiation also is able to decrease crack growth rates.

9.5 Summary and conclusions

Fatigue crack growth at two different stress amplitudes was investigated in HPT processed Cu of high as well as commercial purity. In addition, HPT processed high purity Cu samples with a bimodal structure were tested. The results and conclusions are as follows:

- At the *lower stress amplitude* applied, crack propagation rates are independent of purity, and grain coarsening occurs in the vicinity of the crack. Only the bimodally structured HPT Cu exhibits a stable microstructure in connection with a clearly faster crack propagation. Thus, one can conclude that the occurrence of grain coarsening during fatigue crack propagation leads to a retardation of crack growth.

- In case of a *larger stress amplitude* where coarsening does not take place, all tested HPT materials show the same crack growth rate within the error bar.
- Measurements with a change of the stress amplitude also revealed that the crack propagation rate is strongly sensitive to the coarsening phenomena: a steep change of the applied stress amplitude leads to a gradual change of both, the size of the coarsened area as well as the rate of crack growth.
- Combining these results with our previous investigations on the cyclic deformation behaviour of HPT Cu as well as with thermal stability measurements, it seems that grain coarsening in the presence of a fatigue crack depends more on the stored energy of the material while a similar coarsening during cyclic deformation tests in the HCF regime depends more on the activation enthalpy for migration/annealing of defects.

10 Summary and conclusions

This thesis investigated different aspects concerning the mechanical behaviour of nano-structured materials processed by HPT. First, the tensile properties of HPT processed Cu and Cu-Al alloys were analysed with respect to dislocation density and arrangement. Second, fatigue crack propagation as well as fatigue strength in HPT Cu of different purity and microstructural stability was studied. All the obtained results are summarised here.

In the first chapter (p. 63) the **tensile strength and ductility of HPT Cu, Cu-5at%Al and Cu-15at%Al** were investigated. These alloys have stacking fault energies of 45.5, 24.5 and 5.5 mJ/m² [150], respectively. It was expected that the lower stacking fault energy leads to deformation by mechanical twinning instead of dislocation glide [27, p. 297] resulting in a high density of twin boundaries in the HPT processed materials [11, 15]. HPT processing was performed with 5 rotations and a pressure of 6 GPa at RT and at liquid nitrogen temperature. This resulted in an equivalent von Mises strain of approximately 76 at the gauge section of the tensile specimens.

Concerning the microstructure, the domain sizes, dislocation densities and twin densities of the HPT processed alloys were determined by X-ray line profile analysis. The grain size of HPT processed pure Cu was determined by SEM micrography. All the grain size and domain size values were in the submicron and nanometer regime, the smallest domain size – 38 nm – was obtained for Cu-15Al HPT processed at 77K. A higher alloy content as well as lower temperature during HPT both led to smaller grain or domain size, higher dislocation density and higher twin density in case of the alloys.

From DSC experiments it was concluded that Cu-15Al, an alloy which has a tendency to short-range order, did not exhibit any detectable SRO after quenching and HPT deformation.

The average values of yield strength and ultimate tensile strength obtained from several engineering stress-strain curves showed that the ultimate tensile strength increased with increasing alloy content as well as with decreasing processing temperature. In case of the yield strength, the second trend was not that clear due to a relatively large scatter of the data. At any case, also the yield strength, which was in the range of 375 MPa to approximately 750 MPa, was considerably higher for alloys with higher Al content. The uniform elongation values obtained from the tensile tests were in the range of approximately 2% to 3%. A monotonous tendency with respect to the alloy content was not observed. In case of HPT at RT, Cu-5Al had the highest uniform elongation, Cu-15Al the lowest. There was a slight tendency for higher uniform elongation values in case of low temperature HPT, however, the differences were rather small and mainly within the error range. The total elongation decreased with increasing alloy content and was in the range of 8% to 20%. Generally, the results of the tensile tests were in good agreement with the work of An et al. [19], who used the same HPT parameters.

A comparison of own values and literature data [15, 17–19] of the **yield strength** of SPD nanostructured Cu-Al alloys with measurements of the Hall-Petch coefficient of coarse grain Cu-Al revealed substantial deviations. The strength of these materials cannot be ascribed to the limited grain size only. For the sake of an alternative explanation, the yield strength was analysed in terms of the Taylor equation and the measured dislocation densities. Thereby, a good agreement with dislocation hardening according to the Taylor equation including α -parameter values being consistent with large strain plasticity theory was achieved: The obtained parameter α representing the dislocation arrangement was rather low in HPT processed Cu-Al alloys. This means that the dislocations are mainly arranged in structures which exhibit a large screening effect of the individual strain fields as it is for example the case for polarised tilt walls.

Concerning the **ductility**, it could be concluded from own results as well as from literature [15–19] that the largest influence on the uniform elongation arises from the processing parameters or the specific SPD technique used. A detailed analysis revealed that a low-stress arrangement of dislocations after SPD processing is beneficial for the uniform elongation. Such an arrangement is preferentially formed by a combination of high hydrostatic pressure and high applied strain as well as the subsequent relaxation. The release of the pressure is thereby an important condition because during this unloading a considerable rearrangement to dislocation structures with low internal stresses occurs [82]. The influences of stacking fault energy and twin density on the ductility of SPD Cu-Al alloys are much less important than that of the dislocation arrangement.

In the second chapter (p. 83), **HPT Cu of high and commercial purity** were examined for their **high cycle fatigue and fatigue crack propagation behaviour**. Discs with 10 mm diameter were deformed at a pressure of 4 GPa to an equivalent von Mises strain of approximately 24 at the measurement area (corresponding to 2 rotations). As a third material, high purity HPT Cu after an annealing heat treatment at 150°C for 3 min was investigated. This heat treatment led to a bimodal grain size distribution and a considerable increase of ductility, however, at the cost of strength.

Fatigue life time curves in the range of 10^6 to 10^9 cycles to failure were obtained using flat and notched specimens and an ultrasonic resonance fatigue testing system operating at $R = -1$ (push-pull loading with zero mean strain). The results showed that commercial purity HPT Cu, which had smaller grain size and higher tensile strength than the high purity HPT material, also exhibited higher fatigue strength. It was already shown previously by the author [22] that the stability of the microstructure is of utmost importance for the fatigue behaviour of nanostructured materials. The microstructure of commercial purity HPT Cu was stable during cyclic loading in the HCF regime, but high purity HPT Cu showed grain coarsening at high number of loading cycles which had a detrimental effect on the fatigue life time. Although the heat treated bimodally

structured HPT Cu had a higher microstructural stability than the high purity HPT Cu, an improvement of the fatigue performance was not observed and also this material showed grain coarsening at high number of loading cycles. An overview of all results of the cyclic loading tests in the HCF regime is presented in fig. 10.1.

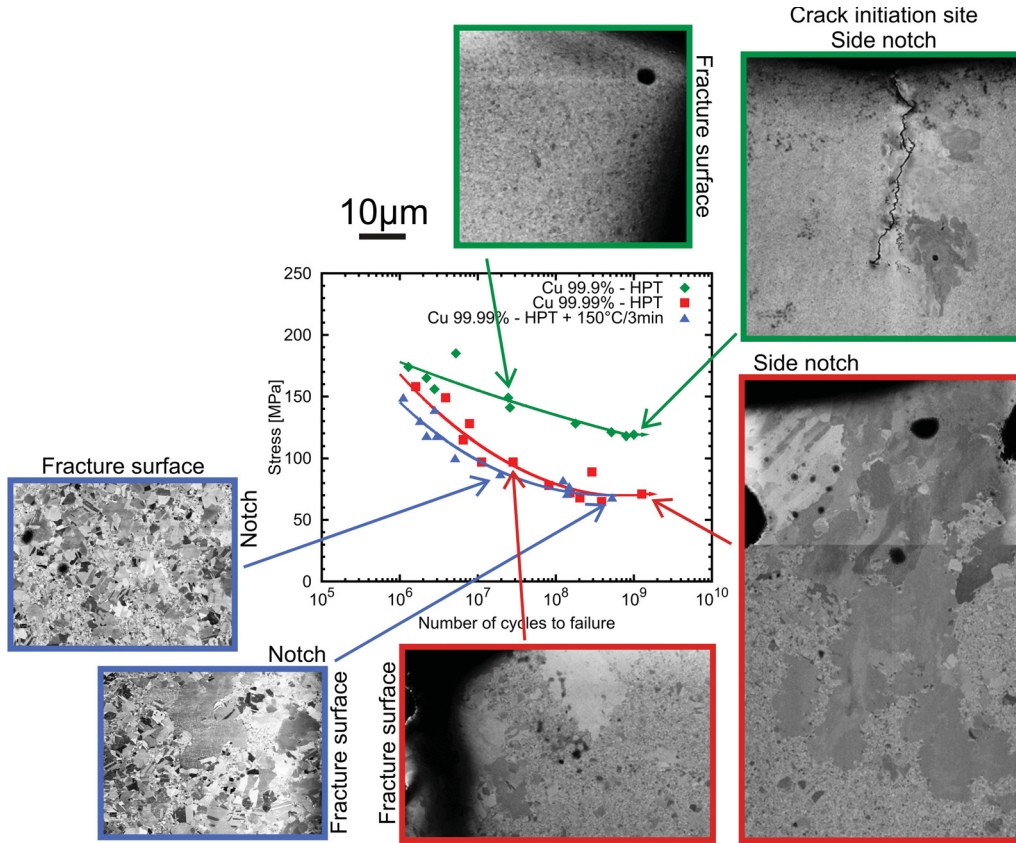


Figure 10.1: S-N curves and microstructure of cyclically loaded HPT processed Cu. The scale bar is valid for all the SEM micrographs.

Fatigue crack growth rates of the same three HPT processed materials as well as of CG Cu were determined using center-notched specimens and again the ultrasonic resonance fatigue testing system. Thereby, it was for the first time possible to measure crack growth rates in HPT Cu down to 10^{-12} m/cycle.

The threshold stress intensity factor range (ΔK_{th}) obtained by the load shedding technique was approximately $3 \text{ MPa}\sqrt{\text{m}}$ for all the HPT processed material. This is lower than the value obtained for CG Cu ($\sim 4 \text{ MPa}\sqrt{\text{m}}$). Also the crack paths were apparently straighter than in coarse grained Cu. This had been observed previously for different nanostructured materials (e.g. [113, 114, 172]) and it was argued that the lack of roughness-induced crack closure leads to higher crack growth rates and lower threshold values for nanostructured materials. However, at $R = -1$ [169] the influence of crack closure is

limited and the differences observed within this study were therefore smaller than what has been reported in the literature.

A further main finding presented in this chapter was that **grain coarsening** near the crack tip occurred in high purity HPT Cu beneath crack growth rates of 10^{-10} m/cycle, and large surface slip marks formed within these coarsened grains. Detailed investigation showed that the size of the coarsened area increased with decreasing crack growth rate (or decreasing applied stress amplitude). Therefore, the origin of the coarsening can be found in the dissipated energy per unit surface created.

The bimodally structured high purity HPT Cu showed no grain coarsening together with slightly higher crack growth rates. This is an indication that deformation-induced grain coarsening can lead to a retardation of the fatigue crack growth. This issue has been studied in more detail within the next chapter (p. 91). For that purpose, fatigue crack growth measurements were performed at two different constant stress amplitudes. Grain coarsening was observed in high purity HPT Cu at the lower constant stress amplitude applied (42 MPa), but not at the higher stress amplitude (55 MPa).

The investigations at low constant stress amplitude showed that grain coarsening in the vicinity of the crack occurred not only in high purity but also in commercial purity HPT Cu. Only the bimodally structured material exhibited a stable microstructure together with higher crack growth rates. At the higher stress amplitude none of the materials showed significant grain coarsening and all of them exhibited – within the error range – the same crack growth rate, being considerably larger than that of CG Cu.

The most important conclusion which was drawn from these experiments is that grain coarsening at the crack tip at low applied stress amplitudes leads to a retardation of the fatigue crack propagation. If the grains in front of the crack tip coarsen, the dissipated energy during cycling is transformed into plastic deformation and movement of grain boundaries instead of crack advance. The crack has then to grow through a distinctly different microstructure, i.e. through coarse, ductile grains.

Further experiments were undertaken to investigate in more detail the correlation between grain coarsening and crack growth rate. They revealed that a steep increase of the applied stress amplitude in high purity HPT Cu did not result in a steep increase of the crack growth rate but rather in a gradual increase as long as the crack tip was within the previously coarsened area. The size of the coarsened area also decreased only gradually. In case of a steep decrease of the stress amplitude there was also a continuous transition of crack growth rate and size of the coarsened area. This behaviour was also observed in commercial purity HPT Cu but not in the bimodally structured material and confirmed the large influence of grain coarsening on the fatigue crack propagation rate of nanostructured materials.

In the following it had been attempted to **understand the observed phenomena in the frame work of varying thermal stability**. For this purpose specific DSC investigations had been performed. The DSC results showed that commercial purity HPT Cu had a higher microstructural stability and annealing of defects occurred at a temperature which was approximately 70°C higher than in case of high purity HPT Cu. The bimodally structured high purity HPT Cu had the same annealing temperature as its non-heat treated counterpart (155°C) but a distinctly lower stored energy than the other two investigated materials.

Grain coarsening during cyclic loading in the HCF regime occurred in the high purity HPT Cu as well as in the bimodally structured one whereas during fatigue crack growth it occurred in HPT Cu irrespectively of the purity except of the bimodally structured one. Furthermore, in case of cyclic loading, an accumulated plastic strain was necessary for grain coarsening, i.e. coarsening was more pronounced at higher number of loading cycles / lower loading amplitude. As mentioned before, in case of fatigue crack growth the amount of coarsening depended on the dissipated energy per crack length extension, i.e. it was more pronounced at lower crack growth rates / lower loading amplitudes.

All these results from crack propagation as well as those from the fatigue life time tests suggest the following common explanation: Considering both, the thermal stability of the investigated materials as well as the specific occurrence of deformation-induced grain coarsening, it seems that two conditions have to be fulfilled at the same time: (i) the stored energy in the material has to reach a certain value and (ii) the activation barrier for the migration of SPD-induced defects (corresponding to the measured annealing temperature) has to be overcome. During crack growth the second condition is fulfilled in all investigated HPT materials due to a very local release of energy at the crack tip. However, the stored energy does not change. Thus, condition (i) is not fulfilled for all materials and grain coarsening occurs only in materials which have an initially high stored energy – as it is true for the non-heat treated HPT materials. During cyclic loading in the HCF regime, energy is distributed in a much larger volume leading to an increase of the overall stored energy. However, in commercial purity HPT Cu, which has a higher stability, the activation barrier cannot be overcome and condition (ii) is not fulfilled. Therefore, this material shows no grain coarsening in HCF tests.

Concerning the overall resistance against cyclic loading, it can be summarised that nanostructured HPT Cu shows a better resistance against fatigue crack initiation and therefore higher fatigue strength but a lower resistance against crack propagation compared to CG material – both at least as long as the microstructure is stable. Grain coarsening during cyclic loading in the HCF regime occurred in high purity HPT Cu and had a detrimental effect on the fatigue life. On the other hand, its occurrence during fatigue crack propagation led to a retardation of the crack growth.

11 Outlook

Based on the results of the tensile tests on HPT Cu-Al alloys, one could think about an optimisation of the structure within the nanostructured grains of SPD materials with respect to the mechanical properties. It would be a further interesting investigation to systematically modify and carefully measure the dislocation arrangement in SPD processed materials. This could be achieved by a systematic change of the processing parameters of HPT as well as ECAP. Achieving a high density of dislocations in a low-stress arrangement is expected to result in a good combination of high strength and ductility.

Another interesting material is the Cu-Al-Zn alloy reported in the appendix. Surprisingly it showed a higher strength after HPT at room temperature than after HPT at liquid nitrogen temperature. The reason for this is unknown. The XRD as well as the DSC investigations showed no indications of second phase particles or precipitations. Thus, a very detailed and quantitative microstructural analysis would shed more light on this puzzle.

PART IV

APPENDIX

A HPT processed Cu after heat treatment

The materials investigated for fatigue and crack propagation are primary the same as in my diploma work [22], namely high purity (99.99%) and commercial purity (99.9%) Cu processed by HPT, and furthermore high purity HPT Cu with a bimodal grain size distribution. The latter should have better uniform elongation as the as-HPT processed material but still rather high strength [92]. For this purpose, a heat treatment was done in an oil bath for 3 minutes, and strength and ductility were measured for different annealing temperatures to find the optimum balance.

The HPT samples had a diameter of 8 mm, the applied pressure was 4 GPa and the strain (γ_t) was 42 at a radius of 2 mm (corresponding to 2 rotations). Tensile strength and uniform elongation after heat treatments at different temperatures are shown in fig. A.1.

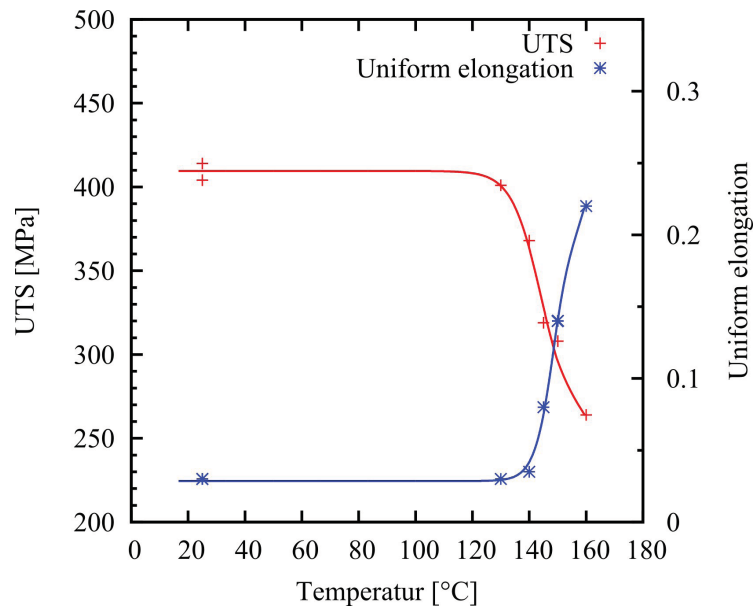


Figure A.1: Tensile strength and ductility of high purity HPT Cu after a 3 min heat treatment, strain rate $5 \times 10^{-4} \text{ s}^{-1}$. The lines are guides for the eye.

It can be seen that at annealing temperatures above 130°C the tensile strength decreases with increasing annealing temperature while the uniform elongation increases. SEM micrographs of the heat treated specimens can be seen in fig. A.2. For all temperatures the microstructure consists of coarse grains with sizes of 1 – 5 μm and residual nanostructured areas. The volume fraction of the coarsened grains is larger at higher annealing temperatures.

A heat treatment at 150°C for 3 min leads to the desired balance between strength and ductility. This material was then ready to be investigated in cyclic loading experiments in the high cycle fatigue regime as well as in fatigue crack growth measurements.

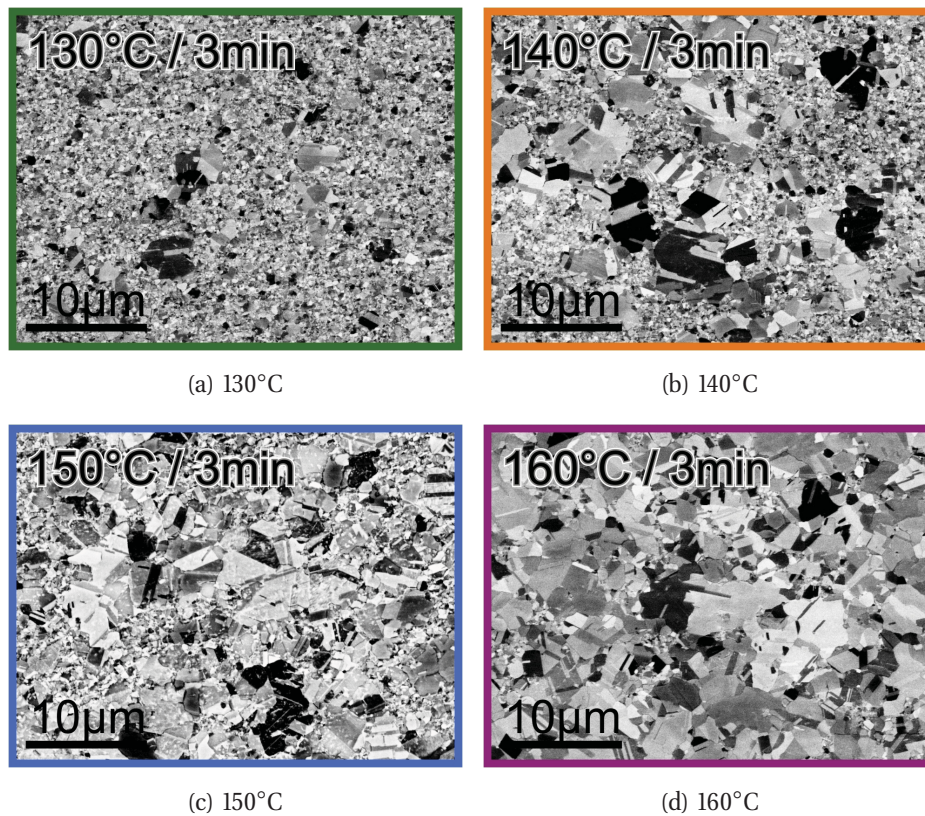


Figure A.2: Microstructure of high purity HPT Cu after a 3 min heat treatment as seen in the SEM using the backscattered electron detector.

In case of commercial purity HPT Cu it was not possible to gain such a bimodal grain size distribution with short-time heat treatments. With increasing temperature, the tensile strength decreased but the uniform elongation did not increase. However, samples with that purity showed a better thermal stability – the ultimate tensile strength did not decrease in case of 3 min heat treatments below 200°C.

B Microstructure and strength of quenched Cu and Cu-Al alloys

The microstructures of the initial annealed and quenched materials which were used for the investigations in section 7 have been characterised by light microscopy of polished and etched samples. The results can be seen in fig. B.1: The grain sizes are in the range of about 50 μm and below in case of pure Cu and Cu-5Al, and in the range of 500 μm in case of Cu-15Al. The raw materials were provided by different companies and it seems that the annealing temperatures were not high enough to induce marked grain growth.

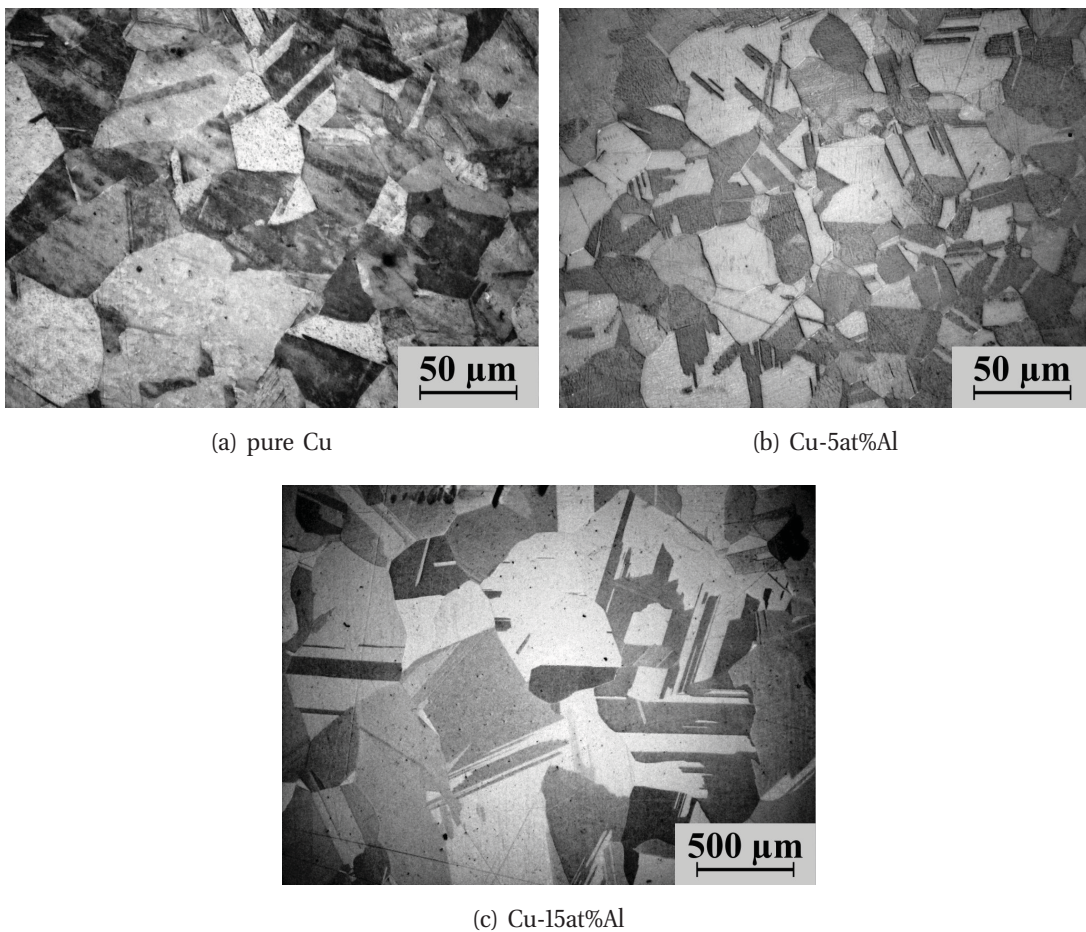


Figure B.1: Microstructure of Cu and Cu-Al alloys before HPT.

Table B.1 summarises the values of hardness and tensile strength of the initial materials. Both increase with increasing alloy content but it can be seen from the tensile curves (fig. B.2) that the work hardening behaviour of the samples is quite different, which also results in a strongly varying ductility. This can be ascribed to the different grain sizes. After HPT processing to large strains these differences of the initial materials are not

relevant any more but still a comparison between HPT processed and initial materials has to be done with great care.

Table B.1: Values of microhardness and tensile strength of annealed and quenched materials. (In case of Cu-15Al only one valid tensile curve was achieved.)

Material	HV 0.1	UTS [MPa]
Cu	58 ± 1	212 ± 8
Cu-5Al	75 ± 4	281 ± 4
Cu-15Al	112 ± 2	297

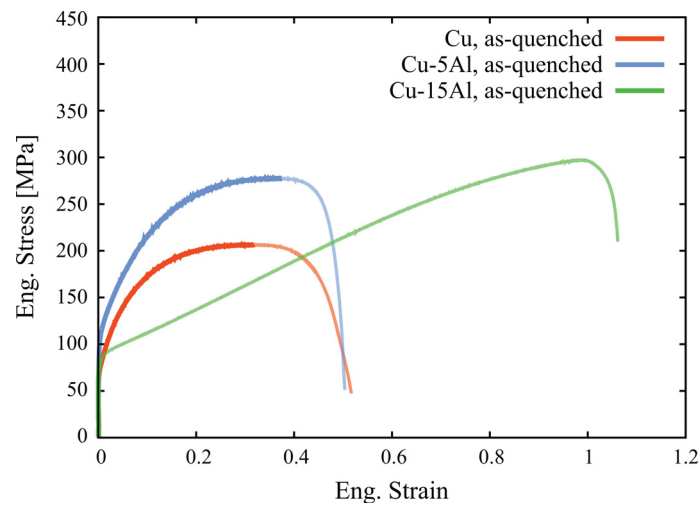


Figure B.2: Exemplary tensile test curves of the as-quenched materials.³

³The bold parts of the tensile curves were directly measured by the laser speckle sensor while the thinner plotted parts are gained from the cross head movement. In case of Cu-15Al a direct strain measurement was only possible in the very beginning (to about the yield strength) because the sample surface changed too much during testing due to the evolution of surface roughness.

C Short-range order in Cu-Al

C.1 Introduction

The interaction energies between the different types of atoms in an alloy determine whether a solid solution, a phase decomposition or ordering is the thermodynamically favourable state [27, p. 112ff]. Ordering takes place if there is an attractive force between the unlike elements. If this force is only small, the order will not expand over the whole crystal (long-range order), but only over a certain distance – this state is called “short-range order” (SRO). Binary alloy compositions showing short-range order can be found for example in Cu-Al, Au-Fe or Ag-Zn [154].

Short-range order is only stable up to a certain temperature. When rapidly cooling or quenching a material from high temperature, the state of this temperature is frozen, and SRO can be avoided. The formation of the specific degree of short-range order which is in thermodynamic equilibrium at a certain temperature occurs via vacancy diffusion [154, p. 4]. Therefore, a high amount of vacancies helps to quickly establish a high degree of SRO.

Short-range order influences the mechanical behaviour of a material. It leads to planar glide of dislocations, meaning that only few glide planes are activated and that plastic deformation becomes inhomogeneous [179]. If a dislocation wants to pass through a short-range ordered crystal, a certain additional stress has to be applied. But if the first – the leading – dislocation has passed the SRO zone, the order is destroyed and subsequent dislocations can pass easier. This can lead to an avalanche-like behaviour and jerky flow [154, p. 14] and also implies that SRO can be destroyed by deformation.

The degree of SRO existing in a material can be determined either by residual resistivity measurements where an increase of SRO leads to a decrease of resistivity [180], or by differential scanning calorimetry (DSC). In this case, an increase of SRO and the concomitant annealing of vacancies lead to an exothermic peak. The dissolution of SRO at higher temperatures – on the other hand – leads to an endothermic peak [154, p. 68].

C.2 Short-range order in quenched Cu-Al alloys

To get an idea about the amount of short-range order existing in the as-quenched Cu-Al alloys, DSC measurements were performed. The results can be seen in fig. C.1. In the first-heating curves (the upper curves, belonging to the legend on the left side) small exothermic peaks can be found. Cu-5Al reveals a peak at 358°C, Cu-15Al shows two peaks at 154°C and 348°C. After the first heating, the samples were cooled to room temperature using a cooling rate of 10 K/min and heated up again. The second-heating curve of Cu-15Al shows a step with an onset temperature of 270°C.

When comparing these results with literature [154] the following conclusions can be

drawn: Cu-5Al has no tendency to short-range order. The (very small) peak at 358°C is due to the annealing of some defects. In contrast, Cu-15Al has a tendency to SRO. But as the material has been quenched from a high temperature, the degree of SRO in the beginning is rather low. During heating in the DSC, SRO forms, resulting in an exothermic peak at about 150°C. During further heating, the SRO is again destroyed. This can be seen very clearly in form of a step in the second-heating curve. But also in the first-heating curve, there is a little step at the same temperature. Furthermore, there is an exothermic peak at about 350°C in the first-heating curve due to the annealing of defects.

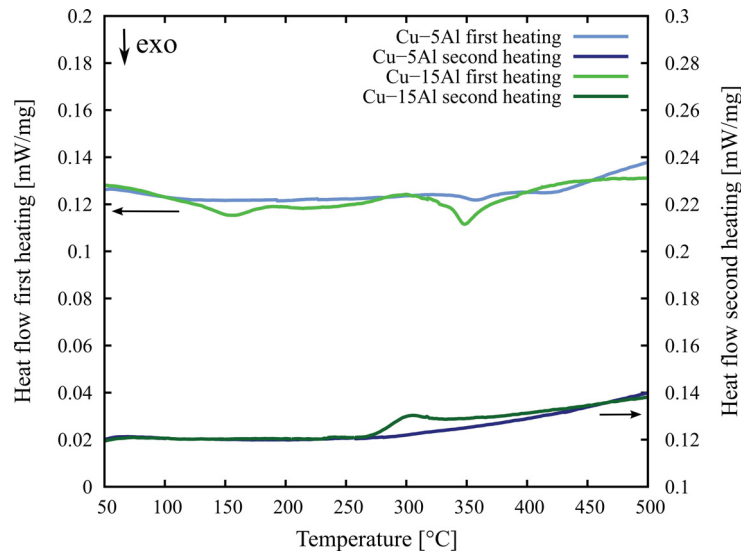


Figure C.1: DSC scans of as-quenched Cu-5%Al and Cu-15%Al. The curves of the first and the second heating are shown on two separate axes to make it easier to distinguish them.

C.3 Short-range order after HPT processing and order hardening

For a proper classification of the DSC peaks in HPT processed materials, additional microhardness measurements have been performed. Samples of Cu-5Al and Cu-15Al processed by HPT at RT have been heated up in the DSC to a certain temperature, then cooled down to room temperature again and afterwards the microhardness has been measured. The temperatures have been chosen before and after the peaks in the DSC curves. The microhardness data can be seen in combination with the DSC curves in fig. C.2 for Cu-5Al and in fig. C.3 for Cu-15Al, both processed by HPT at room temperature.

Cu-5Al shows a large decrease of hardness between 245°C and 335°C, i.e. at the position of the peak in fig. C.2. It can therefore be attributed to the annealing of defects, mainly dislocations. Afterwards, there is another decrease of hardness up to 500°C without detectable DSC signal, which is due to (secondary) grain growth.

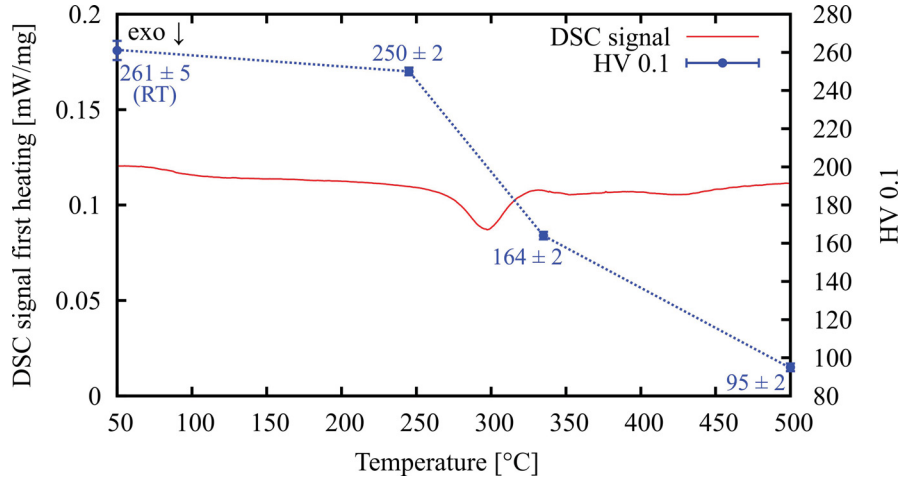
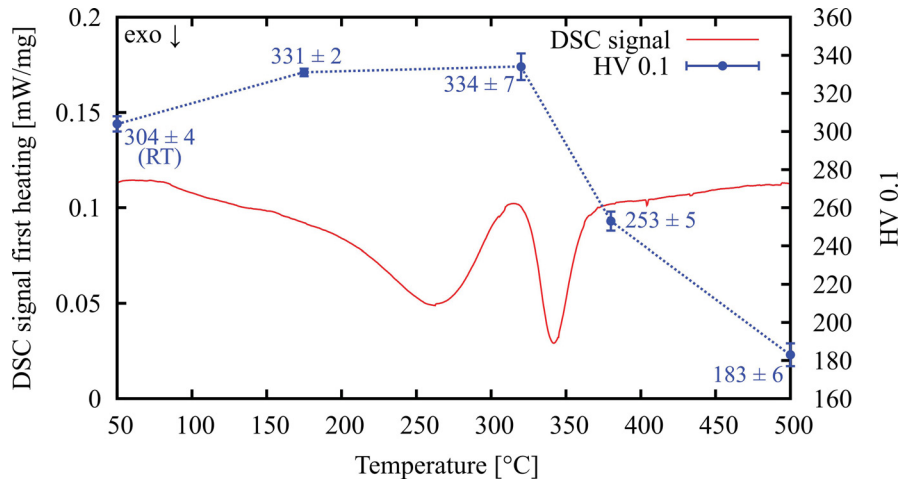


Figure C.2: DSC scan and corresponding microhardness of Cu-5Al after HPT at RT.

Figure C.3: DSC scan and corresponding microhardness of Cu-15Al after HPT at RT.
The second scan not shown here looks like the second scan after quenching.

The situation is more complex in Cu-15Al where heating up until 320°C leads to an increase of microhardness. Two peaks can be seen in the DSC scan in this range. The subsequent third DSC peak then is accompanied by a marked decrease of hardness and can thus be attributed to defect annealing. It can therefore be concluded that the first DSC peak is due to the evolution of SRO implying that the material after HPT possessed no SRO. Hardening due to the evolution of SRO is a well-known effect [135] and a very similar behaviour was found in the work of Spanl [154]. The dissolution of SRO at about 250°C to 300°C cannot be seen in the microhardness measurements because when we cool down the sample, SRO will establish again.

To sum up, it has been shown that although Cu-15Al has a tendency to short-range order, the order is destroyed by quenching and even more by HPT deformation. Cu-5Al – just like pure Cu – does generally not show short-range order.

D Comparison of literature on SPD Cu-Al alloys

Table D.1: Data used in fig. 7.1, 7.2, 7.7 & 7.9. The uniform elongation includes the elastic strain. Data marked with * are obtained from diagrams, data with † from stress-strain curves printed in the corresponding papers.

Reference	Material (at%Al)	SFE [mJ/m ²]	Processing	Grain size [nm]	Geometry of tensile test samples	Strain rate [s ⁻¹]	$\sigma_{0.2}$ [MPa]	UTS [MPa]	ϵ_{unif} [%]	ϵ_{total} [%]
An2008 [16]	Cu-2.3Al	48.5	ECAP, 1 pass		$2 \times 1 \times 8 \text{ mm}^3$	5×10^{-4}		333 *	2.67 *	
	Cu-7.2Al	28.0						496 *	3.35 *	
	Cu-11.6Al	4.5						671 *	5.28 *	
Qu2009 [17]	Cu-5Al	28	ECAP, 4 passes, B _c	107	$2 \times 1 \times 8 \text{ mm}^3$ at least two tests	5×10^{-4}	545	590	1.91	
	Cu-8Al	17	ECAP, 4 passes, B _c	82			670	722	1.96	
	Cu-16Al	6	ECAP, 2 passes, B _c	50			740	862	2.23	
An2011 [19]	Cu 99.97%	78		120	$1 \times 0.5 \times 2 \text{ mm}^3$ at least two tests	5×10^{-4}	445 ± 17 *	514 ± 17 *	3.0 ± 0.3 *	~ 30 †
	Cu-2.3Al	48		100			565 ± 20 *	708 ± 20 *	3.5 ± 0.3 *	~ 25 †
	Cu-5Al	28	HPT, 5 rot, 6 GPa	65			652 ± 20 *	782 ± 24 *	3.6 ± 0.3 *	~ 25 †
	Cu-8Al	17		45			735 ± 20 *	902 *	3.9 ± 0.3 *	~ 25 †
	Cu-16Al	6		30			825 ± 17 *	977 ± 15 *	3.3 ± 0.2 *	~ 15 †
Zhang2011 [15]	Cu 99.995%	78		67	$1 \times 1 \times 5 \text{ mm}^3$ more than 4 tests, laser extensometer	6×10^{-3}	612 *	624 †	1.11 †	~ 9 †
	Cu-1.17Al	60	LNT-DPD (77K,	50			725 *			
	Cu-1.75Al	53	strain rate 10^3 /s ,				753 *			
	Cu-2.3Al	50	$\epsilon=2$	34			771 *	793 †	1.15 †	~ 7 †
	Cu-3.5Al	37					789 *			
	Cu-5Al	25		30			830 *			
	Cu-10Al	12	here only $\epsilon=1.7$	24			866 *	938 †	1.94 †	~ 7.5 †
Zhang2011 [15]	Cu 99.995%	78		297	$1 \times 1 \times 5 \text{ mm}^3$ more than 4 tests, laser extensometer	6×10^{-3}	404 *	407 †	0.97 †	~ 14.5 †
	Cu-1.17Al	60		166			430 *			
	Cu-1.75Al	53	QSC (RT, strain				451 *			
	Cu-2.3Al	50	rate 10^{-1} /s , $\epsilon=2$	160			469 *	490 †	1.24 †	~ 10 †
	Cu-3.5Al	37		112			533 *			
	Cu-5Al	25		60			642 *			
Huang2012 [18]	Cu-10Al	12	here only $\epsilon=1.7$	32	$2 \times 1 \times 8 \text{ mm}^3$ at least 3 tests	5×10^{-4}	837 *	898 †	1.36 †	~ 9 †
	Cu 99.99%	78		314 ± 25			364 ± 23	407 ± 28	1.8 ± 0.5	11.3 ± 2.3
	Cu-2.3Al	48	ECAP, 8 passes, B _c	171 ± 20			449 ± 19	512 ± 20	1.7 ± 0.3	9.8 ± 1.4
	Cu-7.2Al	21		90 ± 20			583 ± 34	698 ± 39	2.3 ± 0.5	10.2 ± 1.5
	Cu-11.6Al	8		57 ± 10			765 ± 21	854 ± 24	3.1 ± 0.4	10.7 ± 2.1

E Tensile properties & DSC of Cu-Al-Zn processed by HPT

Analogue to the Cu-Al alloys also Cu-12.1at%Al-4.1at%Zn was investigated. This solid solution alloy has a stacking fault energy of 7 mJ/m² [181] – almost as low as the value of Cu-15at%Al. Just like the Cu-Al alloys it was first annealed and quenched from 500°C into water and afterwards deformed by HPT at room temperature and at 77K. Five rotations were applied at a hydrostatic pressure of 6 GPa. Tensile tests, DSC and microhardness measurements were performed using the same parameters like in case of the Cu-Al alloys.

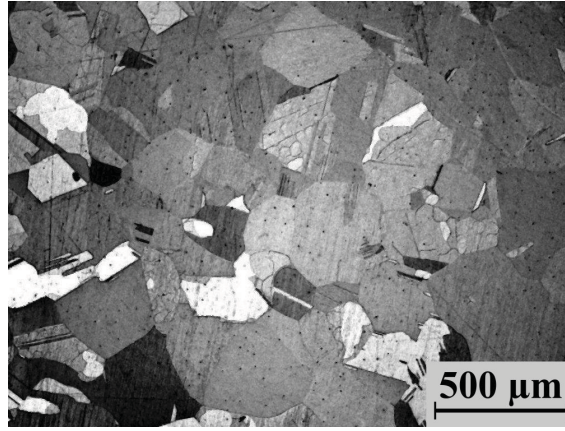


Figure E.1: Microstructure of the Cu-Al-Zn alloy in the as-quenched state.

The microstructure of the alloy before HPT can be seen in fig. E.1, the grain size is in the order of 500 μm. The initial microhardness (HV 0.1) is 113 ± 2 , the tensile strength 326 ± 2 MPa.

After HPT, hardness and tensile strength are markedly increased. Exemplary tensile curves can be seen in fig. E.2, the average values of the tensile properties are gained from three stress-strain curves each and are summarised in table E.1.

Table E.1: Tensile test results: yield strength ($\sigma_{0.2}$), ultimate tensile strength (UTS), uniform elongation and total elongation.

Material	$\sigma_{0.2}$ [MPa]	UTS [MPa]	ϵ_{unif} [%]	ϵ_{total} [%]
Cu-Al-Zn HPT@RT	845 ± 72	1084 ± 26	2.2 ± 0.3	8.6 ± 1.3
Cu-Al-Zn HPT@77K	971 ± 28	985 ± 13	1.8 ± 0.1	7.1 ± 0.3

It can be seen that the tensile strength as well as the uniform and total elongation are higher when HPT processing was performed at RT as if it was done at liquid nitrogen temperature. This is an unexpected result because in pure Cu as well as in the investigated Cu-Al alloys the strength was always higher when HPT processing was done at 77K due

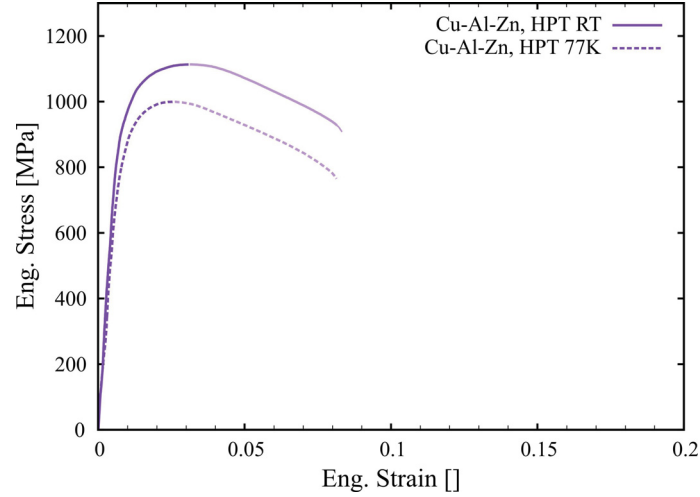


Figure E.2: Exemplary tensile test curves of HPT processed Cu-12.1at%Al-4.1at%Zn.

to higher defect densities and smaller grain sizes. Unfortunately no grain size values are available for this material after HPT processing. The grains are too small to see them in SEM micrographs and the X-ray profile analysis did not yield reliable results because of large scatter and the lack of a global minimum in the profile fits.

It would be very interesting to find the reason for the decreased strength and ductility in low temperature HPT processing, however, this is beyond the scope of this work. A possible explanation could be an HPT-induced phase transformation or the formation of second phase particles during HPT at room temperature which is suppressed at liquid nitrogen temperature. However, no additional peaks have been found in the XRD profiles and also from literature [181] this alloy should be a solid solution.

E.1 Short-range order in the Cu-Al-Zn alloy

Cu-12.1at%Al-4.1at%Zn shows short-range ordering, just like Cu-15Al. The DSC measurement of the as-quenched material (fig. E.3) shows the dissolution of the short-range order at about 300°C in the second-heating curve. In the first-heating curve the evolution of SRO leads to an exothermic peak at about 150°C showing that the alloy in the as-quenched state exhibits no considerable short-range order.

The DSC measurements after HPT processing (fig. E.4) show two peaks associated with the formation of SRO and order hardening, and a subsequent peak due to the annealing of HPT-induced defects. This is very similar to Cu-15Al. But in contrast to Cu-15Al, the Cu-Al-Zn alloy deformed at room temperature shows lower thermal stability than the sample processed by HPT at 77K, i.e. the defect annealing peak is shifted to lower temperature.

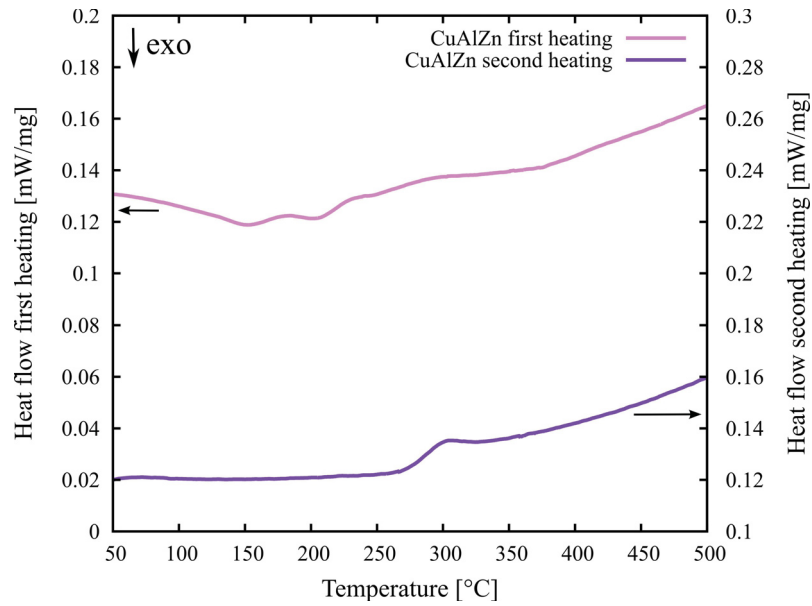


Figure E.3: DSC scans of Cu-Al-Zn in the as-quenched state. The curves of the first and the second heating are shown on two separate axes for a better distinction.

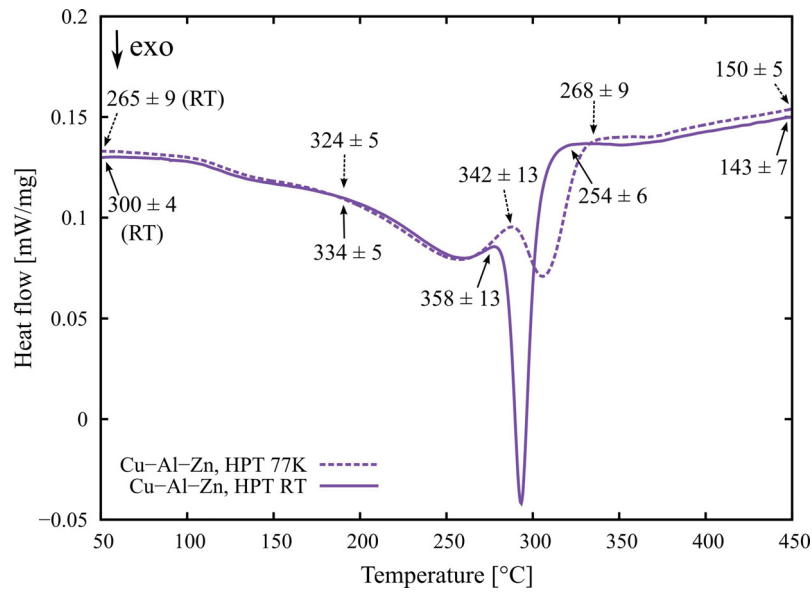


Figure E.4: DSC scans (first heating) of HPT processed Cu-Al-Zn. Corresponding microhardness values (measurement radius 2 mm) of samples annealed in the DSC are also shown. The values above the curves correspond to HPT processing at 77K, the values below to RT processing.

Bibliography

- [1] M.J. Zehetbauer and Y.T. Zhu, eds. *Bulk Nanostructured Materials*. Wiley-VCH (2009).
- [2] R. Pippan, S. Scheriau, A. Hohenwarter and M. Hafok. *Advantages and limitations of HPT: a review*. Materials Science Forum 584-586 (2008) 16–21.
- [3] E. Schafler, A. Dubravina, B. Mingler, H.P. Karnthaler and M. Zehetbauer. *On the microstructure of HPT processed Cu under variation of deformation parameters*. Materials Science Forum 503-504 (2006) 51–56.
- [4] D. Setman, E. Schafler, E. Korznikova and M.J. Zehetbauer. *The presence and nature of vacancy type defects in nanometals detained by severe plastic deformation*. Materials Science and Engineering A 493 (2008) 116–122.
- [5] R. Pippan, S. Scheriau, A. Taylor, M. Hafok, A. Hohenwarter and A. Bachmaier. *Saturation of fragmentation during severe plastic deformation*. Annual Review of Materials Research 40 (2010) 319–343.
- [6] R.Z. Valiev, R.K. Islamgaliev and I.V. Alexandrov. *Bulk nanostructured materials from severe plastic deformation*. Progress in Materials Science 45 (2000) 103–189.
- [7] Y.T. Zhu and T.G. Langdon. *The fundamentals of nanostructured materials processed by severe plastic deformation*. JOM 56 (2004) 58–63.
- [8] K.S. Kumar, H. Van Swygenhoven and S. Suresh. *Mechanical behavior of nanocrystalline metals and alloys*. Acta Materialia 51 (2003) 5743–5774.
- [9] Y. Estrin. *Effects of Severe Plastic Deformation: Mechanical properties and beyond*. Materials Science Forum 503-504 (2006) 91–98.
- [10] M.A. Meyers, A. Mishra and D.J. Benson. *Mechanical properties of nanocrystalline materials*. Progress in Materials Science 51 (2006) 427–556.
- [11] J. Gubicza, N.Q. Chinh, J.L. Lábár, Z. Hegedüs, C. Xu and T.G. Langdon. *Microstructure and yield strength of severely deformed silver*. Scripta Materialia 58 (2008) 775–778.
- [12] L. Balogh, T. Ungár, Y. Zhao, Y.T. Zhu, Z. Horita, C. Xu and T.G. Langdon. *Influence of stacking-fault energy on microstructural characteristics of ultrafine-grain copper and copper–zinc alloys*. Acta Materialia 56 (2008) 809–820.
- [13] Y. Zhang, N.R. Tao and K. Lu. *Effect of stacking-fault energy on deformation twin thickness in Cu–Al alloys*. Scripta Materialia 60 (2009) 211–213.
- [14] Y.S. Li, Y. Zhang, N.R. Tao and K. Lu. *Effect of the Zener–Hollomon parameter on the microstructures and mechanical properties of Cu subjected to plastic deformation*. Acta Materialia 57 (2009) 761–772.
- [15] Y. Zhang, N.R. Tao and K. Lu. *Effects of stacking fault energy, strain rate and temperature on microstructure and strength of nanostructured Cu–Al alloys subjected to plastic deformation*. Acta Materialia 59 (2011) 6048–6058.

- [16] X.H. An, W.Z. Han, C.X. Huang, P. Zhang, G. Yang, S.D. Wu and Z.F. Zhang. *High strength and utilizable ductility of bulk ultrafine-grained Cu–Al alloys*. Applied Physics Letters 92 (2008) 201915.
- [17] S. Qu, X.H. An, H.J. Yang, C.X. Huang, G. Yang, Q.S. Zang, Z.G. Wang, S.D. Wu and Z.F. Zhang. *Microstructural evolution and mechanical properties of Cu–Al alloys subjected to equal channel angular pressing*. Acta Materialia 57 (2009) 1586–1601.
- [18] C.X. Huang, W. Hu, G. Yang, Z.F. Zhang, S.D. Wu, Q.Y. Wang and G. Gottstein. *The effect of stacking fault energy on equilibrium grain size and tensile properties of nanostructured copper and copper–aluminum alloys processed by equal channel angular pressing*. Materials Science & Engineering A 556 (2012) 638–647.
- [19] X.H. An, Q.Y. Lin, S.D. Wu, Z.F. Zhang, R.B. Figueiredo, N. Gao and T.G. Langdon. *The influence of stacking fault energy on the mechanical properties of nanostructured Cu and Cu–Al alloys processed by high-pressure torsion*. Scripta Materialia 64 (2011) 954–957.
- [20] Y.H. Zhao, X.Z. Liao, Z. Horita, T.G. Langdon and Y.T. Zhu. *Determining the optimal stacking fault energy for achieving high ductility in ultrafine-grained Cu–Zn alloys*. Materials Science and Engineering A 493 (2008) 123–129.
- [21] Y.H. Zhao, Y.T. Zhu, X.Z. Liao, Z. Horita and T.G. Langdon. *Tailoring stacking fault energy for high ductility and high strength in ultrafine grained Cu and its alloy*. Applied Physics Letters 89 (2006) 121906.
- [22] J. Horky. *Ermüdungsverhalten von hochdruck-tordiertem Kupfer*. Master's thesis, University of Vienna (2008).
- [23] G. Khatibi, J. Horky, B. Weiss and M.J. Zehetbauer. *High cycle fatigue behaviour of copper deformed by high pressure torsion*. International Journal of Fatigue 32 (2010) 269–278.
- [24] H.W. Höppel, Z.M. Zhou, H. Mughrabi and R.Z. Valiev. *Microstructural study of the parameters governing coarsening and cyclic softening in fatigued ultrafine-grained copper*. Philosophical Magazine A 82 (2002) 1781–1794.
- [25] H. Mughrabi and H.W. Höppel. *Cyclic deformation and fatigue properties of very fine-grained metals and alloys*. International Journal of Fatigue 32 (2010) 1413–1427.
- [26] K. Zhang and J.R. Weertman. *Microstructural Changes Produced by Fatigue in High-Purity Copper Severely Deformed by Cryogenic Rolling*. Metallurgical and Materials Transactions A 40A (2009) 2255–2263.
- [27] G. Gottstein. *Physikalische Grundlagen der Materialkunde*. Springer (2007).
- [28] D.E. Laughlin and K. Hono, eds. *Physical Metallurgy*. Elsevier (2014).
- [29] P. Haasen. *Physikalische Metallkunde*. Springer (1994).
- [30] D.R. Askeland and P. Webster. *The science and engineering of materials*. Chapman and Hall (1990).
- [31] H. Böhm. *Einführung in die Metallkunde*. B.I. Wissenschaftsverlag (1992).

-
- [32] R.E. Smallman and A.H.W. Ngan. *Modern Physical Metallurgy*. Elsevier (2013).
- [33] M. Zehetbauer. *Effects of non-equilibrium vacancies on strengthening*. Key Engineering Materials 97-98 (1994) 287–306.
- [34] B. Ilchner and R.F. Singer. *Werkstoffwissenschaften und Fertigungstechnik*. Springer (2010).
- [35] J.W. Christian and S. Mahajan. *Deformation twinning*. Progress in Materials Science 39 (1995) 1–157.
- [36] C. Zener and J.H. Hollomon. *Effect of strain rate upon plastic flow of steel*. Journal of Applied Physics 15 (1944) 22–32.
- [37] *Ductility*. Papers presented at a Seminar of the American Society for Metals October 14 and 15, 1967. American Society for Metals (1968).
- [38] T.H. Courtney. *Mechanical behavior of materials*. McGraw-Hill (1990).
- [39] G.I. Taylor. *The mechanism of plastic deformation of crystals. Part I. Theoretical*. Proceedings of the Royal Society A 145 (1934) 362–387.
- [40] E.O. Hall. *The Deformation and Ageing of Mild Steel: III Discussion of Results*. Proceedings of the Physical Society B 64 (1951) 747–753.
- [41] R.W. Armstrong, I. Codd, R.M. Douthwaite and N.J. Petch. *The plastic deformation of polycrystalline aggregates*. Philosophical Magazine 7 (1962) 45–58.
- [42] N. Chandra. *Constitutive behavior of superplastic materials*. International Journal of Non-Linear Mechanics 37 (2002) 461–484.
- [43] S.H. Crandall and N.C. Dahl. *An Introduction to the Mechanics of Solids*. McGraw-Hill (1978).
- [44] Y.H. Zhao, Y.Z. Guo, Q. Wei, A.M. Dangelewicz, C. Xu, Y.T. Zhu, T.G. Langdon, Y.Z. Zhou and E.J. Lavernia. *Influence of specimen dimensions on the tensile behavior of ultrafine-grained Cu*. Scripta Materialia 59 (2008) 627–630.
- [45] O.B. Kulyasova, R.K. Islamgaliev and R.Z. Valiev. *On the specific features of tensile tests of small samples of nanostructured materials*. The Physics of Metals and Metallography 100 (2005) 277–283.
- [46] H.-J. Bargel and G. Schulze. *Werkstoffkunde*. Springer (2008).
- [47] M. Klesnil and P. Lukáš. *Fatigue of Metallic Materials*. Elsevier Scientific Publishing Company (1980).
- [48] S. Suresh. *Fatigue of Materials*. Cambridge University Press (1991).
- [49] H. Mughrabi. *Specific features and mechanisms of fatigue in the ultrahigh-cycle regime*. International Journal of Fatigue 28 (2006) 1501–1508.
- [50] F. Ellyin. *Fatigue damage, crack growth and life prediction*. Chapman & Hall (1997).
- [51] R.E. Peterson. *Stress concentration factors*. John Wiley and Sons (2008).

- [52] L. Pook. *Metal Fatigue*. Springer (2007).
- [53] F.S. Silva. *The importance of compressive stresses on fatigue crack propagation rate*. International Journal of Fatigue 27 (2005) 1441–1452.
- [54] A. Hadrboletz. *Rissausbreitung im Bereich kleiner Wachstumsraten bei schwingender Beanspruchung in kubisch flächenzentrierten Metallen*. Ph.D. thesis, Universität Wien (1983).
- [55] H.A. Padilla II and B.L. Boyce. *A Review of fatigue behavior in nanocrystalline metals*. Experimental Mechanics 50 (2010) 5–23.
- [56] H.-J. Fecht. *Nanostructure formation by mechanical attrition*. Nanostructured Materials 6 (1995) 33–42.
- [57] U. Erb. *Electrodeposited nanocrystals: Synthesis, properties and industrial applications*. Nanostructured Materials 6 (1995) 533–538.
- [58] H. Gleiter. *Nanocrystalline materials*. Progress in Materials Science 33 (1989) 223–315.
- [59] C.C. Koch, ed. *Nanostructured Materials - Processing, Properties, and Application*. William Andrew Publishing, USA (2007).
- [60] C. Suryanarayana. *Mechanical alloying and milling*. Progress in Materials Science 46 (2001) 1–184.
- [61] R.Z. Valiev, Y. Estrin, Z. Horita, T.G. Langdon, M.J. Zehetbauer and Y.T. Zhu. *Producing bulk ultrafine-grained materials by severe plastic deformation*. JOM 58(4) (2006) 33–39.
- [62] M.J. Zehetbauer, H.P. Stüwe, A. Vorhauer, E. Schafner and J. Kohout. *The role of hydrostatic pressure in severe plastic deformation*. Advanced Engineering Materials 5 (2003) 330–337.
- [63] G. Wilde. *Synthesis of Bulk Nanocrystalline Materials and Bulk Metallic Glasses by Repeated Cold Rolling and Folding (RCR)*. Materials Science Forum 579 (2008) 109–134.
- [64] M. Lewandowska and K.J. Kurzydowski. *Recent development in grain refinement by hydrostatic extrusion*. Journal of Materials Science 43 (2008) 7299–7306.
- [65] Proceedings. *6th International Conference on Nanostructures by Severe Plastic Deformation*. Materials Science and Engineering, IOP Conference Series (2014).
- [66] Y. Iwahashi, J. Wang, Z. Horita, M. Nemoto and T.G. Langdon. *Principle of Equal-Channel Angular Pressing for the processing of ultra-fine grained materials*. Scripta Materialia 35 (1996) 143–146.
- [67] M. Furukawa, Z. Horita, M. Nemoto and T.G. Langdon. *Processing of metals by equal-channel angular pressing*. Journal of Materials Science 36 (2001) 2835–2843.
- [68] R.Ye. Lapovok. *The positive role of back-pressure in equal channel angular extrusion*. Materials Science Forum 503-504 (2006) 37–44.
- [69] C. Rentenberger, T. Waitz and H.P. Karnthaler. *Formation and structures of bulk nanocrystalline intermetallic alloys studied by transmission electron microscopy*. Materials Science and Engineering A 462 (2007) 283–288.

- [70] G. Rogl, Z. Aabdin, E. Schafler, J. Horky, D. Setman, M. Zehetbauer, M. Kriegisch, O. Eibl, A. Grytsiv, E. Bauer, M. Reinecker, W. Schranz and P. Rogl. *Effect of HPT processing on the structure, thermoelectric and mechanical properties of $\text{Sr}_{0.07}\text{Ba}_{0.07}\text{Yb}_{0.07}\text{Co}_4\text{Sb}_{12}$* . Journal of Alloys and Compounds 537 (2012) 183–189.
- [71] A.D. Rollett and U.F. Kocks. *A review of the stages of work hardening*. Solid State Phenomena 35-36 (1993) 1–18.
- [72] E. Schafler, M. Zehetbauer, I. Kopacz, T. Ungar, P. Hanak, H. Amenitsch and S. Bernstorff. *Microstructural parameters in large strain deformed Ni polycrystals as investigated by synchrotron radiation*. phys. stat. sol. (a) 175 (1999) 501–511.
- [73] H. Mughrabi. *Dislocation wall and cell structures and long-range internal stresses in deformed metal crystals*. Acta Metallurgica 31 (1983) 1367–1379.
- [74] T. Ungár and M. Zehetbauer. *Stage IV work hardening in cell forming materials, part II: A new mechanism*. Scripta Materialia 35 (1996) 1467–1473.
- [75] M. Müller, M. Zehetbauer, A. Borbély and T. Ungár. *Dislocation density and long range internal stresses in heavily cold worked Cu measured by X-ray line broadening*. Zeitschrift für Metallkunde 86 (1995) 827–831.
- [76] M. Zehetbauer and V. Seumer. *Cold work hardening in stages IV and V of f.c.c. metals - I. experiments and interpretation*. Acta Metallurgica et Materialia 41 (1993) 577–588.
- [77] F.J. Humphreys and M. Hatherly. *Recrystallization and related annealing phenomena*. Pergamon (1995).
- [78] R.B. Figueiredo and T. G. Langdon. *Grain refinement and mechanical behavior of a magnesium alloy processed by ECAP*. Journal of Materials Science 45 (2010) 4827–4836.
- [79] S.X. Ding, C.P. Chang and P.W. Kao. *Effects of processing parameters on the grain refinement of magnesium alloy by equal-channel angular extrusion*. Metallurgical and Materials Transactions A 40 (2009) 415–425.
- [80] T. Hebesberger, H.P. Stüwe, A. Vorhauer, F. Wetscher and R. Pippan. *Structure of Cu deformed by high pressure torsion*. Acta Materialia 53 (2005) 393–402.
- [81] Y. Iwahashi, Z. Horita, M. Nemoto and T.G. Langdon. *The process of grain refinement in equal-channel angular pressing*. Acta Materialia 46 (1998) 3317–3331.
- [82] E. Schafler. *Effects of releasing the hydrostatic pressure on the nanostructure after severe plastic deformation of Cu*. Scripta Materialia 62 (2010) 423–426.
- [83] E. Schafler. *Strength response upon pressure release after high pressure torsion deformation*. Scripta Materialia 64 (2011) 130–132.
- [84] J. Gubicza, L. Balogh, R.J. Hellmig, Y. Estrin and T. Ungár. *Dislocation structure and crystallite size in severely deformed copper by X-ray peak profile analysis*. Materials Science and Engineering A 400-401 (2005) 334–338.

- [85] E. Schafler, G. Steiner, E. Korznikova, M. Kerber and M.J. Zehetbauer. *Lattice defect investigation of ECAP-Cu by means of X-ray line profile analysis, calorimetry and electrical resistometry*. Materials Science and Engineering A 410-411 (2005) 169–173.
- [86] J. Gubicza, N.Q. Chinh, J.L. Lábár, S. Dobatkin, Z. Hegedüs and T.G. Langdon. *Correlation between microstructure and mechanical properties of severely deformed metals*. Journal of Alloys and Compounds 483 (2009) 271–274.
- [87] W.-J. Kim, C.-Y. Hyun and H.-K. Kim. *Fatigue strength of ultrafine-grained pure Ti after severe plastic deformation*. Scripta Materialia 54 (2006) 1745–1750.
- [88] E. Schafler and R. Pippan. *Effect of thermal treatment on microstructure in high pressure torsion (HPT) deformed nickel*. Materials Science and Engineering A 387-389 (2004) 799–804.
- [89] E. Schafler and M. Zehetbauer. *Characterization of nanostructured materials by X-ray line profile analysis*. Reviews on Advanced Materials Science 10 (2005) 28–33.
- [90] R.A. Wilkins and E.S. Bunn. *Copper and copper base alloys*. McGraw-Hill (1943).
- [91] C.C. Koch. *Optimization of strength and ductility in nanocrystalline and ultrafine grained metals*. Scripta Materialia 49 (2003) 657–662.
- [92] E. Ma. *Eight routes to improve the tensile ductility of bulk nanostructured metals and alloys*. JOM 58 (2006) 49–53.
- [93] Y.M. Wang and E. Ma. *Three strategies to achieve uniform tensile deformation in a nanostructured metal*. Acta Materialia 52 (2004) 1699–1709.
- [94] I.A. Ovid'ko and T.G. Langdon. *Enhanced ductility of nanocrystalline and ultrafine-grained metals*. Reviews on Advanced Materials Science 30 (2012) 103–111.
- [95] R.Z. Valiev, I.V. Alexandrov, Y.T. Zhu and T.C. Lowe. *Paradox of strength and ductility in metals processed by severe plastic deformation*. Journal of Materials Research 17 (2002) 5–8.
- [96] Y. Wang, M. Chen, F. Zhou and E. Ma. *High tensile ductility in a nanostructured metal*. Nature 419 (2002) 912–915.
- [97] H.W. Höppel, M. Korn, Lapovok and H. Mughrabi. *Bimodal grain size distributions in UFG materials produced by SPD: Their evolution and effect on mechanical properties*. Journal of Physics: Conference Series 240 (2010) 012147.
- [98] E. Ma, Y.M. Wang, Q.H. Lu, M.L. Sui, L. Lu and K. Lu. *Strain hardening and large tensile elongation in ultrahigh-strength nano-twinned copper*. Applied Physics Letters 85 (2004) 4932.
- [99] L. Lu, Y. Shen, X. Chen, L. Qian and K. Lu. *Ultrahigh Strength and High Electrical Conductivity in Copper*. Science 304 (2004) 422–426.
- [100] Y.T. Zhu, X.Z. Liao and X.L. Wu. *Deformation twinning in nanocrystalline materials*. Progress in Materials Science 57 (2012) 1–62.
- [101] Y.-H. Zhao, X.-Z. Liao, S. Cheng, E. Ma and Y.T. Zhu. *Simultaneously Increasing the Ductility and Strength of Nanostructured Alloys*. Advanced Materials 18 (2006) 2280–2283.

- [102] Y.-H. Zhao, J.F. Bingert, X.-Z. Liao, Ba.-Z. Cui, K. Han, A.V. Sergueeva, A.K. Mukherjee, R.Z. Valiev, T.G. Langdon and Y.T. Zhu. *Simultaneously Increasing the Ductility and Strength of Ultra-Fine-Grained Pure Copper*. *Advanced Materials* 18 (2006) 2949–2953.
- [103] Y. Estrin and A. Vinogradov. *Fatigue behaviour of light alloys with ultrafine grain structure produced by severe plastic deformation: An overview*. *International Journal of Fatigue* 32 (2010) 898–907.
- [104] P. Lukáš, L. Kunz and M. Svoboda. *Fatigue mechanisms in ultrafine-grained copper*. *Kovove Materialy* 47 (2009) 1–9.
- [105] P. Lukáš, L. Kunza, L. Navrátilová and O. Bokůvka. *Fatigue damage of ultrafine-grain copper in very-high cycle fatigue region*. *Materials Science and Engineering A* 528 (2011) 7036–7040.
- [106] H.W. Höppel, M. Brunnbauer, H. Mughrabi, R.Z. Valiev and A.P. Zhilyaev. *Cyclic deformation behaviour of ultrafine grain size copper produced by equal channel angular extrusion*. In *Proceedings of Werkstoffwoche 2000*.
- [107] S.R. Agnew and J.R. Weertman. *Cyclic softening of ultrafine grain copper*. *Materials Science and Engineering A* 244 (1998) 145–153.
- [108] H. Mughrabi and H.W. Höppel. *Cyclic deformation and fatigue properties of ultrafine grain size materials: current status and some criteria for improvement of the fatigue resistance*. *MRS Proceedings* 634 (2000) B2.1.1.
- [109] H. Mughrabi, H.W. Höppel and M. Kautz. *Fatigue and microstructure of ultrafine-grained metals produced by severe plastic deformation*. *Scripta Materialia* 51 (2004) 807–812.
- [110] M. Goto, S.Z. Han, T. Yakushiji, S.S. Kim and C.Y. Lim. *Fatigue strength and formation behavior of surface damage in ultrafine grained copper with different non-equilibrium microstructures*. *International Journal of Fatigue* 30 (2008) 1333–1344.
- [111] A. Vinogradov, S. Nagasaki, V. Patlan, K. Kitagawa and M. Kawazoe. *Fatigue properties of 5056 Al-Mg alloy produced by equal-channel angular pressing*. *NanoStructured Materials* 11 (1999) 925–934.
- [112] P.S. Pao, H.N. Jones, S.F. Cheng and C.R. Feng. *Fatigue crack propagation in ultrafine grained Al-Mg alloy*. *International Journal of Fatigue* 27 (2005) 1164–1169.
- [113] T. Hanlon, E.D. Tabachnikova and S. Suresh. *Fatigue behavior of nanocrystalline metals and alloys*. *International Journal of Fatigue* 27 (2005) 1147–1158.
- [114] A. Vinogradov. *Fatigue limit and crack growth in ultra-fine grain metals produced by severe plastic deformation*. *Journal of Materials Science* 42 (2007) 1797–1808.
- [115] K. Hockauf. *Ermüdungs- und Rissfortschrittsverhalten ausscheidungshärtbarer ultrafeinkörniger Aluminiumlegierungen*. Ph.D. thesis, Fakultät für Maschinenbau der Technischen Universität Chemnitz (2011).
- [116] C.S. Chung, J.K. Kim, H.K. Kim and W.J. Kim. *Improvement of high-cycle fatigue life in a 6061 Al alloy produced by equal channel angular pressing*. *Materials Science and Engineering A* 337 (2002) 39–44.

- [117] T. Niendorf, F. Rubitschek, H.J. Maier, D. Canadinc and I. Karaman. *On the fatigue crack growth–microstructure relationship in ultrafine-grained interstitial-free steel*. Journal of Materials Science 45 (2010) 4813–4821.
- [118] H.-K. Kim, M.-I. Choi, C.-S. Chung and D.H. Shin. *Fatigue properties of ultrafine grained low carbon steel produced by equal channel angular pressing*. Materials Science and Engineering A 340 (2003) 243–250.
- [119] A.K. Vasudevan, K. Sadananda and K. Rajan. *Role of microstructures on the growth of long fatigue cracks*. International Journal of Fatigue 19 (1997) 151–159.
- [120] L. Kunz and L. Collini. *Mechanical properties of copper processed by Equal Channel Angular Pressing – a review*. Frattura ed Integrità Strutturale 19 (2012) 61–75.
- [121] L.W. Meyer, K. Sommer, T. Halle and M. Hockauf. *Microstructure and mechanical properties affecting crack growth behaviour in AA6060 produced by equal-channel angular extrusion*. Materials Science Forum 584-586 (2008) 815–820.
- [122] A. Hohenwarter and R. Pippan. *Fracture toughness and fatigue crack propagation measurements in ultrafine grained Iron and Nickel*. In TMS Annual Meeting.
- [123] I. Yamaguchi. *Speckle displacement and decorrelation in the diffraction and image fields for small object deformation*. Optica Acta 28 (1981) 1359–1376.
- [124] S.C. Schneider, Y. Gautam and B.G. Zagar. *Application of a locally operating laser-speckle strain sensor*. IEEE Transactions on Instrumentation and Measurement 52 (2003) 1025–1029.
- [125] S.C. Schneider. *Ein laseroptisches Messsystem zur berührungslosen und lokal aufgelösten Bestimmung von Dehnungen*. Ph.D. thesis, Johannes Kepler University Linz (2005).
- [126] <http://stahlbecker.de/produkte/federbandstahl-gehaertet>. Retrieved September 24, 2014.
- [127] R. Stickler and B. Weiss. *Review of the application of ultrasonic fatigue test methods for the determination of crack growth and threshold behavior of metallic materials*. Ultrasonic Fatigue, Conf. Proc. AIME (1982).
- [128] S. Stanzl-Tschegg, H. Mughrabi and B. Schoenbauer. *Life time and cyclic slip of copper in the VHCF regime*. International Journal of Fatigue 29 (2007) 2050–2059.
- [129] C. Bathias and P.C. Paris. *Gigacycle fatigue in mechanical practice*. Marcel Decker, New York (2005).
- [130] M. Klein, A. Hadrboletz, B. Weiss and G. Khatibi. *The ‘size effect’ on the stress–strain, fatigue and fracture properties of thin metallic foils*. Materials Science and Engineering A 319–321 (2001) 924–928.
- [131] <http://www.hbm.com/en/menu/products/strain-gages-accessories/adhesives-bonding-material/z70/>. Retrieved September 24, 2014.
- [132] L. Lu, R. Schwaiger, Z.W. Shan, M. Dao, K. Lu and S. Suresh. *Nano-sized twins induce high rate sensitivity of flow stress in pure copper*. Acta Materialia 53 (2005).

-
- [133] A. Howie and P.R. Swann. *Direct measurements of stacking-fault energies from observations of dislocation nodes*. Philosophical Magazine 6 (1961) 1215–1226.
- [134] X.H. An, S.D. Wu, Z.F. Zhang, R.B. Figueiredo, N. Gao and T.G. Langdon. *Enhanced strength–ductility synergy in nanostructured Cu and Cu–Al alloys processed by high-pressure torsion and subsequent annealing*. Scripta Materialia 66 (2012) 227–230.
- [135] M. Zehetbauer, L. Trieb and H.P. Aubauer. *Effect of short-range order on the mechanical properties of alpha-CuAl*. Zeitschrift für Metallkunde 67 (1976) 431–441.
- [136] P.R. Swann and H. Warlimont. *The electron-metallography and crystallography of copper-aluminium martensites*. Acta Metallurgica 11 (1963) 511–527.
- [137] X.X. Wu, X.Y. San, X.G. Liang, Y.L. Gong and X.K. Zhu. *Effect of stacking fault energy on mechanical behavior of cold-forging Cu and Cu alloys*. Materials and Design 47 (2013) 372–376.
- [138] K.T. Ramesh. *Nanomaterials: Mechanics and mechanisms*. Springer (2009).
- [139] K. Nakanishi and H. Suzuki. *Analysis of the grain size dependence of the yield stress in copper-aluminium and copper-nickel alloys*. Transactions of the Japan Institute of Metals 15 (1974) 435–440.
- [140] S. Miura, N. Ono and Y. Nishimura. *Hall-Petch relation and twin boundaries in pure copper and Cu–Al alloys*. Journal of the Society of Materials Science, Japan 58 (2009) 865–872.
- [141] T.L. Johnston and C.E. Feltner. *Grain size effects in the strain hardening of polycrystals*. Metallurgical Transactions 1 (1970) 1161–1167.
- [142] Y. Nakada and A.S. Keh. *Solid-solution strengthening in Ni–C alloys*. Metallurgical Transactions 2 (1971) 441–447.
- [143] S. Nagarjuna, M. Srinivas, K. Balasubramanian and D.S. Sarma. *The alloy content and grain size dependence of flow stress in Cu–Ti alloys*. Acta Materialia 44 (1996) 2285–2293.
- [144] T.T. Zhu, A.J. Bushby and D.J. Dunstan. *Materials mechanical size effects: a review*. Materials Technology 23 (2008) 193–209.
- [145] N.Q. Chinh, J. Gubicza and T.G. Langdon. *Characteristics of face-centered cubic metals processed by equal-channel angular pressing*. Journal of Materials Science 42 (2007) 1594–1605.
- [146] A. Dubravina, M.J. Zehetbauer, E. Schafler and I.V. Alexandrov. *Correlation between domain size obtained by X-ray Bragg profile analysis and macroscopic flow stress in severely plastically deformed copper*. Materials Science and Engineering A 387–389 (2004) 817–821.
- [147] C.E. Carlton and P.J. Ferreira. *What is behind the inverse Hall–Petch effect in nanocrystalline materials?* Acta Materialia 55 (2007) 3749–3756.
- [148] J. Gubicza, N.Q. Chinh, J.L. Lábár, S. Dobatkin, Z. Hegedüs and T.G. Langdon. *Correlation between microstructure and mechanical properties of severely deformed metals*. Journal of Alloys and Compounds 483 (2009) 271–274.

- [149] B. Jóni, E. Schafner, M. Zehetbauer, G. Tichy and T. Ungár. *Correlation between the microstructure studied by X-ray line profile analysis and the strength of high-pressure-torsion processed Nb and Ta*. Acta Materialia 61 (2013) 632–642.
- [150] E. Wintner and H. P. Karnthaler. Philosophical Magazine 36 (1977) 1317.
- [151] G. Ribárik, T. Ungár and J. Gubicza. *MWP-fit: a program for multiple whole-profile fitting of diffraction peak profiles by ab initio theoretical functions*. Journal of Applied Crystallography 34 (2001) 669–676.
- [152] G. Ribárik, J. Gubicza and T. Ungár. *Correlation between strength and microstructure of ball-milled Al–Mg alloys determined by X-ray diffraction*. Materials Science and Engineering A 387–389 (2004) 343–347.
- [153] M.B. Kerber, M.J. Zehetbauer, E. Schafner, F.C. Spieckermann, S. Bernstorff and T. Ungar. *X-ray line profile analysis - An ideal tool to quantify structural parameters of nanomaterials*. JOM 63 (7) (2011) 61–69+84.
- [154] M. Spanl. *Nahordnungskinetik in verformten und ausgeheilten binären Legierungen*. Ph.D. thesis, University of Vienna (2000).
- [155] J. Gubicza, N.Q. Chinh, T. Csanádi, T.G. Langdon and T. Ungár. *Microstructure and strength of severely deformed fcc metals*. Materials Science and Engineering A 462 (2007) 86–90.
- [156] Z. Hashin and S. Shtrikman. *A variational approach to the theory of the elastic behaviour of polycrystals*. Journal of the Mechanics and Physics of Solids 20 (1962) 343–352.
- [157] L.A. Cain and J.F. Thomas Jr. *Elastic constants of α -phase Cu-Al alloys*. Phys. Rev. B 5 (1971) 4245–4255.
- [158] E. Schafner, K. Simon, S. Bernstorff, P. Hanák, G. Tichy, T. Ungár and M.J. Zehetbauer. *A second-order phase-transformation of the dislocation structure during plastic deformation determined by in situ synchrotron X-ray diffraction*. Acta Materialia 53 (2005) 315–322.
- [159] J.R. Davis. *Tensile Testing*. ASM International (2004).
- [160] P. Frint, T. Halle, M.F.-X. Wagner, M. Hockauf and T. Lampke. *Scaling up the equal-channel angular pressing process – a study on a 6000 aluminium alloy*. Materialwissenschaft und Werkzeugtechnik 41 (2010) 814–821.
- [161] Z. Horita, T. Fujinami and T.G. Langdon. *The potential for scaling ECAP: effect of sample size on grain refinement and mechanical properties*. Materials Science and Engineering A 318 (2001) 34–41.
- [162] G. Yang, M.-X. Yang, Z.-D. Liu and C. Wang. *Three-dimensional microstructures and tensile properties of pure iron during equal channel angular pressing*. International Journal of Iron and Steel Research 18 (2011) 40–44.
- [163] G.B. Rathmayr, A. Hohenwarter and R. Pippan. *Influence of grain shape and orientation on the mechanical properties of high pressure torsion deformed nickel*. Materials Science and Engineering A 560 (2013) 224–231.

-
- [164] A. Rohatgi, K.S. Vecchio and G.T. Grey III. *The influence of stacking fault energy on the mechanical behavior of Cu and Cu-Al alloys: Deformation twinning, work hardening, and dynamic recovery*. Metallurgical and Materials Transactions A 32 (2001) 135–145.
- [165] A.P. Zhilyaev and T.G. Langdon. *Using high-pressure torsion for metal processing: Fundamentals and applications*. Progress in Materials Science 53 (2008) 893–979.
- [166] P. Hübner, R.E. Kiessling, H. Biermann, T. Hinkel, W. Jungnickel, R. Kawalla, H.-W. Höppel and J. May. *Static and Cyclic Crack Growth Behavior of Ultrafine-Grained Al Produced by Different Severe Plastic Deformation Methods*. Metallurgical and Materials Transactions A 38 (2007) 1926–1933.
- [167] A. Hadrboletz, B. Weiss and G. Khatibi. *Fatigue and fracture properties of thin metallic foils*. International Journal of Fracture 107 (2001) 307–327.
- [168] Y. Murakami, ed. *Stress Intensity Factors Handbook*. Pergamon Press, Oxford, UK (1987).
- [169] F.S. Silva. *Crack closure inadequacy at negative stress ratios*. International Journal of Fatigue 26 (2004) 241–252.
- [170] N. Ranganathan, F. Chalon and S. Meo. *Some aspects of the energy based approach to fatigue crack propagation*. International Journal of Fatigue 30 (2008) 1921–1929.
- [171] H.W. Höppel. *Mechanical properties of ultrafine grained metals under cyclic and monotonic loads: An Overview*. Materials Science Forum 503-504 (2006) 259–266.
- [172] K. Hockauf, T. Halle, M. Hockauf, M.F.-X. Wagner and T. Lampke. *Near-threshold fatigue crack propagation in an ECAP-processed ultrafine-grained aluminium alloy*. Materials Science Forum 667-669 (2011) 873–878.
- [173] R.A. Meirom, D.H. Alsem, A.L. Romasco, T. Clark, R.G. Polcawich, J.S. Pulskamp, M. Dubey, R.O. Ritchie and C.L. Muhlstein. *Fatigue-induced grain coarsening in nanocrystalline platinum films*. Acta Materialia 59 (2011) 1141–1149.
- [174] R.A. Meirom, T.E. Clark and C.L. Muhlstein. *The role of specimen thickness in the fracture toughness and fatigue crack growth resistance of nanocrystalline platinum films*. Acta Materialia 60 (2012) 1408–1417.
- [175] J. Horky, G. Khatibi, B. Weiss and M.J. Zehetbauer. *Role of structural parameters of ultra-fine grained Cu for its fatigue and crack growth behaviour*. Journal of Alloys and Compounds 509S (2011) S323–S327.
- [176] K.N. Pandey and S. Chand. *Analysis of temperature distribution near the crack tip under constant amplitude loading*. Fatigue & Fracture of Engineering Materials & Structures 31 (2008) 316–326.
- [177] D. Setman, M. Kerber, E. Schafler and M. Zehetbauer. *Activation enthalpies of deformation-induced lattice defects in Severe Plastic Deformation nanometals measured by Differential Scanning Calorimetry*. Metall. Mater. Trans. A 41 (2010) 810–815.

- [178] B.L. Boyce and H.A. Padilla II. *Anomalous Fatigue Behavior and Fatigue-Induced Grain Growth in Nanocrystalline Nickel Alloys*. Metallurgical and Materials Transactions A 42 (2011) 1793–1804.
- [179] V. Gerold and H.P. Karnthaler. *On the origin of planar slip in f.c.c. alloys*. Acta Metallurgica 37 (1989) 2177–2183.
- [180] M. Spanl, P. Rosenkranz and W. Pfeiler. *Interaction of deformation and short-range order during post-deformation annealing in α -CuAl*. Materials Science and Engineering A 234-236 (1997) 541–543.
- [181] M.F. Denanot and J.P. Villain. *The Stacking Fault Energy in Cu-Al-Zn Alloys*. Phys. Stat. Sol. 8 (1971) K125.

CURRICULUM VITAE

Mag. Jelena Horky

Date of birth: September 12, 1983

Place of birth: Linz, Austria

Education

- since 2009 Doctorate studies at University of Vienna, Faculty of Physics
- 2002 – 2008 Diploma studies in Physics at University of Vienna, diploma thesis entitled “Ermüdungsverhalten von hochdruck-tordiertem Kupfer” (“Fatigue behaviour of HPT Copper”), graduation with distinction on 19.12.2008
- 1994 – 2002 Bundesrealgymnasium Linz, graduation with distinction on 21.6.2002
- 1990 – 1994 Volksschule Feldkirchen/Donau

Professional experience

- 02/2014 – 04/2015 Research associate at the University of Vienna within the FFG Project “H₂desorb – H₂ Speicher aus Mikro- und Nanostruktur-iertem Magnesium für optimale De- und Adsorption”
- 02/2013 – 01/2014 Research associate at the University of Vienna within the FFG K-Project “OptiBioMat – Development and Optimization of Bio-compatible Metallic Materials”
- 01/2009 – 03/2012 Research associate at the University of Vienna within the National Research Network “High Performance Bulk Nanocrystalline Materials” financed by the FWF

Publications

- 18. “Long-term hydrogen storage in Mg and ZK60 after Severe Plastic Deformation”, A. Grill, J. Horky, A. Panigrahi, G. Krexner, M. Zehetbauer, International Journal of Hydrogen Energy, accepted for publication.
- 17. “Bimodal grain size distribution enhances strength and ductility simultaneously in a low-carbon low-alloy steel”, P.J. Szabó, D.P. Field, B. Jóni, J. Horky, T. Ungár, Metallurgical and Materials Transactions A 46 (2015) 1948-1957.

16. "Changes in microstructure and physical properties of skutterudites after severe plastic deformation", G. Rogl, A. Grytsiv, J. Bursik, J. Horky, R. Anbalagan, E. Bauer, R.C. Mallik, P. Rogl, M. Zehetbauer, *Physical Chemistry Chemical Physics* 17 (2015) 3715-3722.
15. "Influence of deformation temperature on texture evolution in HPT deformed NiAl", C. Tränkner, R. Chulist, W. Skrotzki, B. Beausir, T. Lippmann, J. Horky, M. Zehetbauer, *IOP Conference Series: Material Science and Engineering* 63 (2014) 012154.
14. "Enhancement of mechanical properties of biocompatible Ti-45Nb alloy by hydrostatic extrusion", K. Ozaltin, W. Chrominski, M. Kulczyk, A. Panigrahi, J. Horky, M. Zehetbauer, M. Lewandowska, *Journal of Materials Science* 49 (2014) 6930-6936.
13. "Effect of microstructural stability on fatigue crack growth behaviour of nanostructured Cu" J. Horky, G. Khatibi, D. Setman, B. Weiss, M. Zehetbauer. *Mechanics of Materials* 67 (2013) 38-45.
12. "Nature and density of lattice defects in ball milled nanostructured copper", D. Setman, M. Kerber, H. Bahmanpour, J. Horky, R.O. Scattergood, C.C. Koch, M.J. Zehetbauer, *Mechanics of Materials* 67 (2013) 59-64.
11. "Dependence of thermoelectric behaviour on severe plastic deformation parameters: A case study on p-type skutterudite DD0.60Fe3CoSb12", G. Rogl, A. Grytsiv, P. Rogl, E. Poyanian, E. Bauer, J. Horky, D. Setman, E. Schafner, M. Zehetbauer, *Acta Materialia* 61 (2013) 6778-6789.
10. "Thermoelectric properties of chalcogenide based Cu₂xZnSn_{1-x}Se₄", C. Raju, M. Falmbigl, P. Rogl, X. Yan, E. Bauer, J. Horky, M. Zehetbauer, R.C. Mallik, *AIP Advances* 3 (2013) 032106.
9. "Effect of high-pressure torsion on the structure and magnetic properties of as-cast Nd_{9.5}Fe_{84.5}B₆ alloy", S.V. Polikutkina, V.P. Menushenkov, S.V. Skorodumov, M. Zehetbauer, J. Horky, *METAL 2013 – 22nd International Conference on Metallurgy and Materials, Conference Proceedings* (2013) 1542-1545.
8. "Changes of thermoelectric properties and hardness after HPT processing of micro- and nanostructured skutterudites", G. Rogl, D. Setman, E. Schafner, J. Horky, M. Kerber, M. Zehetbauer, M. Falmbigl, P. Rogl, E. Bauer, *NATO Sciences for Peace and Security B: New Materials for Thermoelectric Applications: Theory and Experiment* (2013) 81-91.
7. "Deformation twins and related softening behavior in nanocrystalline Cu-30% Zn alloy", H. Bahmanpour, K.M. Youssef, J. Horky, D. Setman, M.A. Atwater, M.J. Zehetbauer, R.O. Scattergood, C.C. Koch, *Acta Materialia* 60 (2012) 3340-3349.
6. "High-pressure torsion, a new processing route for thermoelectrics of high ZTs by means of severe plastic deformation", G. Rogl, D. Setman, E. Schafner, J. Horky, M.

- Kerber, M. Zehetbauer, M. Falmbigl, P. Rogl, E. Royanian, E. Bauer, *Acta Materialia* 60 (2012) 2146-2157.
5. "Effect of HPT processing on the structure, thermoelectric and mechanical properties of $\text{Sr}_{0.07}\text{Ba}_{0.07}\text{Yb}_{0.07}\text{Co}_4\text{Sb}_{12}$ ", G. Rogl, Z. Aabdin, E. Schafner, J. Horky, D. Setman, M. Zehetbauer, M. Kriegisch, O. Eibl, A. Grytsiv, E. Bauer, M. Reinecker, W. Schranz, P. Rogl, *Journal of Alloys and Compounds* 537 (2012) 183-189.
 4. "Role of structural parameters of ultra-fine grained Cu for its fatigue and crack growth behaviour", J. Horky, G. Khatibi, B. Weiss, M.J. Zehetbauer, *Journal of Alloys and Compounds*, 509S (2011) S323-S327.
 3. "Application of a locally operating laser-speckle strain sensor on tensile deformation of miniaturized nanostructured specimens", J. Horky, M. Lederer, B. Weiss, M. Zehetbauer, B. Zagar, *Proceedings of the IMEKO TC2 Symposium on Photonics in Measurement* (2011).
 2. "Nanocrystallization and dissolution of immiscible powder alloys using high pressure torsion", S. Kahofer, M.J. Zehetbauer, H. Danninger, E. Schafner, M. Kerber, J. Horky, *Materials Science Forum* 667-669 (2011) 151-156.
 1. "High cycle fatigue behaviour of copper deformed by high pressure torsion", G. Khatibi, J. Horky, B. Weiss, M.J. Zehetbauer, *International Journal of Fatigue* 32 (2010) 269-278.

Conference contributions

Talks

- | | |
|---------|---|
| 07/2014 | "Mechanical properties and microstructure of HPT processed Mg-Zn-Ca alloys for biodegradable implants", NanoSPD6 – 6 th International Conference on Nanomaterials by Severe Plastic Deformation, Metz, France. |
| 04/2012 | "On the sensitivities of fatigue and crack propagation to the purity of UFG Cu", 23 rd Colloquium on Fatigue Mechanisms, Poitiers, France. |
| 03/2012 | "Fatigue and crack propagation in SPD Cu with regard to microstructural stability", DPG-Frühjahrstagung, Berlin, Germany. |
| 03/2012 | "Comparison of structure and properties of nanomaterials by Ball Milling and High Pressure Torsion", TMS 2012, Orlando, Florida, USA. |
| 03/2012 | "Consolidation of nanostructured copper and copper based alloys via High Pressure Torsion", TMS 2012, Orlando, Florida, USA. |
| 09/2011 | "Fatigue crack growth behaviour of nanostructured Cu: Role of grain size, purity and strength", E-MRS 2011 Symposium C: Mechanical Properties Of Nanomaterials – Experiment and Modelling, Warsaw, Poland. |
| 05/2011 | "Application of a locally operating laser-speckle strain sensor on tensile deformation of miniaturized nanostructured specimens", 20 th IMEKO TC2 Symposium on Photonics in Measurement, Linz, Austria. |

- 03/2011 "Influence of microstructural stability on the fatigue and crack propagation behaviour of copper deformed by high pressure torsion", NanoSPD5 – 5th International Conference on Nanomaterials by Severe Plastic Deformation, Nanjing, China.
- 03/2011 "Influence of microstructural stability on the fatigue and crack growth behaviour of HPT Cu", 22nd Colloquium on Fatigue Mechanisms, Vienna, Austria.
- 07/2010 "Role of structural parameters of ultrafine grained Cu for its fatigue and crack growth behaviour", ISMANAM 2010 – 17th International Symposium on Metastable, Amorphous and Nanostructured Materials, Zurich, Switzerland.
- 03/2010 "Fatigue crack growth in HPT copper ", 21st Colloquium on Fatigue Mechanisms, Brno, Czech Republic.
- 02/2010 "Fatigue crack growth behaviour of ultrafine grained copper", TMS 2010, Seattle, USA.
- 03/2008 "High cycle fatigue behaviour of HPT copper of different purities", 19th Colloquium on Basic Mechanisms of Fatigue, Dresden, Germany.

Poster presentations

- 10/2014 "Cyclic Stability of Hydrogen Storage Properties of SPD Processed Nanostructured Materials", HySEA 2014 – International Conference on Hydrogen Storage, Embrittlement and Applications, Rio de Janeiro, Brasil.
- 09/2011 "Influence of purity and grain size on the fatigue crack growth behaviour of SPD nano copper", 2nd International Workshop on the Plasticity of Nanocrystalline Metals, Bosen, Germany.
- 09/2009 "High cycle fatigue properties of UFG Cu", 30th Risø International Symposium on Materials Science – Nanostructured Materials – Fundamentals to Application, Risø, Denmark.
- 07/2009 "High cycle fatigue behaviour of small-sized HPT Cu specimens", International Summer School on Micro-Mechanical Experiments, Leoben, Austria.
- 09/2008 "Fatigue behaviour of nanocrystalline Cu processed by High Pressure Torsion", International Workshop on the Plasticity of Nanocrystalline Metals, Bosen, Germany.

Teaching activity

10/2010 – 06/2011 Teaching within the laboratory course in basic physics.

Conference organisation

Member of the organizing committee of the 22nd Colloquium on Mechanisms of Fatigue, March 1–2, 2011, University of Vienna.

ACKNOWLEDGEMENTS

First, I want to thank all my – present and former – colleagues of the group *Physics of Nanostructured Materials* for supporting me in all kinds of smaller and larger scientific and technical troubles. I really enjoyed being part of this kind team.

Special thank goes to *Prof. Michael Zehetbauer* for his supervision of this thesis, helpful discussions, and for offering possibilities of employment as well as numerous attendances at international conferences.

I want to thank *Dr. Golta Khatibi* for valuable assistance in the development of the set-ups to measure fatigue and crack growth of small-scaled samples and I also want to thank her together with *Prof. Brigitte Weiss* for fruitful discussion on the interpretations of the results.

For further assistance I want to thank *Mag. Roman Schuster* for the X-ray line profile analysis and the whole team which was conducting the measurements at the Sincrotrone Trieste (local support Sigrid Bernstorff): *Prof. Erhard Schafner*, *Dr. Florian Spieckermann*, *Mag. Gerald Polt* and *Dipl.-Ing. Harald Wilhelm*. Moreover, I thank *Dr. Stefan Puchegger* and the whole *Faculty Center for Nanostructure Research* for help with SEM and sample preparation. Furthermore, I want to thank *Prof. Bernhard Zagar* from the Johannes Kepler University Linz for providing his knowledge about laser-speckle-based strain measurement and *Dr. Wei Wei* from the Changzhou University who produced and tested several of the HPT Cu-Al tensile samples alloys during his stay in Vienna. I also want to thank the *Erich Schmid Institute of Material Science* in Leoben for providing the HPT facility in the early stages of this thesis.

Research is only possible with financial support. Therefore, I am grateful for the employments by the Austrian Science Fund (Project No. S10403), the Austrian Research Promotion Agency (COMET K-Project “OptiBioMat”) as well as the “Klima- und Energiefonds”.

Last but not least I want to thank my family and friends for their constant support and their encouragements in all situations.